Enhancing Stability of Powder-Route Nanocrystalline Tungsten-Titanium via Alloy Thermodynamics

by

Tongjai Chookajorn

B.S., Materials Science and Engineering
Carnegie Mellon University, 2006

Submitted to the Department of Materials Science and Engineering
in Partial Fulfillment of the Requirements for the Degree of

Doctor of Philosophy in Materials Science and Engineering
at the
MASSACHUSETTS INSTITUTE OF TECHNOLOGY

September 2013

Signature of Author: .....
Department of Materials Science and Engineering
August 16, 2013

Certified by: .....
Christopher A. Schuh
Danae and Vasilios Salapatas Professor of Metallurgy
Thesis Supervisor

Accepted by: .....
Gerbrand Ceder
Chair, Departmental Committee for Graduate Students

Enhancing Stability of Powder-Route Nanocrystalline Tungsten-Titanium via Alloy Thermodynamics

by

Tongjai Chookajorn

Submitted to the Department of Materials Science and Engineering
on August 16, 2013 in Partial Fulfillment of the Requirements for the
Degree of Doctor of Philosophy in Materials Science and Engineering

ABSTRACT

Improvement in material properties as a result of grain size refinement to the nanoscale is often limited by an inherent tendency of these nanostructured materials to coarsen especially at the high temperatures required for processing. The structural instability stems from a large volume fraction of grain boundaries that carry an intrinsic energy penalty, but can be overcome by a consideration of the thermodynamics-based mechanism of interface energy relief via alloying. Suitable alloying conditions can provide a solute segregated grain boundary configuration that enables a nanostructured alloy to become the system's most energetically preferable state. A thermodynamics-based Monte Carlo method that captures the physics of regular solution mixing and grain boundary segregation in nanostructured alloys is developed and used to study the energetics and equilibrium structures of binary alloys. Our simulation is used to identify the alloying elements with preferable interface stabilizing capability appropriate for the high-temperature sintering requirement for powder-route nanocrystalline tungsten. Based on both alloy simulation and consideration of material properties, titanium is selected as a suitable alloying element. Nanocrystalline tungsten alloys with 0-20 atomic percent titanium content are produced by high-energy ball milling and tested at the expected sintering temperature of 1100°C. With an addition of 20 atomic percent titanium, nanocrystalline tungsten shows retention of nanoscale grain size after a one-week equilibration at 1100°C. Scanning transmission electron microscopy and atom probe tomography techniques reveal a heterogeneous distribution of titanium in the alloy with enhanced grain stability, which contradicts the expectation of a uniform solid solution by conventional bulk thermodynamics but is explicitly predicted by the alloy simulation when grain boundaries are included as possible equilibrium states. The segregation profiles from the experimental characterizations and simulated results show depletion of titanium from tungsten grain centers and enrichment of titanium well above the nominal concentration in the grain boundary vicinity in a form of complex segregation state.

Thesis Supervisor: Christopher A. Schuh

Title: Danae and Vasilios Salapatas Professor of Metallurgy

Acknowledgements

I would like to thank the members of my thesis committee, Professor Silvija Gradecak and Professor Carl Thompson, for their useful advice and insightful comments. I truly appreciate their time in evaluating my thesis work and also their support and encouragements.

The staff members of the MIT Center for Materials Science and Engineering, especially Dr. Shiahn Chen, Dr. Yong Zhang, and Dr. Scott Speakman, are gratefully acknowledged. The trainings I received and their help in CMSE have extensively helped me develop my experimental skills and understandings of these tools. Dr. Andrew Magyar, Dr. Mor Baram, and Professor David Bell of Harvard University are acknowledged for their help on atom probe tomography. Matt Humbert and Don Galler are also acknowledged for their help in the metallurgy and glove box labs.

The Schuh research group members have been very helpful and kind during my time in the group. I enjoy working and talking with all of you both scientifically and nonscientifically, in- and outside the lab, and I have learned tremendously from all of you. Members of the MIT department of Materials Science and Engineering have also been very nice and I appreciate our efficient and helpful support team (thank you, Angelita, Elissa, Jazy and Diane).

I would like to especially thank my advisor, Professor Chris Schuh, for the invaluable training and advice throughout my Ph.D. career at MIT. Chris has always encouraged me to tackle challenging problems and has always inspired me to do a better job. Many accomplishments in this thesis would not have been possible without his guidance and teaching. Thank you for setting a great example of a good scientist and for consistently helping me push my limits.

I am grateful for the friendship I have made during my time at MIT and would like to thank all of you for making my life at MIT and in Boston so enjoyable. And last but not least, I would like to thank my family for being a great support and building a solid foundation by giving me a great education from the first day I could learn. Special thanks go to my brother, Dr. Thanat Chookajorn, for always giving me a genuine advice on everything.

Table of Contents

List of Figures

List of Tables

Chapter 1: Introduction

1.1. Nanocrystalline metals: properties and opportunities

Refinement of grain size to the nanometer scale can enhance properties of metals compared to their coarse grained counterparts, and in some cases provide us with an ability to control their properties via careful structural design. As the grain size is reduced below 100 nm, material behaviors tend to change drastically with the change in grain size and many interesting physical phenomena have been observed. For instance, the Hall-Petch relation describes a strong correlation between reduction in grain size and increase in strength and hardness of metals, and the studies of nanocrystalline Ni alloys show the obtainable maximum strength from the average grain size on the order of tens of nanometers, as shown in Figure 1.1(a) [1-3]. In addition to high strength and hardness, improvements accompanying structural refinement have been observed in nanostructured metals, both in the mechanical sense including superplasticity and better wear resistance, and also in other areas of applications such as increased thermoelectric figure of merit, high electrical conductivity, influence on magnetic properties and improved corrosion resistance [4-9]. These behaviors may result from the high volume fraction of grain boundaries and therefore different interface-dominated physics that emerge on the nanometer length scale.

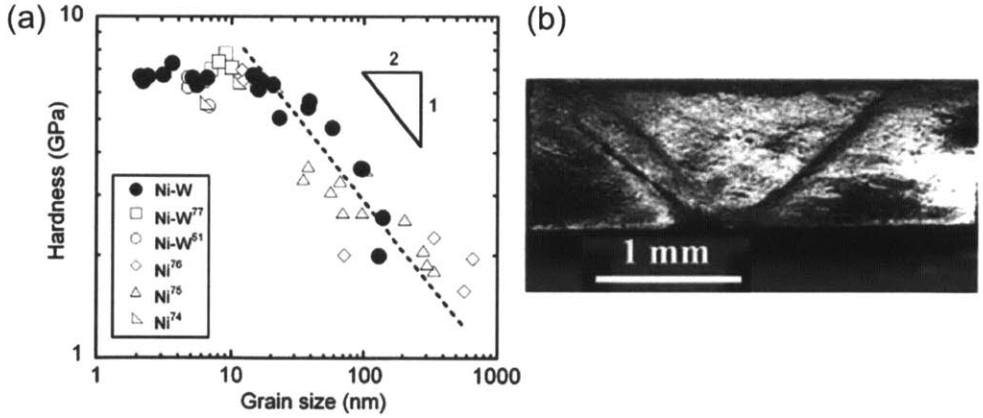

Figure 1.1: Property enhancement as a result of nanostructuring in metals. (a) Improved hardness with grain size refinement in nanocrystalline Ni alloys [1]. (b) Adiabatic shear banding in nanostructured W [10].

One implication of the high interface or defect content is a possible change in deformation mechanism, with many interesting deformation behaviors reported in particular in body centered cubic (BCC) nanocrystalline metals. For instance, strain rate sensitivity is

suppressed in ultrafine grained BCC metals but increases in ultrafine grained face centered cubic (FCC) metals [11]. When deformed, some nanocrystalline BCC metals can exhibit localized deformation, or shear localization, instead of uniform plastic deformation or axial cracking, especially at high rate loading. Examples include the shear bands observed in nanostructured iron under compression, and in nanostructured vanadium under dynamic loading [12-15]. Furthermore, there is evidence of shear localization and adiabatic shear banding in nanostructured tungsten under uniaxial dynamic compression, as shown in Figure 1.1(b). This tungsten, which was produced by severe plastic deformation, has a remarkably high strength with a maximum hardness of 11 GPa measured locally [10, 16, 17].

Tungsten and many BCC metals are refractory metals with extremely high melting temperature as well as high strength and density even in their coarse grained structure. The comparison of tensile strength and density in Figure 1.2 identifies tungsten as one of the strongest metals in pure form. In addition, with appreciable strength and yield point retention at high temperatures, it has the highest tensile strength of all pure metals above 1650°C, high creep resistance, the highest melting point among pure metals (3422°C) and also low vapor pressure [18, 19]. Because of its intrinsically high density and strength, tungsten is a potential replacement for the chemically toxic depleted uranium in kinetic energy penetrator applications, given that certain behaviors such as shear localization, low strain rate sensitivity, and self-sharpening characteristics under impact loading can be attained. Although coarse grained tungsten does not exhibit shear localization under high rate loading, nanocrystalline BCC metals have a strong tendency to do so. Nanostructuring tungsten could induce these behaviors and in general is a direction worth exploring for high strength and high temperature applications. In order to do so, an important problem to first address is the nanostructure's stability against coarsening, especially at high temperatures required for processing and also usage.

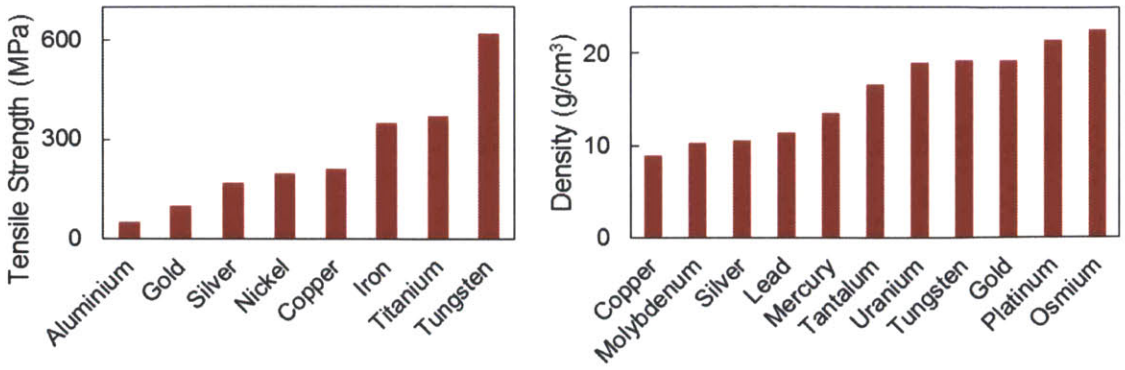

Figure 1.2: Tensile strength and density of pure metals (data from [20, 21]).

1.2. Nanostructure stability against coarsening

Even though their large volume fraction of grain boundaries gives rise to interesting behaviors in nanocrystalline materials, these so-called defect structures exist in a relatively high energy state compared to the regular crystalline arrangement in the grain interior. Nanocrystalline materials are generally unstable, and many undergo grain coarsening at room temperature or low homologous temperatures of less than 0.3 in pure form [22, 23]. Figure 1.3 shows an example of room-temperature grain coarsening in nanocrystalline palladium. After a day, the average grain size suffers a five-fold increase. The grain structure completely transforms from nanocrystalline to microcrystalline after two months at ambient temperature.

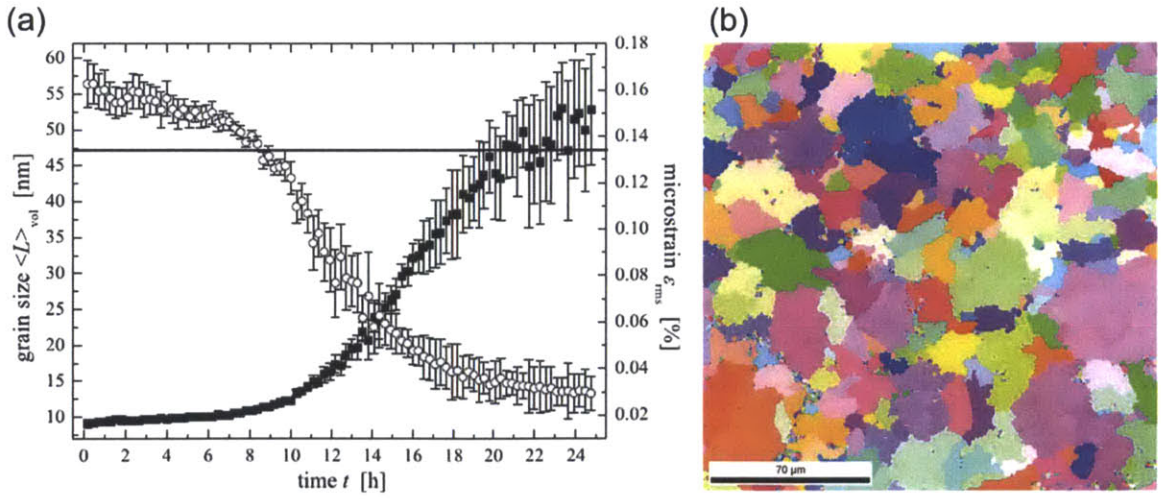

Figure 1.3: Room-temperature grain coarsening observed in nanocrystalline Pd after (a) one day and (b) two months [23].

As a result, even though nanoscale grain sizes can be fairly easily achieved by various processing methods, these fine grain structures and their associated enhanced properties can be short-lived, thus preventing nanocrystalline materials from large-scale batch processing or full deployment. Processing methods for metals, especially those that are refractory, often involve high temperature to induce malleability, interdiffusion, or even melting, for example during shape forming, joining, casting, or heat treatment. Powder-route processing allows materials to be processed entirely in the solid state at milder temperatures and is a good candidate for nanocrystalline metal processing. Nevertheless, a high-temperature consolidation step is still required to sinter power particulates into a bulk form. Grain growth, reported to be significant above 1400°C in coarse grained tungsten [24], and in some cases recrystallization reportedly around 1700°C [25], should be taken as the main considerations. In its usual coarse grained form, tungsten powder can be sintered in the temperature range of 1100-1600°C [24, 26, 27]. Although the sintering mechanism and the resulting temperature cycle requirement could be different when the grain size is refined to the nanoscale, practical nanocrystalline tungsten should be able to resist grain coarsening at least at 1100°C in anticipation of high-temperature powder sintering.

1.3. Structural stabilization and control via alloying and grain boundary segregation

Conventional strategies for grain growth inhibition can be divided into two general categories, namely kinetics-based and thermodynamics-based approaches. The kinetics based approach relies on temporarily trapping structures in an unstable or metastable state; grain boundaries are pinned and their mobility is reduced. This approach includes porosity drag, second phase drag, solute drag, and chemical ordering. Since the driving force for grain growth is still present, these kinetically stabilized structures are still prone to coarsening. And also more importantly, there is generally a lack of well-established structural control in this method.

On the other hand, the thermodynamics based approach eliminates the driving force for grain growth by creating a special configuration which allows grain boundaries and nanostructured grains to become the system's ground state [28-33]. The interface stabilizing mechanism essentially stems from thermodynamic principles and there is growing experimental evidence that the stability observed in some nanocrystalline metals may surpass what would be expected from a kinetics-based mechanism. From a thermodynamic perspective, a minority

element can be selected such that it preferentially segregates to grain boundaries, where it can exist in a lower energy state compared to the grain interior, and in turn relieve the energy penalty of these interfaces. The driving force for coarsening is therefore reduced or in ideal cases completely eliminated.

From a viewpoint of thermodynamic energy minimization, the system free energy of a polycrystal at a constant temperature and pressure can be written as:

$$G = \Sigma \mu_i N_i + \gamma A \tag{1.1}$$

where N is the number of atoms of chemical type 'i' with the chemical potential μ_i, and A is the total grain boundary area with the associated energy of γ per unit area. A stable grain structure can be achieved when the derivative of the free energy with respect to the change in total grain boundary area, $\frac{dG}{dA}$, is zero. This requires a reduction in the grain boundary energy penalty by an alloying element via:

$$\gamma(X,T) = \gamma_0 - \Gamma(\Delta H^{seg} + kT\ln X), \tag{1.2}$$

where γ and γ_0 are the grain boundary energies of alloyed and unalloyed materials, respectively, Γ is the specific solute excess at the grain boundaries, ΔH^{seg} is the dilute-limit enthalpy of grain boundary segregation, k is the Boltzmann constant, T is the absolute system temperature, and X is the global solute content. According to Equation (1.2), grain boundary energetics, and therefore nanostructure stability, can be modified via the concentration and characteristics of alloying elements and the effective grain boundary energy after alloying is dictated by the added solute content.

Alloying thus allows the grain boundary energy penalty to be lowered in a controllable manner. As the grain size gets smaller, the free energy of the system rises due to the increase in the total grain boundary area, A. However, by alloying there is a fraction of grain boundaries that can exist without an energy penalty. These "stabilized" grain boundaries do not contribute to the increase in system energy and in some cases help reduce it. When the two effects are combined, there is a minimum in free energy at a certain average grain size such that the overall grain structure can exist in a stable state. As the average grain size fluctuates away from this minimum, the free energy increases and overall grain growth or shrinkage becomes energetically unfavorable. This equilibrium grain size is controlled by the fraction of stabilized grain

boundaries and the alloying composition. Consequently, an implication of this concept is that retention of nanoscale grain size should indeed be possible by alloying. Figure 1.4 shows experimental evidence of alloying on stabilizing a nanoscale grain structure in Ni alloys. Nanocrystalline Ni with similar initial grain size suffers grain coarsening in the pure form while maintaining the grain structure at high temperature with an addition of the alloying element W. Beyond grain structure stabilization, microstructural design and property optimization become possible using this alloy stabilization concept. Examples include nanocrystalline Ni-W with grain sizes that can be controlled via the composition of W [1].

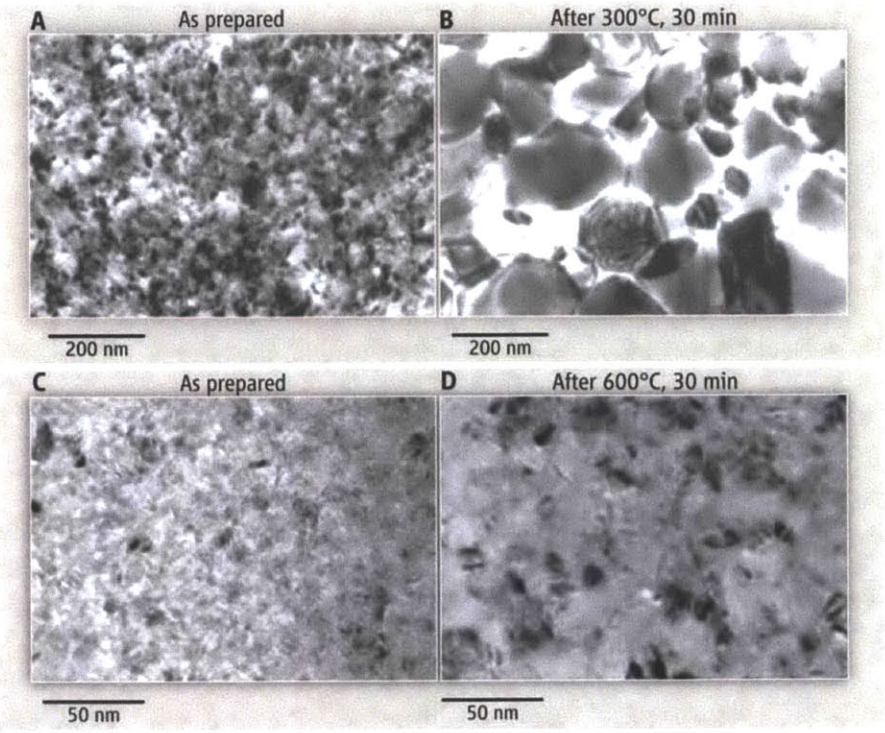

Figure 1.4: Effects of alloying on the high-temperature evolution of grain structures. Unalloyed and alloyed nanocrystalline Ni with similar initial grain sizes (A and C) display completely different behaviors when subjected to high temperature. For the same duration of 30 minutes, the Ni-W alloy can retain the nanoscale grain size at 600°C (D), whereas the unalloyed Ni shows significant grain growth even at a much lower temperature of 300°C (B) [34].

There are several considerations for the selection of an appropriate alloying element for nanostructure stabilization. For the alloying element to be able to segregate to grain boundaries and lower the grain boundary energy, a large atomic size difference between the host metal and the alloying element is generally preferable; High elastic strain energy would induce the alloying

element to accommodate the strain energy by segregating to the relatively loosely packed grain boundaries instead of staying in the crystal interior. One concern about adding a solute is grain boundary embrittlement. Certain elements such as nonmetals are known to cause grain boundaries to become brittle and therefore our choices are focused on metallic elements. In particular, transition metals are good candidates since they do not necessarily promote intergranular fracture. Formation of intermetallic compounds or precipitates can complicate the grain boundary segregation behaviors by abruptly reducing the solute content available in the general crystal vicinity and in some cases can trigger abrupt or abnormal grain growth. In order to ensure that there is a sufficient amount of solute and that a reduction of grain boundary energy is possible by grain boundary segregation, tungsten based binary systems with no intermetallic phase will be examined preferentially here.

1.4. Problem statement and structure of thesis

This thesis is aimed at investigating structural engineering of nanostructured alloys with an emphasis on the structural stability of nanocrystalline tungsten. The research approach is to establish a strategy for structural stabilization against grain coarsening, a processing method for nanocrystalline tungsten, and also characterization methods of grain and chemical structures. The high-temperature structural evolution in nanocrystalline tungsten will be addressed in order to be able to understand their behaviors and instabilities, especially through atomic rearrangement and structural relaxation. The distribution of solute atoms should be investigated to verify if the mechanism is indeed solute segregation. This thesis is organized into three main parts to address the posed research questions.

- Chapter 2: A thermodynamics based simulation method is established and theoretical understandings of nanostructured alloy behaviors are explored to gain more insights on the principles of grain structure stabilization. This simulation method is subsequently used throughout the rest of the thesis to help appreciate and understand the concepts and experimental results that follow.
- Chapter 3: The process of material synthesis begins with the developments of alloying element selection scheme and material processing method, and is supplemented by an introduction of the characterization methods of grain and chemical structures. Nanocrystalline

tungsten alloys are synthesized and the as-processed structures are characterized. Alloys with a range of solute compositions are synthesized in order to study solute effects on thermal stability.

- Chapters 4 and 5: Thermal stability of nanocrystalline tungsten alloys is examined in detail. The processed powder is tested for grain structure stability at the temperatures required for sintering. Post-annealing structures are studied to gain more understanding of the grain size distribution and chemical segregation state.

Chapter 2: Monte Carlo simulations of nanostructure behaviors

2.1. Understanding nanostructure behaviors via alloy thermodynamics

Alloying has been identified as a means of stabilizing grain structures, and many researchers have proposed that such stability can in fact result from actual thermodynamic energy minimization rather than merely introducing a kinetic barrier [1, 28, 30-32, 35-38]. The basis of alloy stabilization can be understood from the standpoint of interface and mixing thermodynamics. Based on the free energy expression of polycrystalline alloys in Equation (1.1), a stable grain structure can be achieved when the derivative of the free energy with respect to the change in total grain boundary area, expressed below, is zero.

$$\frac{dG}{dA} = \frac{d(\Sigma\mu_i N_i)}{dA} + A\frac{d\gamma}{dA} + \gamma \qquad (2.1)$$

For pure materials, the free energy is $G = \mu N + \gamma_0 A$, and the derivative is simply $\frac{dG}{dA} = \gamma_0$. As a result, the system free energy can be lowered by decreasing the total grain boundary area until the grain structure is completely coarsened. On the other hand, for alloyed materials the derivative can be further expanded to:

$$\frac{dG}{dA} = \frac{d(\Sigma\mu_i N_i)}{dX_c}\frac{dX_c}{dA} + A\frac{d\gamma}{dX_c}\frac{dX_c}{dA} + \gamma \qquad (2.2)$$

where X_c is the solute concentration in crystal, or the grain interior.

The derivative $\frac{dG}{dA}$ evaluates differently in open and closed systems. For open systems, the grain interior concentration X_c is kept constant and therefore $\frac{dG}{dA} = \gamma$. Both of these terms, $\frac{dG}{dA}$ and γ, have units of energy per unit area, and both have been called "grain boundary energy" in the literature. For open systems this is appropriate given their equivalence. However, for closed systems these quantities are not equal, and thus different nomenclature is required. Terms such as "open-system grain boundary energy" or "grain boundary formation energy" are appropriate for γ, and in a closed system it has been pointed out that this quantity can even be negative for some grain boundary solute segregation states [28, 32, 35, 37, 39-41]. The quantity $\frac{dG}{dA}$ is the more important term for identifying an equilibrium grain size, which occurs when $\frac{dG}{dA} = 0$ but not

necessarily when $\gamma = 0$. We call $\frac{dG}{dA}$ the "grain boundary area potential", and for a dilute polycrystalline alloy this parameter can be expressed as a function of solute characteristics and concentration by combining Equations (1.2) and (2.1) as:

$$\frac{dG}{dA} = \frac{d(\Sigma\mu_i N_i)}{dA} + \gamma_0 - (\Gamma + A\frac{d\Gamma}{dA})(\Delta H^{seg} + kT\ln X) \qquad (2.3)$$

For alloy systems with positive grain boundary adsorption (i.e. positive Γ and ΔH^{seg}), $\frac{dG}{dA}$ can be suppressed to zero or a negative value by maintaining a sufficient solute excess at the grain boundaries with respect to the change in grain size $\left(\Gamma > -A\frac{d\Gamma}{dA}\right)$, and a free energy minimum at $\frac{dG}{dA} = 0$ can be accessed with a specific grain boundary segregation–grain size state (Γ,A).

This chapter introduces a thermodynamics based simulation that will be used to understand grain-atomic interactions in nanostructured alloys. By treating both chemical configurations and grain boundary states as variables, we can use an equilibrium seeking algorithm such as the Monte Carlo method to probe for the ground state of alloy systems. Conventionally accepted nanostructure behaviors will be investigated using this simulation to both assess the validity of the model and also to gain more insights about nanostructured alloys. Grain and atomic structures can also be presented visually using the simulation and therefore comparison to real material structures as well as elucidation of complex structures that exist in theory but could be difficult to observe or discern experimentally may be possible. Finally, the aforementioned grain boundary energy requirement for thermodynamic grain stability will be revisited.

2.2. Simulation method

Lattice-based Monte Carlo (MC) methods have been widely applied to both alloying thermodynamics and grain structure problems [42-58]. To capture the interaction between solute and solvent in a polycrystalline grain environment and their effects on stabilizing nanostructured grains, we use a lattice MC method that tracks both atomic chemical identity and grain allegiance. As a simplifying first step, only phase separating binary alloys (i.e., those with positive enthalpies of mixing) are considered, and the body centered cubic (BCC) and face

centered cubic (FCC) lattices, as in Figure 2.5, are used as the atomic framework. Each lattice site is assigned an atom type, which denotes the chemical identity of the atom as solvent (A) or solute (B), and a grain number, which differentiates atoms in the same grain from those that are neighbors across grain boundaries. Periodic boundary conditions are applied on all three principal axes. For ease of viewing in what follows, we present two dimensional sections viewed along the [001] direction for the BCC lattice and along the [111] direction for the FCC lattice, with atoms in both the sectioning plane and first sub-surface plane visible.

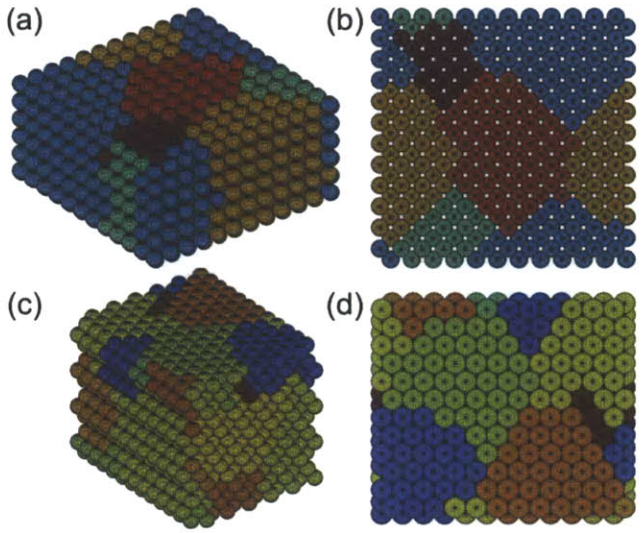

Figure 2.5: Representative lattice of a polycrystalline structure produced by the Monte Carlo simulation. (a) A three dimensional view of a BCC lattice with 12 x 12 x 12 atoms is shown with (b) the top down view along the [001] direction, revealing the top two atomic planes. (c) A three dimensional view of a FCC lattice with 12 x 12 x 12 atoms shows denser packing. (d) The top down view along the [111] direction exposes mostly only the top close-packed (111) plane. The atoms with the same color belong to the same grain.

2.2.1. Bond energy calculation

Our simulation is based on nearest-neighbor interactions only, with six unique bond types: between each pairing of the atomic types (A and B) and lying either in the grain interior or across a grain boundary (i.e., matched or unmatched grain numbers, respectively). The total internal energy, U, is calculated by summing the bond energy between all atoms:

$$U = \sum_{\text{all bonds}}\left[\left(N_{\text{c}}^{\text{AA}}E_{\text{c}}^{\text{AA}} + N_{\text{c}}^{\text{BB}}E_{\text{c}}^{\text{BB}} + N_{\text{c}}^{\text{AB}}E_{\text{c}}^{\text{AB}}\right) + \left(N_{\text{gb}}^{\text{AA}}E_{\text{gb}}^{\text{AA}} + N_{\text{gb}}^{\text{BB}}E_{\text{gb}}^{\text{BB}} + N_{\text{gb}}^{\text{AB}}E_{\text{gb}}^{\text{AB}}\right)\right] \quad (2.4)$$

where N is the number of bonds, and E is the bond energy. The subscript denotes whether the bond is in a crystal (or grain interior, denoted by c) or across a grain boundary (denoted by gb), and the superscript denotes the chemical pairings involved. The internal energy can also be expressed as $U = \Sigma\mu_i N_i + \gamma A - PV + TS$, and at constant pressure P, volume V, temperature T and entropy S, its derivative with respect to the change in total grain boundary area, $\frac{dU}{dA} = \frac{d(\Sigma\mu_i N_i + \gamma A)}{dA}$, is equivalent to the grain boundary area potential as defined earlier.

There are thus six independent inputs to our model, or five if one of the bond types is regarded as the reference state that sets the temperature scale. This multidimensional parameter space offers great flexibility for modeling various alloy systems, but its breadth is too large to consider systematically in detail here. For purposes of simplifying the parameter space, it is useful to connect the bond energies to more routine macroscopic material parameters. These include pure component A grain boundary energy:

$$\gamma_0^{\mathrm{A}} = \frac{zt}{2\Omega^{\mathrm{A}}}\left(E_{\mathrm{gb}}^{\mathrm{AA}} - E_{\mathrm{c}}^{\mathrm{AA}}\right), \tag{2.5}$$

and an equivalent expression for the pure component B grain boundary energy, as well as the alloy enthalpy of mixing:

$$\Delta H^{\mathrm{mix}} = z\omega_{\mathrm{c}}X(1-X), \tag{2.6}$$

and the enthalpy of grain boundary segregation:

$$\Delta H^{\mathrm{seg}} = z\left[\omega_{\mathrm{c}} - \omega_{\mathrm{gb}}\left(1 - \frac{\nu}{1-f_{\mathrm{gb}}}\right) - \frac{1}{zt}\left(\Omega^{\mathrm{B}}\gamma_0^{\mathrm{B}} - \Omega^{\mathrm{A}}\gamma_0^{\mathrm{A}}\right)\left(1 - \frac{\nu}{1-f_{\mathrm{gb}}}\right)\right]$$

$$+ 2zX_{\mathrm{gb}}\omega_{\mathrm{gb}}\left(1 - \frac{\nu}{1-f_{\mathrm{gb}}}\right) - 2z\left[X_{\mathrm{c}}\omega_{\mathrm{c}} + \nu(X_{\mathrm{gb}} - X_{\mathrm{b}})\omega_{\mathrm{gb}}\right], \tag{2.7}$$

which, in the dilute limit of McLean type segregation (with composition $X \to 0$ and grain boundary fraction $f_{\mathrm{gb}} \to 0$) and with the transitional bond fraction $\nu = ½$, can be simplified to:

$$\Delta H^{\mathrm{seg}} = z\left[\omega_{\mathrm{c}} - \frac{\omega_{\mathrm{gb}}}{2} - \frac{1}{2zt}\left(\Omega^{\mathrm{B}}\gamma_0^{\mathrm{B}} - \Omega^{\mathrm{A}}\gamma_0^{\mathrm{A}}\right)\right] \tag{2.8}$$

The dilute-limit enthalpy of grain boundary segregation inherently incorporates various effects such as chemical interactions, difference in interface energies, and solute-solvent size mismatch

(elastic energy), as described by the linear combination of sub-contributions: $\Delta H^{\text{seg}} = \Delta E_{\text{chemical}} + \Delta E_{\text{interface}} + \Delta E_{\text{elastic}}$.

In these equations, $\omega_c = E_c^{AB} - \left(\frac{E_c^{AA} + E_c^{BB}}{2}\right)$, is the regular solution grain interaction energy, $\omega_{gb} = E_{gb}^{AB} - \left(\frac{E_{gb}^{AA} + E_{gb}^{BB}}{2}\right)$, is the grain boundary interaction energy, z is the coordination number, t is the grain boundary thickness, taken as 0.5 nm throughout, and Ω is the atomic volume.

The number of independent parameters can be reduced by focusing strictly on mixing thermodynamics, i.e., by assuming equal like-bond energies in the grain interior, $E_c^{AA} = E_c^{BB}$, and similar grain boundary penalties, $\frac{\Omega^A \gamma_0^A}{zt} = \frac{\Omega^B \gamma_0^B}{zt}$. These parameters are taken to be 486 kJ/mol and 2.64 kJ/mol, respectively, based on the material parameters of tungsten metal but can be regarded as essentially arbitrary. The bond energies are summarized in Table 2.1 for general polycrystalline binary alloys and also for the special case with the two assumptions applied.

Table 2.1: Bond energies in a polycrystalline binary alloy in full and simplified forms.

Bond energy	Full form	Simplified form
E_c^{AA}	E_c^{AA}	E_c^{AA}
E_c^{BB}	E_c^{BB}	E_c^{AA}
E_c^{AB}	$\left(\frac{E_c^{AA} + E_c^{BB}}{2}\right) + \omega_c$	$E_c^{AA} + \omega_c$
E_{gb}^{AA}	$E_c^{AA} + \frac{2\Omega^A \gamma_0^A}{zt}$	$E_c^{AA} + \frac{2\Omega^A \gamma_0^A}{zt}$
E_{gb}^{BB}	$E_c^{BB} + \frac{2\Omega^B \gamma_0^B}{zt}$	$E_c^{AA} + \frac{2\Omega^A \gamma_0^A}{zt}$
E_{gb}^{AB}	$\left(\frac{E_c^{AA} + E_c^{BB}}{2}\right) + \omega_{gb} + \frac{1}{zt}\left(\Omega^A \gamma_0^A + \Omega^B \gamma_0^B\right)$	$E_c^{AA} + \omega_{gb} + \frac{2\Omega^A \gamma_0^A}{zt}$

2.2.2. Monte Carlo procedure

The general methods of Monte Carlo simulations can be classified into two main categories, namely the standard or Metropolis Monte Carlo method and the kinetic Monte Carlo method, depending on the thermodynamic or kinetic contributions that dominate the nature of structural evolution. The standard Monte Carlo method samples system configurations for the equilibrium state by transitioning toward lower energy states with possible excitation events governed by the Boltzmann-type probability [59, 60]. On the other hand, the kinetic Monte Carlo method considers the relative rates of transition events, which depends on the energy barrier of transition [61]. The time increment can be obtained from the rate of transition and amounts to the total simulation time. It is appropriate for structural changes that are kinetically motivated and also used to capture the system evolution with time.

Our Monte Carlo procedure is a standard thermodynamics based calculation in the sense that we probe configuration space through individual switching events that are accepted if energy lowering and accepted with probability $\mathrm{P} = e^{\frac{-(E_2-E_1)}{kT}}$ if energy raising; E_1 and E_2 are respectively the total system energies before and after the switch. The transition to a higher energy state ensures that the system can reach the lowest possible energy state without being trapped in a local energy minimum. There are two types of switching events in our MC procedure, considered as independent and referred to as grain switching and atom switching. A type of switch is first selected with equal probability. For atom switching, a solute atom and a solvent atom are selected at random regardless of their grain numbers and their chemical types are exchanged with the original grain number of each atomic site unchanged. For grain switching, an atom is chosen at random, and if it has at least one neighbor of a different grain number, its grain number is changed. The new grain number is chosen at random from among those of its nearest neighbors as well as a unique grain number that matches none of the neighboring atoms. Thus, the grain switching event allows atoms at grain boundaries to change their grain allegiance, or to spontaneously nucleate new grains, which may subsequently grow or disappear.

The system is initialized at 10,000 K, where it is randomized, and then slowly cooled at a rate $\frac{-(T_{\mathrm{step}}-T_{\mathrm{final}})}{1000}$. The system spends one MC step at an immediate temperature, T_{step}, and cooling decelerates as the system temperature converges to the final target, T_{final}. The Monte Carlo procedure proceeds until the total system energy reaches a steady state. All simulations are

performed for 100,000 MC steps, with each step corresponding to an average of one switch event per atom across the whole system. We tested this MC procedure for path-independence, by using different initial states (including bicrystal, polycrystal, amorphous, mixed, and unmixed) and establishing convergence to the same steady-state structure regardless of the initial grain structure and atomic distribution. We also verified that the rate of cooling specified above yielded sufficiently equilibrated structures for the conditions presented, by running various simulations at various rates and obtaining the same results. The equilibrium structures produced using a bicrystal initial state and a faster cooling rate are provided for reference in Figure A.1.

2.2.3. Regular solution mixing

Before considering a system with any influence from grain boundaries, we first start by focusing on the atomic interactions via grain interior mixing based on the regular solution model. Single crystalline structures with 0.1 and 0.2 at.% solute are equilibrated at 500°C with only atom switching active, and for each composition, ΔH^{mix} is varied from 0 to 100 kJ/mol. At these dilute concentrations, the solute-solvent interactions can be simplified to the first few nearest neighbors. At a constant temperature, a transition from a miscible solution to a precipitated structure can occur as the composition or ΔH^{mix} increases, and by considering the total system energy, ΔH^{mix} can be evaluated based on the observation of such transition. In a completely dissolved solid solution, all bonds around solute atoms are A-B bonds and the system energy can be approximated by $E_{\text{dissolved}} = zN^{\text{B}}E_{\text{c}}^{\text{AB}} + \left(\frac{zN}{2} - zN^{\text{B}}\right)E_{\text{c}}^{\text{AA}}$, where N is the total number of atoms, and N^{B} is the number of solute atoms. This can be reduced further to:

$$E_{\text{dissolved}} = zN^{\text{B}}\omega_{\text{c}} + \frac{zN}{2}E_{\text{c}}^{\text{AA}} \tag{2.9}$$

and therefore the calculated enthalpy of mixing, H_{calc}, can be obtained from:

$$H_{\text{calc}} = \frac{E_{\text{dissolved}} - zNE_{\text{c}}^{\text{AA}}/2}{N^{\text{B}}} \tag{2.10}$$

The plots between the calculated and input enthalpies of mixing for both BCC and FCC lattices in Figure 2.6 show good agreement at relatively low ΔH^{mix}. When a solute-solute cluster forms, the system energy is expressed differently as $E_{\text{clustered}} = E_{\text{c}}^{\text{BB}} + (zN^{\text{B}} - 2)E_{\text{c}}^{\text{AB}} + \left(\frac{zN}{2} - zN^{\text{B}} + 1\right)E_{\text{c}}^{\text{AA}}$, or $E_{\text{clustered}} = E_{\text{dissolved}} - 2\omega_{\text{c}}$. Therefore, in systems with a positive

ΔH^{mix}, precipitation can reduce the system energy discreetly via ω_c by minimizing the number of unlike bonds. When solute atoms start clustering, the calculated enthalpy of mixing from Equation (2.10) will be lower than the actual ΔH^{mix}, which is reflected in both the enthalpy plots and the solute distributions in Figure 2.6. The threshold in ΔH^{mix} at the precipitation event decreases with the solute composition. The effects of temperature can also be investigated in the context of regular solution mixing, and the results in Figure A.2 show a transition from solute precipitation to a miscible solid solution with increasing temperature. At elevated temperature, entropy effects start to become significant and therefore an entropically stabilized state may be preferred.

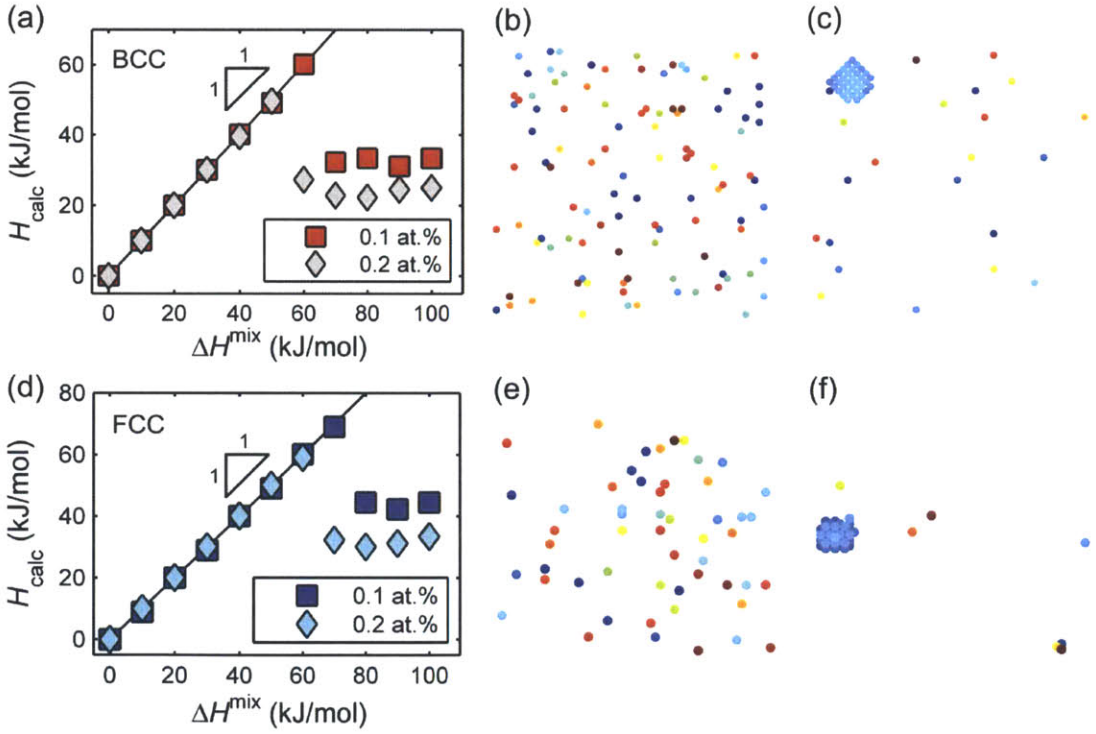

Figure 2.6: (a) Calculated and actual enthalpies of mixing from 30 x 30 x 60 BCC single crystals with 0.1 and 0.2 at.% solute. At 0.2 at.% concentration, the solute distribution changes from (b) miscible at ΔH^{mix} = 50 kJ/mol to (c) precipitated at ΔH^{mix} = 60 kJ/mol. (d) Calculated and actual enthalpies of mixing from 30 x 30 x 30 FCC single crystals. Similarly, at 0.2 at.% concentration, (e) the miscible solute distribution is observed up to ΔH^{mix} = 60 kJ/mol then (f) solute precipitation is evident with increasing enthalpy of mixing from ΔH^{mix} = 70 kJ/mol. The colors of the solute atoms indicate the depth into the page. All simulations are performed at T = 500°C.

2.2.4. Grain boundary segregation

To verify conformity of the present model to conventional grain boundary segregation thermodynamics, we perform some simulations on bicrystal geometries in which the grain numbers are fixed, so as to permit grain boundary segregation to develop independently of any change in grain structure. In the dilute limit, the enthalpy of grain boundary segregation relates to local solute concentrations, X_{gb} in the grain boundaries, and X_c in the grain interior, via the McLean segregation isotherm:

$$\frac{X_{gb}}{1-X_{gb}} = \frac{X_c}{1-X_c}\exp\left(\frac{E_{diff}}{kT}\right) \tag{2.11}$$

where E_{diff} is the energy difference between a solute atom residing in the grain interior with respect to a grain boundary. For a BCC bicrystal conjoined on the (001) planes, $E_{diff} = 8E_c^{AB} - (4E_{gb}^{AB} + 4E_c^{AB})$ which is equal to ΔH^{seg} when ΔH^{mix} and γ_0 are taken as zero to eliminate the effects from chemical mixing and grain boundary energy penalty. For a FCC bicrystal conjoined on the (111) planes, $E_{diff} = 12E_c^{AB} - (3E_{gb}^{AB} + 9E_c^{AB})$. A solute atom occupying a grain boundary site has more bonds in the grain interior than across the grain boundary. Therefore, the transitional bond fraction ν of 3/4 is used, and the energy difference is also equal to ΔH^{seg} under the same conditions as those applied to the BCC lattice.

The relative solute excess at grain boundaries, X_{gb}/X_c, is calculated from bicrystals with X = 0.1-2 at.% and plotted with ΔH^{seg} in Figure 2.7, along with a side view of the bicrystal and a three dimensional solute distribution map showing the solute atoms preferentially segregating at grain boundaries. The energy difference E_{diff} after equilibrating the alloy configuration, denoted by H_{calc} in Figure 2.7(b), displays the expected behavior, but with an upper limit imposed by the measurable relative solute excess around 15 kJ/mol when all solute atoms migrate to the grain boundaries thus setting X_c as zero. Alternatively, by definition E_{diff} can be calculated from the change in system energy normalized by the change in the number of solute atoms relocated to the grain boundaries after equilibration. This method reproduces the same relationship with ΔH^{seg} but with no upper limit in strongly segregating systems.

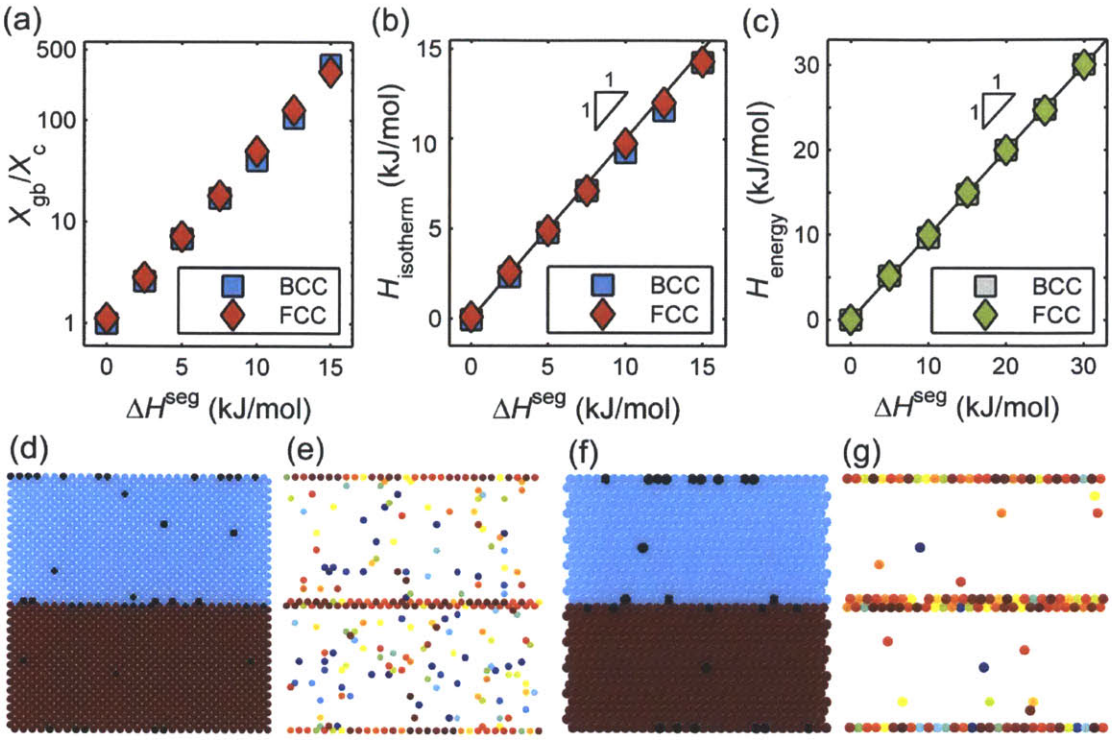

Figure 2.7: (a) The relative solute excess at grain boundaries in a bicrystal shows a higher tendency for grain boundary segregation with increasing ΔH^{seg}. The energy difference calculated using (b) the segregation isotherm and (c) the change in system energy both show the expected relationship with the input ΔH^{seg}. (d) A side view of a 30 x 30 x 60 BCC bicrystal with 2 at.% solute and ΔH^{seg} = 15 kJ/mol. The color denotes the grain numbers and the black circles represent the solute atoms. (e) A solute distribution map of the same BCC bicrystal with the color of the solute atoms indicating the depth into the page. (e) A side view of a 30 x 30 x 30 FCC bicrystal with 2 at.% solute and ΔH^{seg} = 15 kJ/mol. (f) A solute distribution map of the same FCC bicrystal. All simulations are performed at T = 25°C.

Grain boundary segregation behaviors across a wider range of composition is further investigated using the same BCC bicrystal geometry, ΔH^{seg} = 10 kJ/mol, X = 0.1 – 40 at.%, and T = 25°C. The effective grain boundary segregation energy, E_{diff}, is calculated from the measured relative solute excess at grain boundaries, X_{gb}/X_c, using Equation (2.11) and plotted with the global solute composition, X, in Figure 2.8. At dilute concentrations, the value of E_{diff} is similar to the input ΔH^{seg} value of 10 kJ/mol. However, at higher solute content, the effective grain boundary segregation energy begins to drop as the grain boundaries start to become saturated with solute atoms. We conclude that conventional grain boundary segregation behavior is well captured by our simulation in both dilute and non-dilute limits with proper composition dependence.

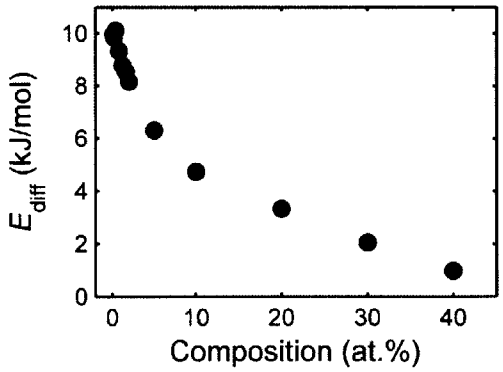

Figure 2.8: Variation between the effective grain boundary segregation energy and the global solute composition.

2.2.5. Classification of nanostructure behaviors

The bonding energies in Table 2.1 display two independent adjustable bonding parameters, represented by the mixing parameters for grain and grain boundary regions: ω_c and ω_{gb}, which simply map to the more intuitive parameters, ΔH^{mix} and ΔH^{seg}, using $\Delta H^{mix} = z\omega_c$. Consequently, we can use a two dimensional material parameter space such as in Figure 2.9 to represent binary alloy systems based on their mixing and grain boundary segregation characteristics. The state space in Figure 2.9 encloses four main regions that emerge from consideration of the bonding energies used in our MC model, and which are divided by the following boundary lines.

1. *Onset of solute segregation at grain boundaries*, $\omega_{gb} = 0$

The most important consideration for the present work is whether or not grain boundary solute segregation will occur, opening the door to stable nanostructures. Relief of interface energy penalty by grain boundary segregation requires a negative ω_{gb}, and the boundary line at $\omega_{gb} = 0$ along the diagonal of the map in Figure 2.9, with negative ω_{gb} lying above the boundary line (or $\Delta H^{seg} > \Delta H^{mix}$), represents the cases where alloying can lower the grain boundary formation energy compared to its single-component counterpart.

2. *Transition from solid solution to grain boundary segregation*, $\omega_{gb} = -\frac{2\Omega^A \gamma_0^A}{zt} + \omega_c$

Even if ω_{gb} is negative and alloying lowers the grain boundary penalty, a bulk solid solution may yet be more stable than a grain boundary segregated state. Only when E_{gb}^{AB} is lower

than E_c^{AB} would alloying be able to provide a lower-energy grain boundary state than a bulk solid solution. This occurs when the following inequality is met: $\omega_{gb} < -\frac{2\Omega^A \gamma_0^A}{zt} + \omega_c$.

3. *Onset of grain metastability*, $\omega_c = \frac{2\Omega^A \gamma_0^A}{zt}$

For those cases where grain boundary solute segregation is not preferred (i.e., lying in the lower part of Figure 2.9), the structure will not have a stable nanostructure. The ground state in this condition could be a solid solution or a bulk phase separated state. The vertical boundary line in Figure 2.9 represents the crossover between dominance of E_c^{AB} and E_{gb}^{AA} and therefore whether formation of solid solution in the grain interior or a single-component grain boundary results in a higher energy state. Solute precipitation becomes more likely with higher ω_c, and when $\omega_c > \frac{2\Omega^A \gamma_0^A}{zt}$, the system can lower the energy by forming a precipitated polycrystalline structure rather than a single crystal solid solution.

4. *Onset of grain boundary stabilization*, $\omega_{gb} = -\frac{2\Omega^A \gamma_0^A}{zt}$

The last boundary line represents the ideal case where alloying can lower the grain boundary energy penalty sufficiently enough that a nanocrystalline structure becomes the system's ground state. This requires the alloyed grain boundaries to be the lowest-energy bonding state; such condition is realized only when $\omega_{gb} < -\frac{2\Omega^A \gamma_0^A}{zt}$, which defines the upper, green-shaded region in Figure 2.9.

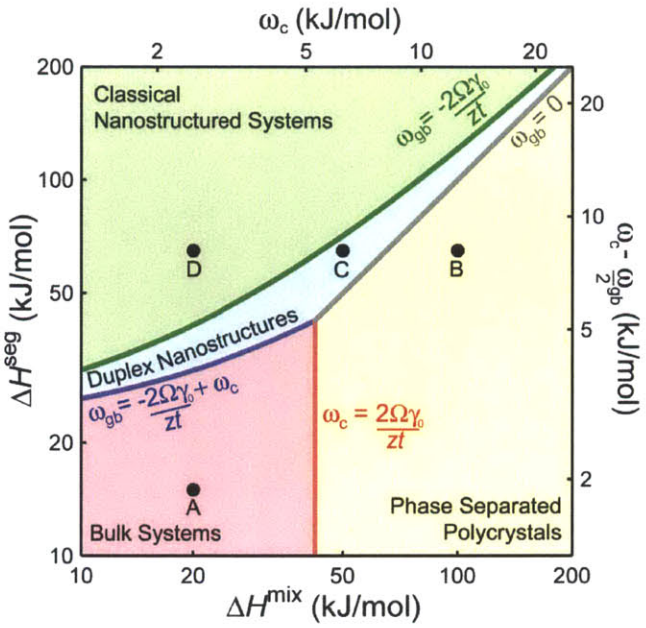

Figure 2.9: Nanostructure stability map for binary alloys with four boundary lines and four behavioral regimes.

The above boundary lines construct the diagram in Figure 2.9, and delineate four main regions worthy of further exploration using the MC model. We select four particular alloy systems, labeled A to D on the stability map above, to represent the regions enclosed by the four boundary lines. These are denoted:

- **Region A**: Bulk systems (single crystalline solid solutions with precipitation of solute beyond solubility limit)
- **Region B**: Phase separated polycrystals (polycrystalline structures with solute precipitation)
- **Region C**: Duplex nanostructures (coexistence of nanoscale solvent- and solute-rich crystalline structures)
- **Region D**: Classical nanostructured systems (nanoscale solvent-rich grains with solute segregating at grain boundaries)

and will be explored in more detail in later sections.

2.3. Systems without stable nanostructured states

Systems that do not exhibit stable nanostructured states generally exhibit low grain boundary segregation tendency relative to bulk phase separation, i.e. $\frac{\Delta H^{\text{seg}}}{\Delta H^{\text{mix}}} < 1$, or $\omega_{\text{gb}} > 0$ for our alloy systems. In this section we begin with a brief examination of the first two structures, labeled A and B. These structures are similar in that they involve systems where grain boundary segregation is not expected to be energy lowering, and they exhibit bulk ground states.

Depending on the relative severity of the phase separation tendency and the grain boundary energy penalty, instability can manifest in several ways including the structures in Figure 2.10, all of which display no apparent solute segregation at grain boundaries. For structure A, at low ΔH^{mix} and ΔH^{seg}, the grain boundary energy penalty is greater than the enthalpic terms and therefore all grain boundaries are higher in energy than grain interior bonds. A nanostructure cannot be maintained in this "bulk system" regime, highlighted in red in Figure 2.9. The representative alloy system A in Figure 2.10(a) displays bulk solid solution structures at low solute concentrations, and precipitation emerges at higher alloy contents beyond the solubility limit; in all cases the system has only a single grain once equilibrated.

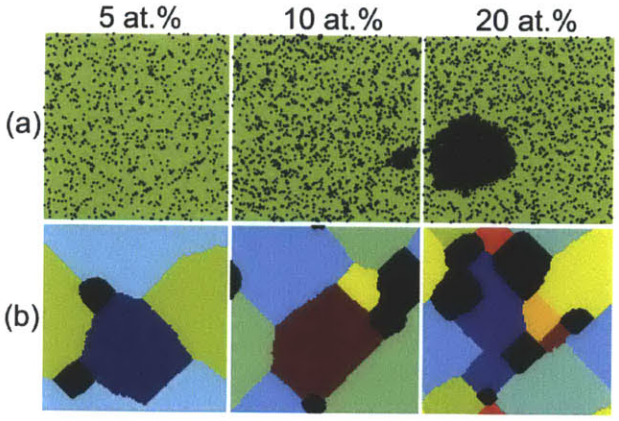

Figure 2.10: Systems with no stable nanostructured state at 500°C. (a) System "A" with ΔH^{mix} = 20 kJ/mol ΔH^{seg} = 15 kJ/mol forms single crystalline solid solutions with precipitation emerging at 10 at.% solute concentration. (b) System "B" with ΔH^{mix} = 100 kJ/mol and ΔH^{seg} = 65 kJ/mol exhibits phase separation with no solute segregation at grain boundaries.

For structure B in Figure 2.10(b), the system equilibrates to a polycrystal with phase separation. Although there are grain boundaries present they are not decorated with solute in concentrations above those in the bulk solution. In this regime, highlighted in yellow in Figure 2.9, the single-component grain boundaries have a bond energy with a magnitude between that of

the bulk solid solution, E_c^{AB}, and bulk phase separation, E_c^{AA}, bonds. As a result, bulk phase separation is the preferred condition, but single-component grain boundaries may persist in an entropically stabilized condition.

2.4. Duplex nanostructures

Traversing from lower-right to upper-left in Figure 2.9, there is a transition between the bulk-stable conditions described above and the green region where nanocrystalline structures may emerge. The blue region in which alloy C resides is a transition region between these behaviors; here the solute-segregated grain boundary is a low energy configuration compared to unalloyed grain boundaries, but higher in energy compared to bulk phase separation. A nanostructure can exist if solute-segregated grain boundaries are preferred over bulk solid solution, or in energetics terms when $\frac{-2\Omega^A\gamma_0^A}{zt} < \omega_{gb} < \frac{-2\Omega^A\gamma_0^A}{zt} + \omega_c$, highlighted in blue in Figure 2.9. The "duplex nanostructures" from alloy C, shown in Figure 2.11, display a nanocrystalline structure at low solute concentrations, and become a duplex nanocrystalline structure with solvent-rich and solute-rich crystalline regions and solute segregation at grain boundaries at higher solute concentrations. The overall grain boundary fraction is only 15 – 40% and does not vary significantly with composition. The grain size can be moderately controlled by the solute composition; by adding more solute, the system can access a higher fraction of relatively low energy E_{gb}^{AB} and therefore maintains a smaller grain size. However, phase separation would also be more severe as the composition increases.

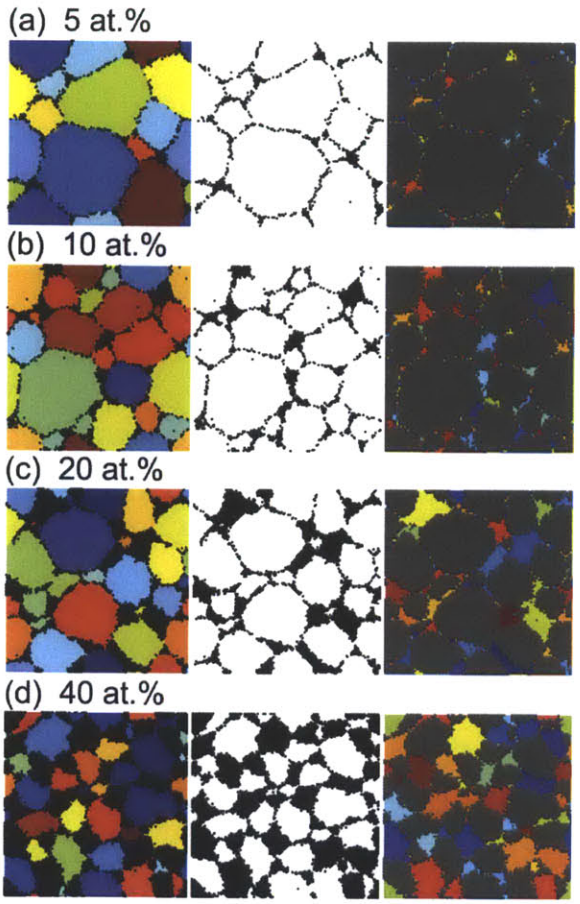

Figure 2.11: Duplex nanocrystalline structures from system "C" at 500°C with (a) 5 at.% (b) 10 at.% (c) 20 at.% and (d) 40 at.% solute content from a 100 x 100 x 6 BCC lattice with ΔH^{mix} = 50 kJ/mol and ΔH^{seg} = 65 kJ/mol. The solute atoms are presented in black in the first and second columns with and without the grain structure, respectively. The grain structure of the solute-rich regions is displayed with solvent atoms highlighted in gray in the third column. The solute-rich regions remain crystalline at all concentrations.

2.5. Classical nanostructured alloys

Alloying can lower the energy penalty of a grain boundary when ω_{gb} is negative, or $\frac{\Delta H^{\mathrm{seg}}}{\Delta H^{\mathrm{mix}}} > 1$ for our alloy systems. An ideal case is when solute segregation at grain boundaries creates the lowest energy state among all bond types, ultimately making a nanoscale grain structure the ground state. This condition is characterized by $\omega_{\mathrm{gb}} + \frac{2\Omega^{\mathrm{A}}\gamma_0^{\mathrm{A}}}{zt} < 0$ and highlighted in green in Figure 2.9. The representative alloy D in this "classical nanostructured" region has bond energies that are ordered $E_{\mathrm{c}}^{\mathrm{AB}} > \left(E_{\mathrm{gb}}^{\mathrm{AA}} = E_{\mathrm{gb}}^{\mathrm{BB}}\right) > \left(E_{\mathrm{c}}^{\mathrm{AA}} = E_{\mathrm{c}}^{\mathrm{BB}}\right) > E_{\mathrm{gb}}^{\mathrm{AB}}$; solute segregated grain

boundaries are preferred over bulk phase separation, and undecorated grain boundaries over bulk solid solution.

Some typical nanostructures that emerge in system D are shown along the bottom of Figure 2.12, in panels d-f. Here we observe polycrystalline structures that are clearly decorated at the boundaries with solute, and as more solute is available, the grains become finer to accommodate it. This is classical nanostructure stabilization of the kind envisioned by Weissmuller [28, 35], Kirchheim [30, 31], and also Detor, Trelewicz, and Schuh [1, 36, 38]. The notion that such nanostructures are formally the system's ground state presents an interesting alternative to conventional bulk materials thermodynamics, and proposes a major correction to, e.g., the assembly of binary alloy phase diagrams. As such, it is instructive to examine the energetics and structural degrees of freedom of such materials with the present MC model, where we can independently manipulate the structural constituents and explore the nature of these nanocrystalline ground states.

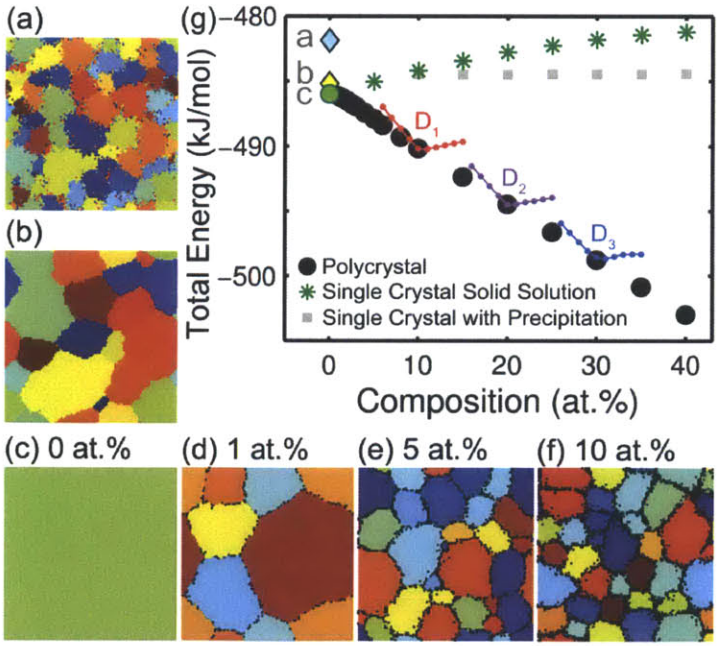

Figure 2.12: The structures and total system energy of system "D" with 0 – 40 at.% solute. For the unalloyed material, the system energy reduces upon cooling from (a) a fine grained polycrystalline structure to (b) a coarse grained structure, and finally (c) a single crystal equilibrium state. The equilibrated structures are provided for (d) 1 at.%, (e) 5 at.%, and (f) 10 at.% alloys, along with (g) an inverse relationship between the total system energy and the solute content. With increasing solute content, the system energy is lowered and a smaller average grain size can be accessed. The energies of alloys with a static grain structure but varied solute concentration are also provided, indicating that for

a grain structure there is a certain global concentration needed for the system energy to be minimized. The energies of single crystal structures are provided as a reference; for a single crystal structure, bulk precipitation emerges at 10 at.% composition and provides lower-energy states compared to a single crystal solid solution. Simulations are performed on a 100 x 100 x 6 BCC lattice with ΔH^{mix} = 20 kJ/mol, ΔH^{seg} = 65 kJ/mol, and T = 500°C.

2.5.1. System energy

First, we compare the structure and total energy of alloy D after equilibration at 500°C with those of the unalloyed material under the same conditions. The sequence of panels a-c in Figure 2.12 shows the evolution of the unalloyed structure upon cooling. As expected, the grain structure is initially a fine grained polycrystal (a) which coarsens (b) until the single-crystal ground state is achieved (c) over the course of the cooling process. In panel g, the total system energy is shown for these structures, and the monotonic drop from points 'a' to 'c' corresponds to the coarsening process; the total energy at point 'c' represents the lowest energy that can be achieved in the unalloyed condition.

Next, we consider the addition of solute atoms. Before considering the nanocrystalline systems, it is instructive to consider the energy of a single crystalline system that is alloyed; such systems are produced by the same equilibration process but with only a single (unchanging) grain number used for the whole MC lattice. The asterisk data points in Figure 2.12(g) show the energy of such single crystalline alloys. Even though the single crystalline alloys are equilibrated without the presence of grain boundaries, solute precipitation is still a possible competing bulk state. Given their equal enthalpy of mixing, the single crystalline behaviors of alloy D are identical to those of alloy A shown earlier in Figure 2.10(a). We observe precipitation of solute emerging at 10 at.% concentration in both systems, with a plateau of lower-energy states (presented in square data points) from precipitation. The energies of a single crystalline random solid solution are also provided by the asterisk data points in Figure 2.12(g) as a reference. Their values increase slightly with alloying level; this is expected since the alloy in question has a modest positive enthalpy of mixing.

Compared with any of the above results on alloyed or unalloyed single crystals, the system energy can be lowered even further to achieve unique ground states when the grain structure is allowed to remain polycrystalline in the alloyed systems. The series of panels d-f show the resulting equilibrated structures, which, as noted earlier, are characterized by grain

boundary segregation. What is clear now by comparison of the data in Figure 2.12(g), is that these structures are of lower energy than any single crystal solid solution in this alloy system; these are thermodynamically stable nanocrystalline structures in which grain growth at constant composition is an energy raising proposition.

The black data points in panel g show a linear decrease in energy with composition, which is in line with analytical calculations in Ref. [62]. What is more, these structures (cf. Figure 2.12(d), (e) and (f)) exhibit smaller average grain sizes with increasing solute content. This is made more explicitly clear in Figure 2.13(a), which shows an inverse relationship between grain size and composition as expected in this regime; solute excess drives the system toward grain boundary retention rather than solvation or precipitation. Here the average grain size is calculated from the diameter of volume-equivalent cylinders and converted to the nanometer scale using the lattice parameter of 3.16 Å.

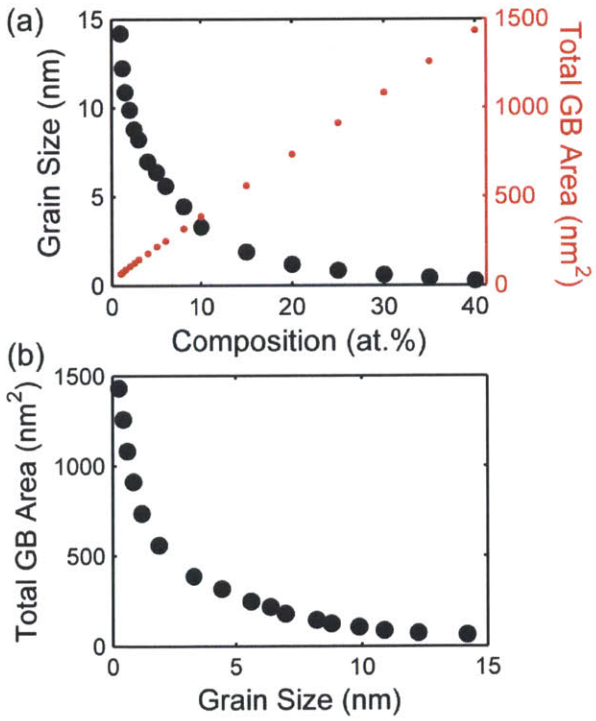

Figure 2.13: (a) Inverse relationship between average grain size and solute content in the classical nanostructured alloy D with 1 – 40 at.% solute concentration at 500°C, shown with the associated change in total grain boundary area. (b) The total grain boundary area increases as the average grain size decreases with solute addition.

2.5.2. Reduction in grain boundary formation energy

The equilibrium condition for closed alloy systems with grain boundaries is the one in which the total system energy is minimized with respect to any change in grain size, i.e., $\frac{dG}{dA} = 0$. The equilibrated structures in Figure 2.12 and Figure 2.13 all must satisfy this condition. There is opportunity for confusion in closed systems because $\frac{dG}{dA}$ is not equal to γ, and both quantities are occasionally called "grain boundary energy". To clarify the relationship between these variables and to more clearly elaborate their circumstances in equilibrium, we proceed to directly evaluate them from the simulated structures.

We call γ the "grain boundary formation energy", and it is the difference between the energy of a grain boundary structure and that of a perfect crystal normalized by the total grain boundary area [36, 63]:

$$\gamma = \frac{\Delta E_{\text{defect}} - \Delta E_{\text{ideal}}}{A_{\text{defect}}} \tag{2.12}$$

where ΔE_{defect} and ΔE_{ideal} are respectively the formation energies of the polycrystal and a single crystal and A_{defect} is the total grain boundary area in the polycrystal. The single crystal must possess the same chemical ordering (chemical potentials) as the defected structure such that the energy difference results only from topological defects [36]. By replacing all grain numbers in the equilibrated alloy structure with a single value, a single crystal with the same chemical distribution as the original alloy structure can be obtained, based on which ΔE_{ideal} may be calculated. The total grain boundary area can be obtained by replacing all atoms in the alloy with the solvent, thus creating a pure polycrystal with the identical grain structure, and calibrating it using Equation (2.12) with the formation energy of a pure single crystal (as ΔE_{ideal}) and the grain boundary formation energy of the pure metal. After obtaining ΔE_{ideal} and A_{defect} of the alloy, the total energy of the equilibrated alloy is used as ΔE_{defect} and the alloy grain boundary formation energy can be calculated.

Upon increasing the solute content, a higher fraction of grain boundaries exists in equilibrium to accommodate the solute, and Figure 2.13 shows a monotonic increase in the total grain boundary area, or A_{defect}, as the concentration increases (Figure 2.13(a)), or as the grain size is refined (Figure 2.13(b)). The reduction of the grain boundary formation energy is presented in Figure 2.14, on both linear (a) and logarithmic (b) scales with composition. On the logarithmic scale the alloy grain boundary formation energy displays a nearly linear trend with composition,

as expected (at least in the dilute limit) from Equation (1.2). The grain boundary specific solute excess, Γ, is estimated from the best fit line in Figure 2.14(b) to be approximately 36-49 atoms/nm^2, which is a physically reasonable value.

At 0 at.% concentration, the grain boundary formation energy is 1.11 J/m^2 which matches the input γ_0 value. After alloying, the grain boundary formation energy is reduced significantly *below* zero. It has been pointed out in a discussion of Kirchheim and Gottstein [39, 40] that for closed systems, the first two terms on the right hand side of Equation (2.2) are positive but their magnitudes are small. In order to attain equilibrium ($\frac{dG}{dA} = 0$), the grain boundary formation energy, γ, then must be negative. The negative values of γ obtained in Figure 2.14 are thus expected. The implication of a negative alloy grain boundary formation energy is not that unchecked creation of grain boundaries is preferable, but rather that a very specific solute-segregated grain boundary configuration can reduce the system energy according to Equation (1.1). Such configuration depends in detail on the solute concentration according to Equation (1.2). The fraction of decorated grain boundaries in the equilibrium state is limited by the amount of solute available in the system. Any grain boundary area created beyond the capacity of solute to stabilize them would annihilate in equilibrium because of the energy penalty from $\gamma_0 A$.

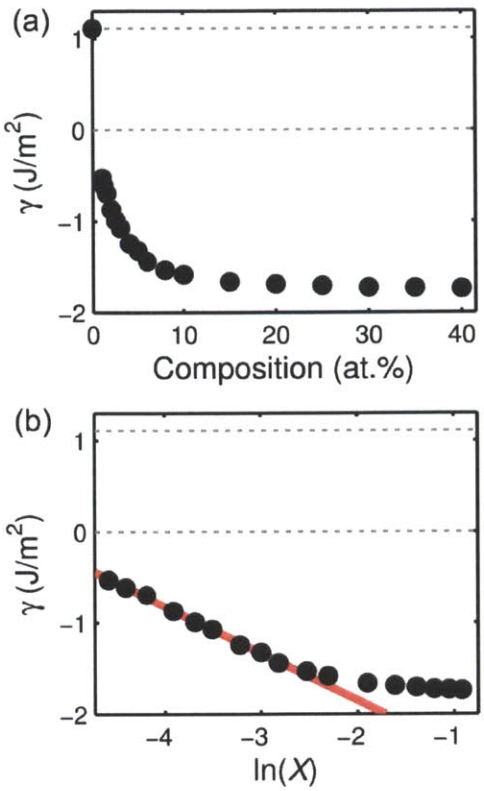

Figure 2.14: Reduction in grain boundary formation energy with solute addition. In the classical nanostructured alloy D, the grain boundary formation energy is reduced to a negative value, indicating that these nanocrystalline alloys are lower in energy than their single crystalline counterparts. The variation between the effective grain boundary formation energy and ln(X) is almost linear as expected at dilute concentrations. The pure-component grain boundary formation energy of 1.11 J/m^2 and zero grain boundary energy are noted by the dotted lines.

To further elucidate this concept, we use our simulation to compare the total energy of alloy D when the composition is fixed at 5 at.% but the grain size is varied away from the equilibrium value. This is accomplished by using equilibrated grain structures obtained from those in Figure 2.12, at a variety of compositions that effect different grain sizes (Figure 2.13). These structures then have their chemical composition reassigned to a value of 5 at.% solute, before the structures are equilibrated isothermally at 500°C, while fixing the grain structure. In this way we fix a nanoscale grain size and explore the preferred solute configuration on that structure, with results as shown in Figure 2.15.

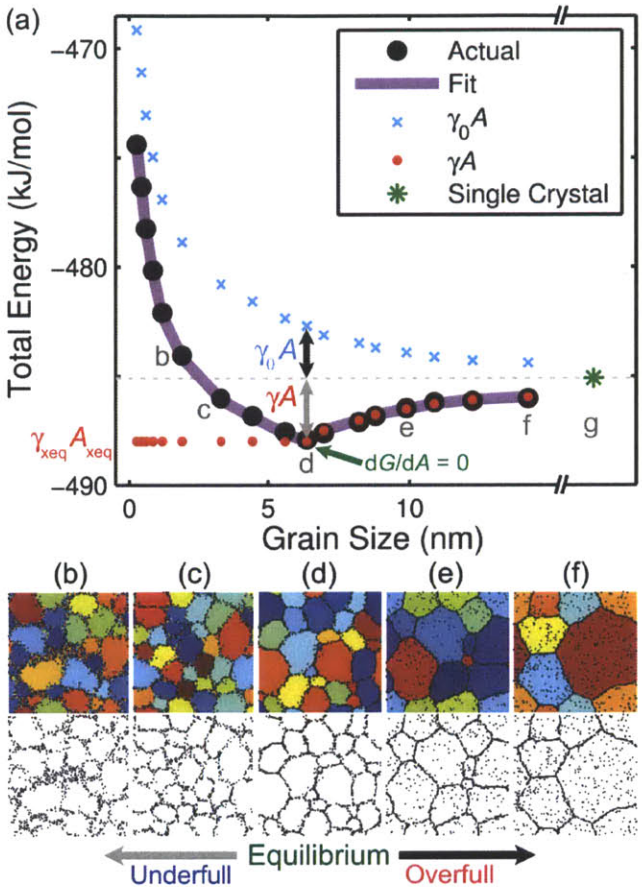

Figure 2.15: (a) Total system energy of 5 at.% classical nanostructured alloys from system "D" with various pre-determined average grain sizes. The system energy is minimized at point 'd' with the grain structure obtained from the equilibrium 5 at.% alloy. The structures with smaller or larger average grain sizes are observed to have higher energy with underfull and overfull solute segregated grain boundaries, respectively. With the energy of a single crystalline solid solution under the same conditions, denoted by 'g', as the reference state, the energies of alloys with equilibrium and overfull grain boundaries are lowered by $\gamma_{\mathrm{xeq}}A$ via grain boundary segregation, while the alloys with underfull grain boundaries possess both energy increment and penalty of the magnitude $\gamma_{\mathrm{xeq}}A_{\mathrm{xeq}} + \gamma_0(A - A_{\mathrm{xeq}})$. The structures of 5 at.% alloys after equilibration are provided for the original grain structures from (b) 15 at.%, (c) 10 at.%, (d) 5 at.%, (e) 2 at.%, and (f) 1 at.% alloys. Simulations are performed on a 100 x 100 x 6 BCC lattice with $\Delta H^{\mathrm{mix}} = 20$ kJ/mol, $\Delta H^{\mathrm{seg}} = 65$ kJ/mol, and $T = 500$°C.

The solid data points in Figure 2.15 show the raw output of these simulations, giving the total system energy as a function of grain size at fixed composition. With no precipitation and therefore a negligible change in entropy, the slope of this data is $\frac{\mathrm{d}G}{\mathrm{d}D}$, with D the grain size, and is related to $\frac{\mathrm{d}G}{\mathrm{d}A}$ as $\frac{\mathrm{d}G}{\mathrm{d}A} = \frac{\mathrm{d}G}{\mathrm{d}D}\frac{\mathrm{d}D}{\mathrm{d}A}$, with the functional form between A and D presented in Figure 2.13(b). These data show an energy landscape that is reminiscent of those proposed by

Weissmuller [28, 35] and others [38], which decreases to a minimum value before rising again. Even though all of the obtained final structures are energy minimized with respect to the chemical distributions in their present grain structures, the true minimum energy can only be achieved at a specific grain size, shown in Figure 2.15(d), where the grain structure is obtained from the equilibrium 5 at.% alloy structure, which is exactly the point where $\frac{dG}{dD} = \frac{dG}{dA} = 0$.

When a grain is smaller than the equilibrium grain size, there is an energy excess in grain boundaries that are not decorated by the solute and therefore exist in a high-energy state; grain growth towards the equilibrium value is preferred. On the other hand, when the average grain size falls above the equilibrium value, all grain boundaries are decorated but there are grain interior bonds that could exist in an otherwise lower-energy solute-segregated grain boundary configuration, if there only were grain boundary sites to accept them. The balance between underfull and overfull grain boundary networks results in a specific equilibrium grain size. The fine-grained equilibrium structure in Figure 2.15(d) possesses a lower energy than its single crystalline counterpart, denoted by the asterisk labeled 'g'.

With a single crystal as the reference state, grain refinement raises the system energy by $\gamma_0 A$ from the increase in total grain boundary area, and when alloyed, counteracted by γA from the reduced equilibrium grain boundary formation energy. Based on the free energy expression in Equation (1.1) and a single crystal solid solution with energy $\Sigma\mu_i N_i$ as the reference state, these two terms ($\gamma_0 A$ and γA) are isolated and plotted in Figure 2.15 along with the actual system energy obtained from our simulated alloy structures. For grain sizes above the equilibrium value, all grain boundaries are stabilized; the grain boundary formation energy γ is thus the equilibrium grain boundary formation energy of the 5 at.% alloy and A is the total grain boundary area at each grain size. However, for the grain sizes below the equilibrium value, only a fraction of grain boundaries are decorated and stabilized by the solute, and therefore γA is fixed to the value of the equilibrium 5 at.% alloy. The remaining grain boundaries are undecorated and possess the energy penalty from γ_0. The overall energy is thus $G = \Sigma\mu_i N_i + \gamma_{xeq} A_{xeq} + \gamma_0 (A - A_{xeq})$, where the subscript denotes the equilibrium concentration (5 at.% in this case). The resulting energy function provides a good fit for the total energy of our alloy structures.

As a complementary line of logic to the above, a static grain structure can be equilibrated with the solute composition varied. The subplots in Figure 2.12(g) labeled 'D_1', 'D_2', and D_3'

represent the energies of alloys with a fixed grain structure but different solute concentrations specified by the x axis. The results show three energy minima that align with the equilibrium data points in black, suggesting that for a certain grain structure (or its representative D), there is a specific global solute concentration needed to achieve grain stability. The two types of energy minima, with varying X at a fixed D in Figure 2.12(g) and with varying D at a fixed X in Figure 2.15, are in line with the one-to-one relationship between global solute concentration and equilibrium grain size presented earlier in Figure 2.13(a) and the consequent control of grain size via solute concentration in these classical nanostructured alloys.

With solute-segregated grain boundaries being preferred over phase separation, and with an excessive amount of grain boundaries induced by the solute, the structures of alloy D from the classical nanocrystalline regime can display an amorphous-like structure at the highest solute concentrations. Due to the nature of our fixed lattice simulation, an amorphous structure is not explicitly captured as a state of disordered atomic packing, but rather as a system in which individual grains are so small as to defy definition as crystals (i.e., no larger than a few atoms). This is captured by a high volume fraction of atoms coordinating grain boundaries, as shown quantitatively in Figure 2.16. All atoms have at least one grain boundary bond at 50 at.% concentration. This amorphous-like structure is in line with the analytical thermodynamic calculations from Refs. [28] and [62], which suggested that there is a terminal concentration at which a nanocrystalline state can exist, and above which the grain size refines to the order of the grain boundary thickness and an amorphous phase can emerge close to the equiatomic concentration.

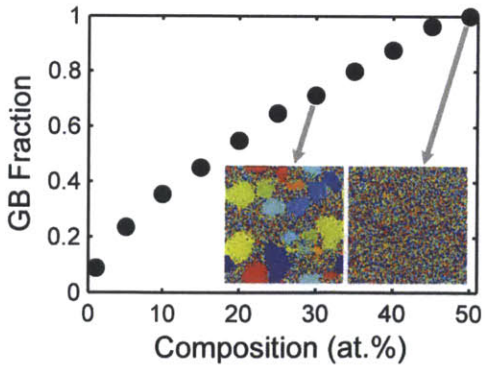

Figure 2.16: The grain boundary fraction increases with solute content in the classical nanocrystalline alloys. The grain structures, provided in the insets, are composed of a

large volume fraction of grain boundaries at high solute compositions and eventually become all grain boundaries at 50 at.%.

2.6. Grain boundary formation energy and influence on nanostructure stability

The efficacy of solute in stabilizing a nanoscale grain structure is determined not only by the solute-solvent elastic mismatch, accounted for by ΔH^{seg} in our simulation, but also other effects including mixing (or precipitation) characteristics, accounted for by ΔH^{mix}, along with solute composition and system temperature. The alloy grain boundary formation energy, γ, can be used as measure of grain structure stability, i.e. how much energy reduction is achieved by alloying compared to a similar structure without grain boundaries. We can simulate various 5 at.% alloy structures with the material parameters from the systems marked in Figure 2.17 across all four different regimes of nanostructure behaviors and assess their stability via γ.

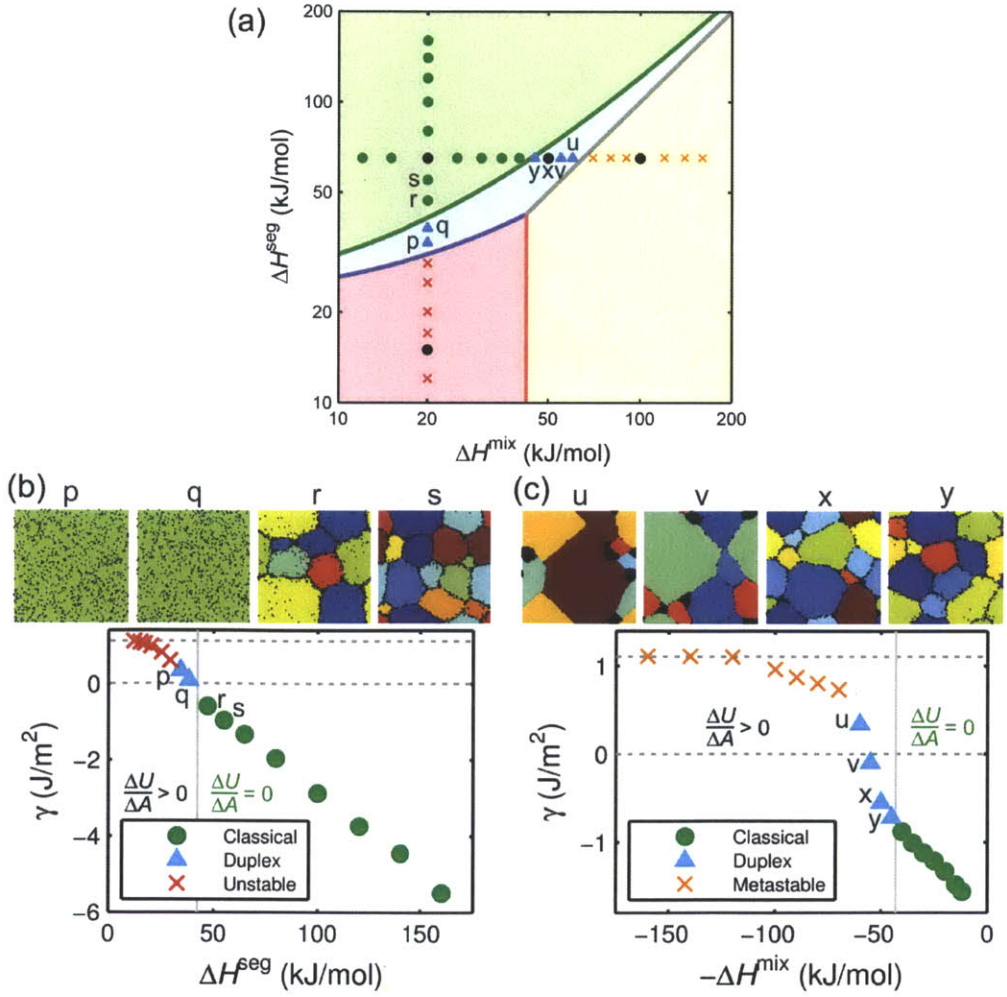

Figure 2.17: Grain boundary formation energies in alloys with 5 at.% solute addition. (a) The alloys from which the material parameters are taken are marked on the stability map. (b) With varying ΔH^{seg}, γ is equal to γ_0 in bulk systems and starts decreasing as we advance toward the classical nanostructured regime, where γ becomes negative. Similarly, with varying ΔH^{mix}, γ is significantly reduced below zero with alloying in the classical nanostructured region. Only those alloys from the classical nanostructured region have the free energy profile with a global minimum. Simulations are performed on a 100 x 100 x 6 BCC lattice and T = 500°C.

No precipitation is observed in the 5 at.% alloys with low ΔH^{mix} in Figure 2.17(b). The values of γ from the bulk systems at low ΔH^{seg} are obtained from their immediate structures before converging to single crystals. All of these unstable structures display a positive γ, indicating a higher energy polycrystalline state compared to their similar single crystalline structures. At higher ΔH^{seg}, the structures from the duplex region have lower, but still positive, γ. Their steady-state structures are single crystals (but duplex nanocrystalline at higher compositions, as shown in Figure A.3.). The grain boundary area potential $\frac{dG}{dA}$ is positive in these bulk and duplex systems, which is consistent with the absence of grain boundaries in their steady-state structures.

The structures from the classical nanostructured region in Figure 2.17(b) and (c) are all solid solutions with solute segregation at grain boundaries. These structures serve as examples of alloy systems that could be stabilized not only against grain growth but also phase separation. All stable classical alloys have a negative γ and zero $\frac{dG}{dA}$, as expected in a thermodynamically stabilized grain structure.

With ΔH^{mix} varied at a constant ΔH^{seg} , the structures from the yellow-shaded region "B" in Figure 2.17(c) show reduction in γ from the reference metal value γ_0 but their magnitudes are all positive. The duplex structures with zero and positive grain boundary formation energies at relatively high ΔH^{mix} display solute precipitation while those with a negative γ remain in solution with solute segregation at grain boundaries, similar to the alloys from the classical nanostructured region. It is interesting to note that a nanoscale grain structure can be retained in a metastable manner with zero or slightly positive γ, however these particular structures also display phase separation. The energy reduction in these structures in fact results from phase separation more than grain boundary segregation.

2.7. Conclusions

We have developed a Monte Carlo simulation for the purpose of investigating polycrystalline alloys in which both the chemical configuration and grain structure are allowed to vary. The model is built in such a way that classical McLean-type grain boundary segregation and regular solution mixing are recovered in the proper limits. By using the simulation to visualize grain–atomic structures and study alloy energetics, grain stability is explored in phase-separating binary alloys with the following findings:

- Grain boundary segregation states in some alloys can be energetically favorable compared to any competing bulk states, and therefore a polycrystalline structure is the system's ground state.
- The distinction between what we call the "grain boundary formation energy", γ, and the "grain boundary area potential", $\frac{\mathrm{d}G}{\mathrm{d}A}$, in a closed system is clarified using simulation results. Whereas these two terms are both equivalent and called "grain boundary energy" in an open system, in a closed system γ is related to the energy change caused by topological defects and $\frac{\mathrm{d}G}{\mathrm{d}A}$ is related to the equilibrium grain size attainment.
- Upon alloying, a negative γ is physically plausible, and stability against both grain growth and phase separation can be achieved when γ is negative and $\frac{\mathrm{d}G}{\mathrm{d}A} = 0$ in closed systems.
- The free energy landscape and γ can both be modified via solute addition, as observed in different types of nanostructure behaviors with alloy material parameters (ΔH^{mix} and ΔH^{seg}) and control of equilibrium grain size via solute concentration.

Chapter 3: Synthesis and characterization of nanocrystalline W alloys

3.1. Alloying element selection

Prior to synthesis of nanocrystalline materials, we must first select one or more preferred alloying elements for enhancing grain stability. Even though our intended processing route based on powder processing requires relatively mild temperature exposure compared to other techniques, powder consolidation or sintering procedure is identified as the manufacturing step where the material is most susceptible to grain coarsening. As a result, our goal is to preserve the nanoscale grain structure at the typical tungsten sintering temperature of 1100°C through a period of time suitable for a full consolidation cycle. The thermodynamic framework introduced in Chapter 2 is applied in order to evaluate the stability of tungsten-based alloy systems at 1100°C, from the pool of candidate solutes for which materials data are available.

The nanostructure stability map in Figure 2.9 is constructed specifically for tungsten-based systems, and this map is reproduced here in Figure 3.18. By populating this map with the material parameters obtained from reference [64], the regions in Figure 3.18 classify the candidate solute into three main groups. The solute in the classical region, i.e. Mn, Sc, Th, Ti and Zn, and also the duplex region, i.e. Au, Cr and In, are potential contenders.

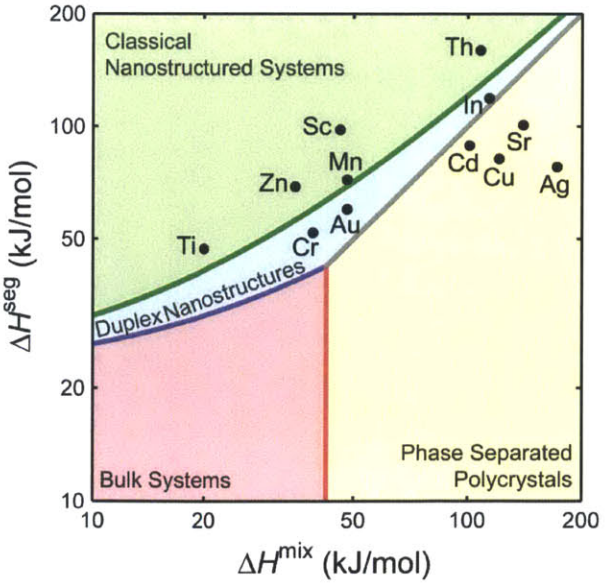

Figure 3.18: Nanostructure stability map for tungsten based alloys.

Our Monte Carlo simulation can be used to determine the equilibrium alloy configurations at 1100°C both visually and quantitatively. Before considering the alloy structures, a quantitative measure of grain stability may provide an overall understanding of the solute stabilizing capability. The grain boundary formation energy, γ, was measured in Monte Carlo structures using the same methods described in Chapter 2. This is shown for tungsten alloys with 2, 5, and 10 at.% solute concentration in Figure 3.19. It is significant that the values of γ are negative for all of those alloy systems that appeared in the "classical nanostructure" region of Figure 3.18. By contrast, the values of γ are only mildly negative for the duplex systems.

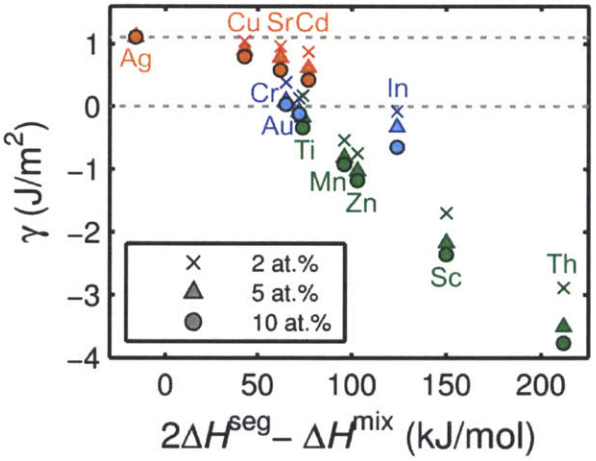

Figure 3.19: Reduction in grain boundary formation energy calculated from tungsten based alloys with 2, 5, and 10 at.% solute after equilibration at 1100°C. The colors indicate the stability region of the alloys.

A negative γ is required for grain stabilization via grain boundary solute segregation, and a more negative value of γ allows a higher fraction of grain boundaries in equilibrium according to Equation (2.2). The plot in Figure 3.19 is similar to those in Figure 2.17 but with a parameter ω_{gb} - ω_c, or its linearly and negatively proportional term $\Delta H = 2\Delta H^{seg} - \Delta H^{mix}$, on the x axis to represent the combined effects of ΔH^{mix} and ΔH^{seg}. This parameter is chosen particularly for the classical nanostructure alloys; Relief of interface energy penalty in these alloys is governed by the competition between formations of solute segregated grain boundary and bulk phase separation (represented by $\omega_{gb} + \frac{2\Omega^A\gamma_0^A}{zt}$), and also between formations of undecorated grain boundary and bulk solid solution (represented by $\frac{2\Omega^A\gamma_0^A}{zt}$ - ω_c). Thus, the correlation between γ

and the term ω_{gb} - ω_c should be monotonic for the classical nanostructured alloys, as observed by the linear trend in Figure 3.19 formed by the alloys from the classical region.

The visual representations of these tungsten based alloys created from the Monte Carlo simulation results show the expected structural features according to the stability region in Figure 3.18 in which each alloy resides. The classical nanostructured alloy structures in Figure 3.20 are solid solutions with solute segregation at grain boundaries. W-Au, -Cr, and -In alloys from the duplex region exist in solid solution with a propensity for both grain boundary solute segregation and nanoscale phase separation. Figure 3.21 shows solute segregation at grain boundaries, and also solute-rich nanocrystalline regions emerging as the solute concentration rises. Tungsten alloys with Ag, Cd, Cu and Sr form phase separated metastable polycrystalline structures with no apparent grain boundary solute segregation, as shown in Figure 3.22.

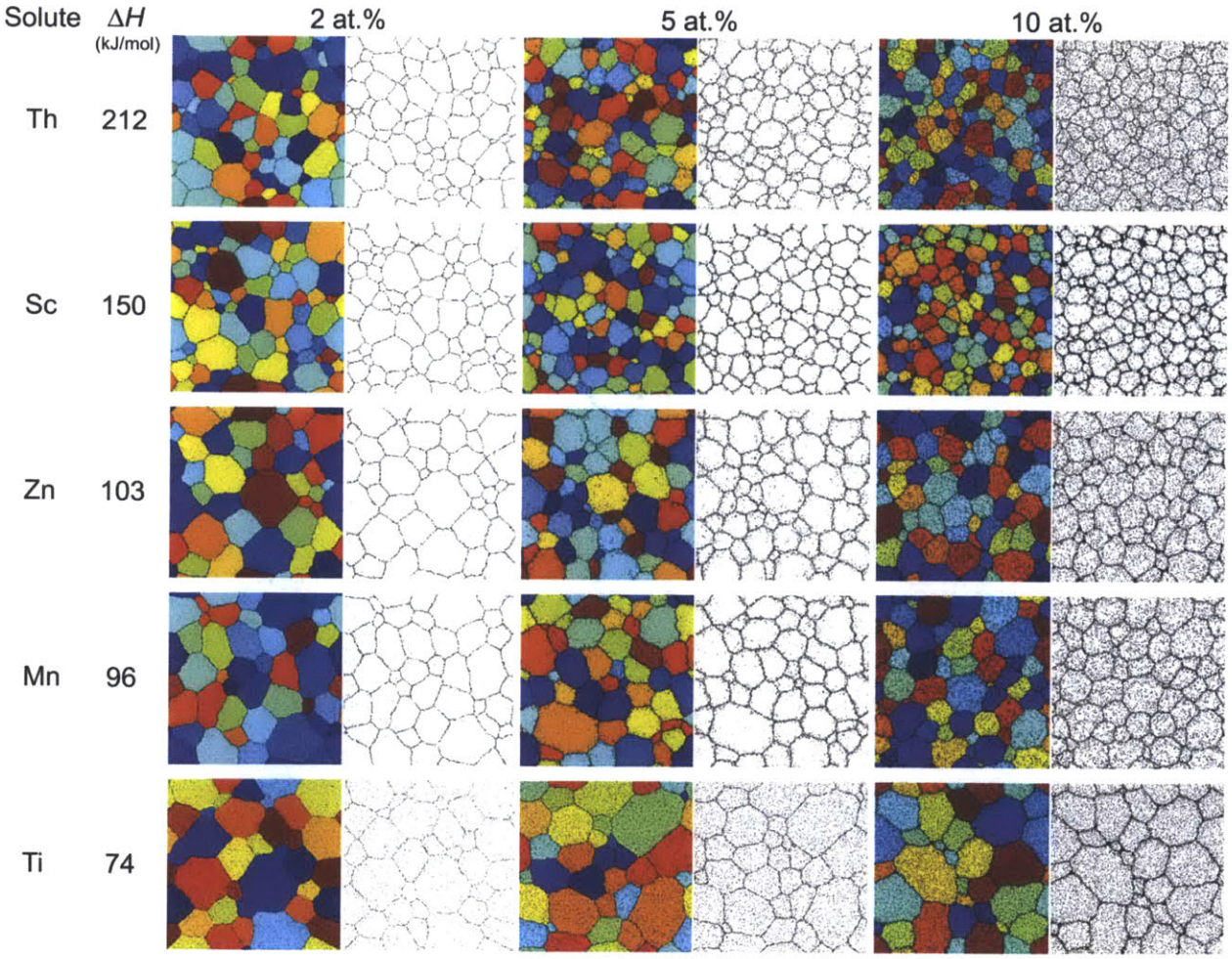

Figure 3.20: Grain structures and solute distributions of tungsten based alloys from the classical nanostructured region at 1100°C with 2, 5, and 10 at.% solute content from a

400 x 400 x 6 BCC lattice. All alloys are single-phase nanostructured solid solutions with solute segregation at grain boundaries.

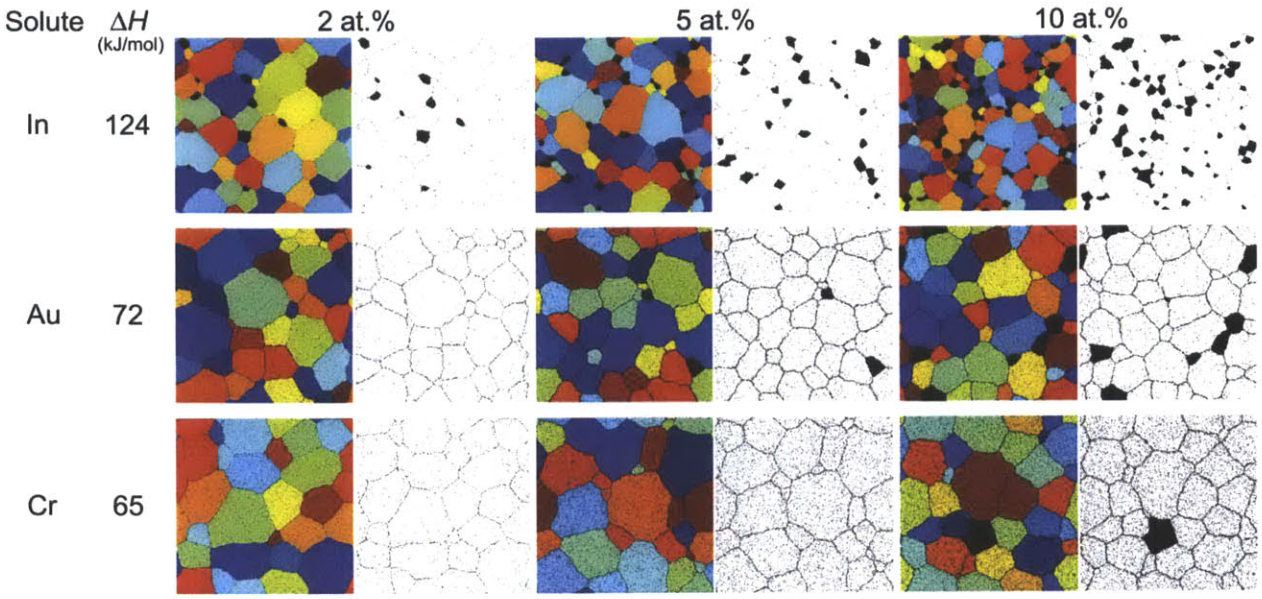

Figure 3.21: Structures of tungsten based alloys from the duplex nanostructure region at 1100°C with 2, 5, and 10 at.% solute content from a 400 x 400 x 6 BCC lattice. All alloys are nanostructured solid solutions with two apparent structural features. Solute atoms can segregate at grain boundaries or assemble into solute-rich clusters or precipitates, which become more evident as the solute concentration increases.

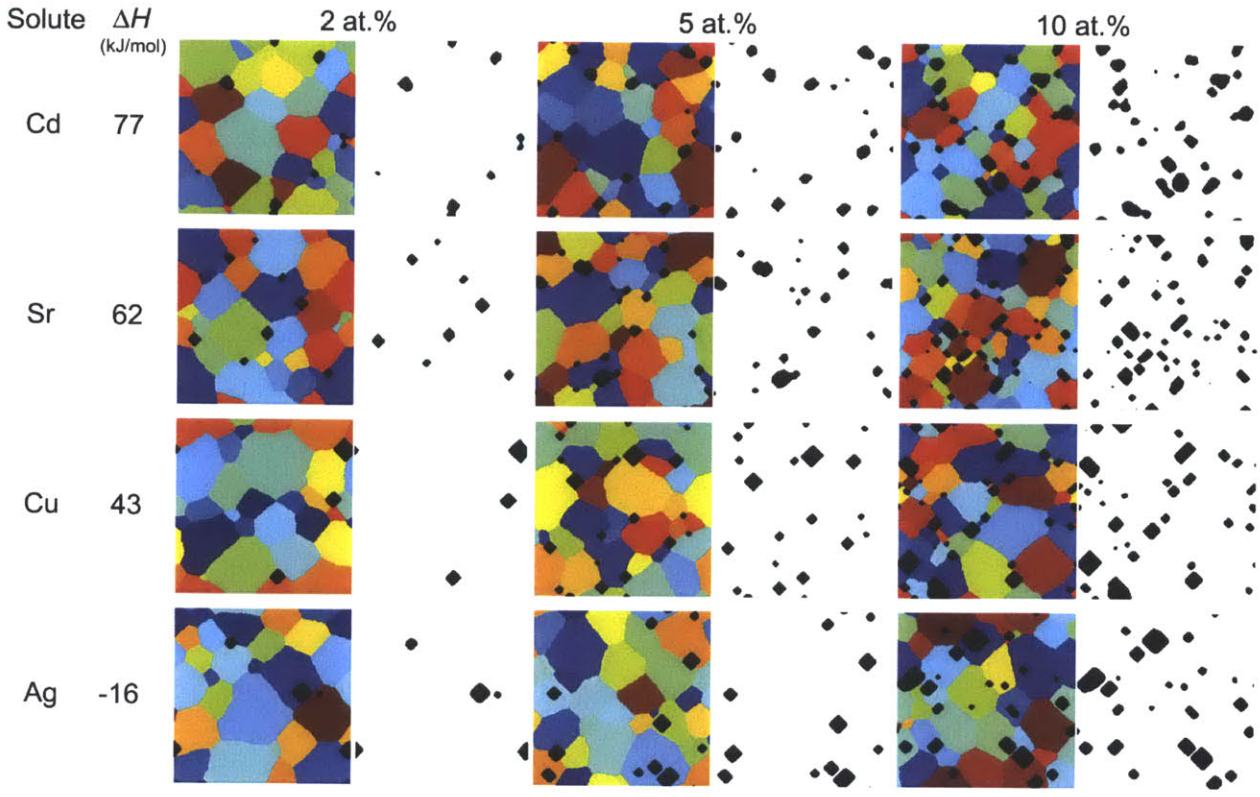

Figure 3.22: Structures of tungsten based alloys from the precipitated polycrystalline region at 1100°C with 2, 5, and 10 at.% solute content from a 400 x 400 x 6 BCC lattice. None of the alloys displays classical-type grain boundary segregation, but rather, several solute-rich precipitates are observed throughout the structure.

From Figure 3.19, within each stability region, γ displays a negative and monotonic correlation with $\Delta H = 2\Delta H^{\text{seg}} - \Delta H^{\text{mix}}$. The magnitude of this parameter is directly proportional to the reduction in γ, and a more negative value of γ (or a more positive ΔH) can be associated with a higher fraction of grain boundary in equilibrium, or in other words a smaller grain size. The order by which these alloy structures are listed in Figure 3.20, Figure 3.21, and Figure 3.22 is according to the value of ΔH. Thus, as we navigate down the list of the classical and also duplex alloy structures with decreasing ΔH, or less negative γ, the apparent average grain size is observed to increase. For all of these alloy systems with the exception of W-Ag, grain boundary formation energy can also be reduced with an increase in solute concentration as observed in Figure 3.19, and therefore, after the selection of a suitable alloying element for any processing requirement, the grain-atomic structure may still be modified via the solute concentration. For the classical nanostructured alloys in Figure 3.20, the grain structures become finer as the solute concentration increases.

With this information, several tungsten-based alloys can be processed and tested for high-temperature stability. Alloy systems that fall into the classical nanostructured region may be preferred for their lower chance of structural disruption from solute precipitation. Alloying elements that are potentially unsafe (Th) or not cost competitive (Au and Sc) are eliminated at this stage of solute selection. Among the remaining candidates, W-Ti is a preferred system for several reasons, including more available materials and phase diagram data compared to W-In, W-Mn, W-Zn, high intrinsic strength of Ti, and relatively simple phase equilibria between W and Ti. The phase diagram between W and Ti in Figure 3.23 show a high solid solubility and no competing intermetallic compounds.

Ti is also of interest because it runs counter to prior conceptions of what alloying elements would be preferred for nanostructure stabilization. Conventional approaches for solute selection generally prefer elements with a high atomic size mismatch or low solubility with the host atoms for their higher tendency to segregate at grain boundaries. In this particular pool of solute, the elements with the largest size mismatch with W (i.e. Sr with 55% size mismatch) and the lowest solubility in W (i.e. Ag and Cu, both with negligible solubility) fall within the precipitated polycrystal region of the nanostructure stability map.

Among the candidate solute in Figure 3.18, Ti is the alloying element with the lowest ΔH^{seg} and a low-to-moderate atomic size mismatch of 6% with W. At 1100°C, Ti has a particularly high 48 at.% solid solubility in W, as shown in the phase diagram in Figure 3.23. Yet, the placement of the W-Ti system is safe within the classical nanostructure region even after a consideration of the errors from ΔH^{mix} and ΔH^{seg} calculations. Moreover, Ti is a fast diffusing element so stabilization mechanisms based on kinetic drags is rather unlikely.

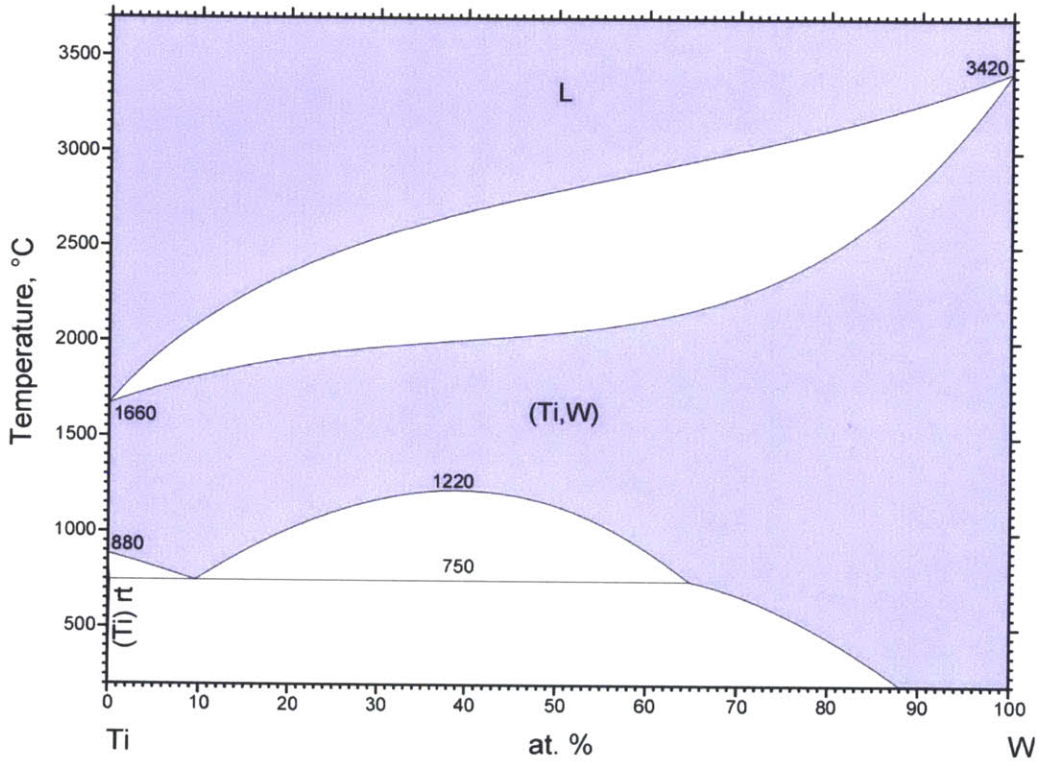

Figure 3.23: Phase diagram of W-Ti alloy [65].

3.2. Material processing

3.2.1. High-energy ball milling of tungsten

Severe plastic deformation via high-energy ball milling is selected as the powder processing method since alloying and grain refinement can be achieved simultaneously. The powders were processed in a SPEX 8000 high-energy ball mill using tungsten carbide media with a ball-to-powder ratio of 5 to 1. Ball milling was carried out in a controlled argon atmosphere in a glove box, and 1 wt.% stearic acid was used as the process control agent.

Tungsten powders were milled for 2, 4, 6, 8, and 10 hours and the resulting powders were characterized.

Stages of milling

Scanning electron microscopy (SEM) images in Figure 3.24 show the shape, size, and distribution of the milled particles at different milling times. Plate-like particles are present during the first four hours of milling, and from the sixth hour on, the powder particles become more equiaxed with minor change as milling progresses. The general mechanism of ball milling can be understood from the developments in particle size and geometry over time.

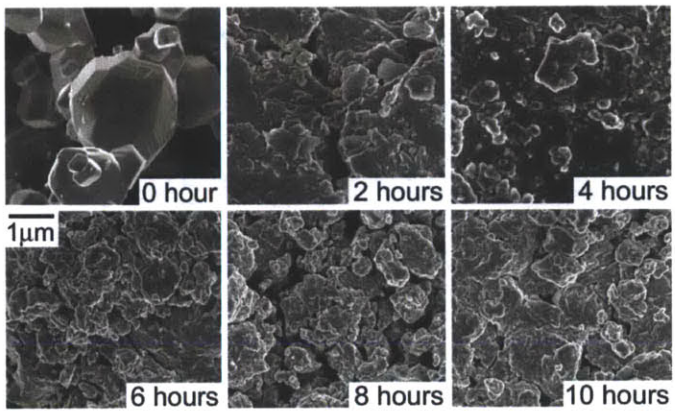

Figure 3.24: SEM micrographs of powder particles at different milling times.

During the first stage of milling, powder particles are flattened by microforging between the milling media, resulting in plate-like particles [66]. The increased surface area results in extensive cold welding between powder particles, causing a lamellar structure to develop. As the particles are continuously fractured and cold welded, lamellar colonies of random orientations are formed in each particle and the different atomic species continue to intermix. Further fracturing causes particles to become smaller and more equiaxed. As milling continues, the strength is increased by strain hardening. And hence, fracturing becomes dominant and the particle size decreases. Finally, a steady state between welding and fracturing is reached and the particle size saturates with time. The similarity in the overall size and shape in our ball milled tungsten powder at times after about the sixth hour (as observed in Figure 3.24) suggests a plateau in structural changes as a steady state is reached after about 4-6 hours.

Grain refinement with time

We use X-ray diffraction (XRD) to investigate the ball milled structures and the change in average grain size with time. The X-ray diffraction time-series in Figure 3.25 shows broadening of major tungsten peaks with milling time, particularly starting at six hours, due to the refinement of grain size and the lattice strain from plastic deformation. These traces also reveal minor peaks of tungsten carbide picked up from the milling media. The average grain size of tungsten is estimated using the Rietveld refinement method and Figure 3.26 shows the grain size significantly reduced below 50 nm after six hours of milling. However, as the milling time increases, the tungsten carbide peaks from the milling media become more noticeable. Therefore, in order to obtain nanocrystalline tungsten with a minimal amount of tungsten carbide contamination, six hours is selected as a preferred milling duration. The amount of microstrain shown in Figure 3.26 increases with milling as expected and the lattice parameter remains close to 3.165 Å which is the reference value for tungsten metal.

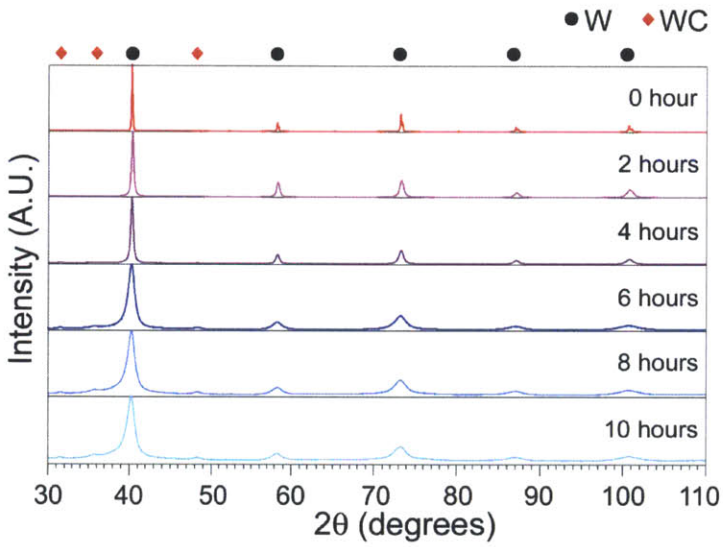

Figure 3.25: X-ray diffraction patterns of ball-milled tungsten at different milling stages. Broadening of tungsten peaks becomes more noticeable with the milling time.

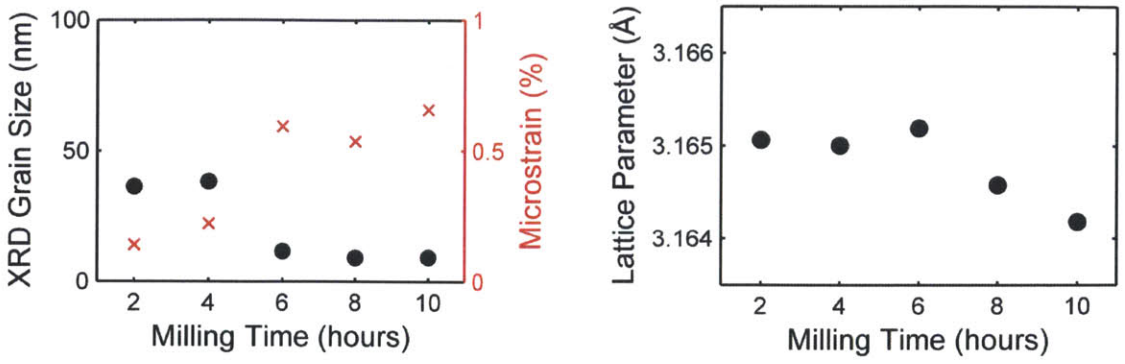

Figure 3.26: Average grain size, microstrain, and lattice parameter of ball-milled tungsten at different milling times from X-ray diffraction analysis. The average grain size is significantly refined after six hours of milling.

3.2.2. Synthesis and stability of tungsten-based alloys

Using the same ball milling procedure, solute can be added to the powder mixture and ball milled with tungsten to produce a nanocrystalline alloy. Samples with a 20 at.% addition of solute with a positive ΔH^{mix} with tungsten, i.e. Cr, Fe, Ti and V, were produced and tested for stability at 1100°C. After a 24-hour anneal in an argon atmosphere, the tungsten alloys were quenched to room temperature and characterized. The X-ray diffraction results in Figure 3.27 show a rough trend between thermal stability and increasing atomic size difference (with a positive value for a solute that is larger than tungsten). Among the metals with a positive ΔH^{mix} with tungsten and with reliable materials data, Ti exhibits better thermal stability compared to Cr (which agrees with our simulation results in Figure 3.19) and will be our choice of alloying element for further investigation.

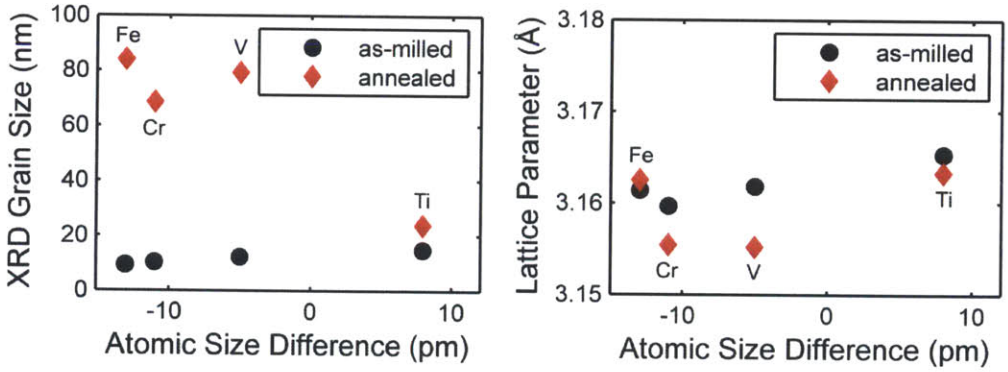

Figure 3.27: Average grain sizes and lattice parameters from X-ray diffraction analysis of tungsten-based alloys with a 20 at.% addition of the specified solute before and after annealing at 1100°C for one day.

3.3. Synthesis of W-Ti alloys

Tungsten samples with titanium content ranging from 0 to 20 atomic percent were ball milled for six hours using the same procedure outlined in section 3.2 and their structures after milling are characterized by the following two methods.

3.3.1. Characterization methods

X-ray diffraction

The X-ray diffraction patterns in Figure 3.28 show similar peak positions and peak profiles with the change in Ti composition. Using the Rietveld refinement method, the results in Figure 3.29 shows a general trend of decreasing grain size with increasing solute content, although the change is minor. There is no evident peak from titanium in these as-milled diffraction patterns; however the change in tungsten lattice parameter suggests that the addition of larger titanium atoms may slightly alter the tungsten host lattice in the as-milled state by possibly forming a substitutional solution. The peaks from tungsten-containing phases generally dominate peaks from other elements due to the high atomic number and therefore high scattering capability, or structure factor.

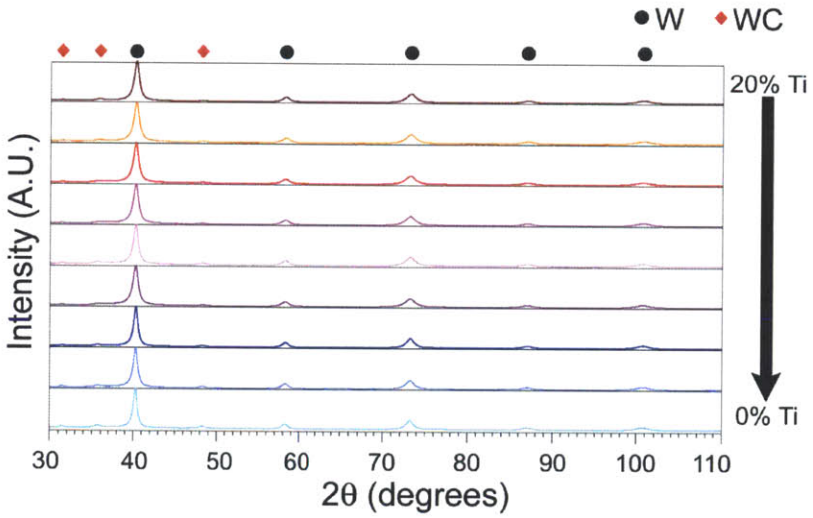

Figure 3.28: X-ray diffraction patterns of W-Ti alloys with 0-20 at.% Ti content. There is no significant change in peak profile with solute addition in the as-milled state.

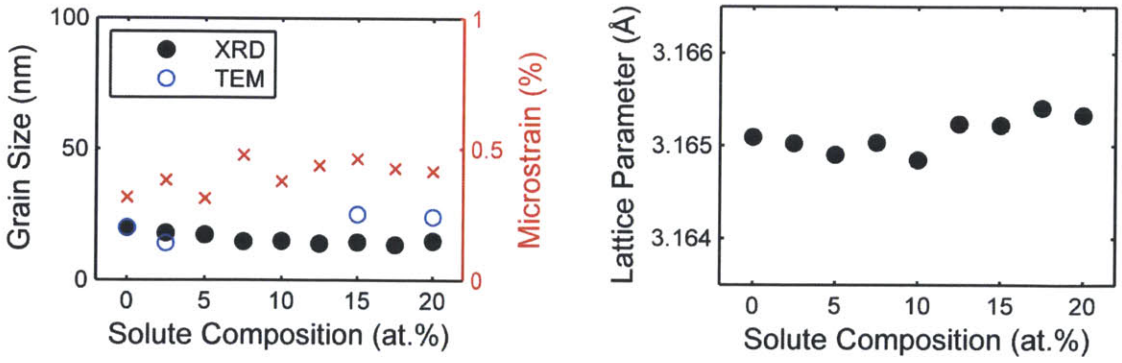

Figure 3.29: Average grain size, microstrain, and lattice parameters of as-milled W-Ti alloys with 0-20 at.% Ti addition from X-ray diffraction analysis. The average grain sizes from TEM observation are also provided.

Electron microscopy

The second method of grain structure characterization is by transmission electron microscopy (TEM). TEM allows direct observations of grain size, shape and distribution; however, preparation of TEM specimen from particulate materials can be challenging since their irregular surface and interparticle voids can give rise to nonuniform milling or etching rate. Furthermore, due to the high atomic weight of tungsten, electron transmission requires a particularly thin specimen. As a result, preparation of TEM specimens with a uniform thickness small enough for electron transmission is crucial.

Many of the common methods to prepare TEM specimens from powders were found ineffective for the present W-based materials. For example, particulate samples may be embedded in a media or binder material prior to TEM sample preparation, but preferential thinning can occur when the media is softer than the embedded powder; the present W powders are exceptionally strong and pose challenges to this method. Compaction of the powder into a bulk form was also ruled out because it may introduce a change in structure and mechanical state. Instead, the focused ion beam lift-out method was used to prepare TEM specimens from loose, uncompressed powder instead of the conventional argon ion milling that would otherwise require embedding or pressing the powder.

An FEI Helios NanoLab DualBeam focused ion beam (FIB) is used to prepare the samples for electron microscopy with the steps shown in Figure 3.30. The powder is planarized by a platinum protection layer, milled down to a thin membrane, lifted out by a manipulating probe, placed on a TEM grid and thinned down to electron transparency. The lift-out process provides a large uniform area of uncompressed powder with no external binding material available for TEM observation and structural analysis. Bright- and dark-field images from JEOL 2010F and JEOL 2011 transmission electron microscopes were obtained for grain structure observation and grain size measurement. The perimeter of each grain was traced and the grain size was calculated from the diameter of an area-equivalent circle.

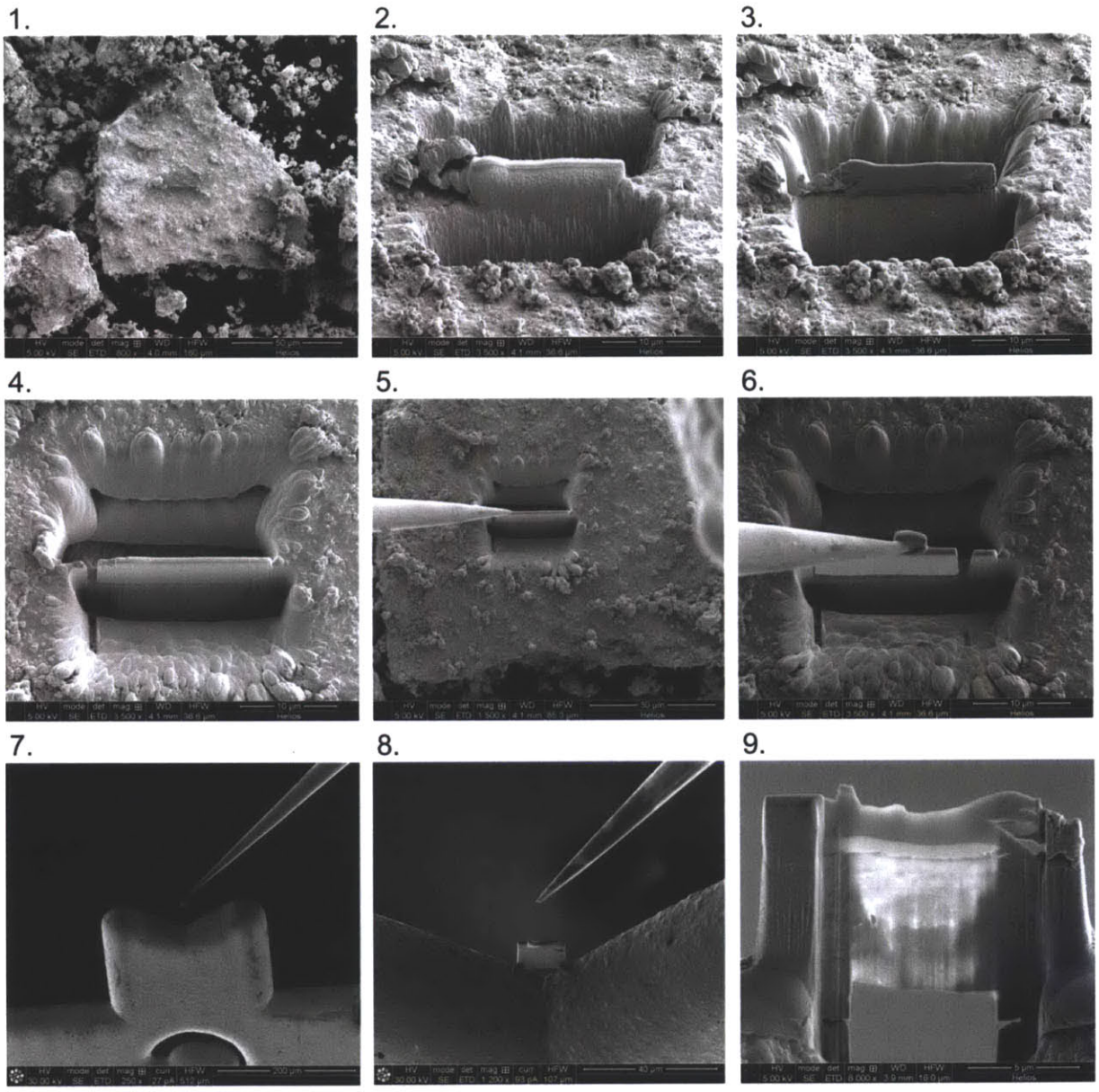

Figure 3.30: Lift-out procedure for TEM specimen preparation from loose powder.

3.3.2. As-milled grain structures

The complete grain size distributions are presented by the histograms in Figure 3.31 along with bright- and dark-field TEM images of tungsten and W-Ti alloys. All samples have grains that are smaller than 100 nm and an average grain size around 20 nm. The structures appear uniform and polycrystalline, as also confirmed by electron diffraction. In order to compare with the X-ray diffraction results, the XRD-equivalent 3/4 volume averaged grain sizes from the TEM measurements are plotted in Figure 3.29 [67]. Both methods of grain

characterization reveal only a slight change in the overall grain size with solute content in the as-milled state, as all samples are imposed with a similar degree of deformation from the same ball milling procedure. The structure could remain in an out-of-equilibrium state as a result of severe plastic deformation and the solute atoms do not display any noticeable influence at this stage.

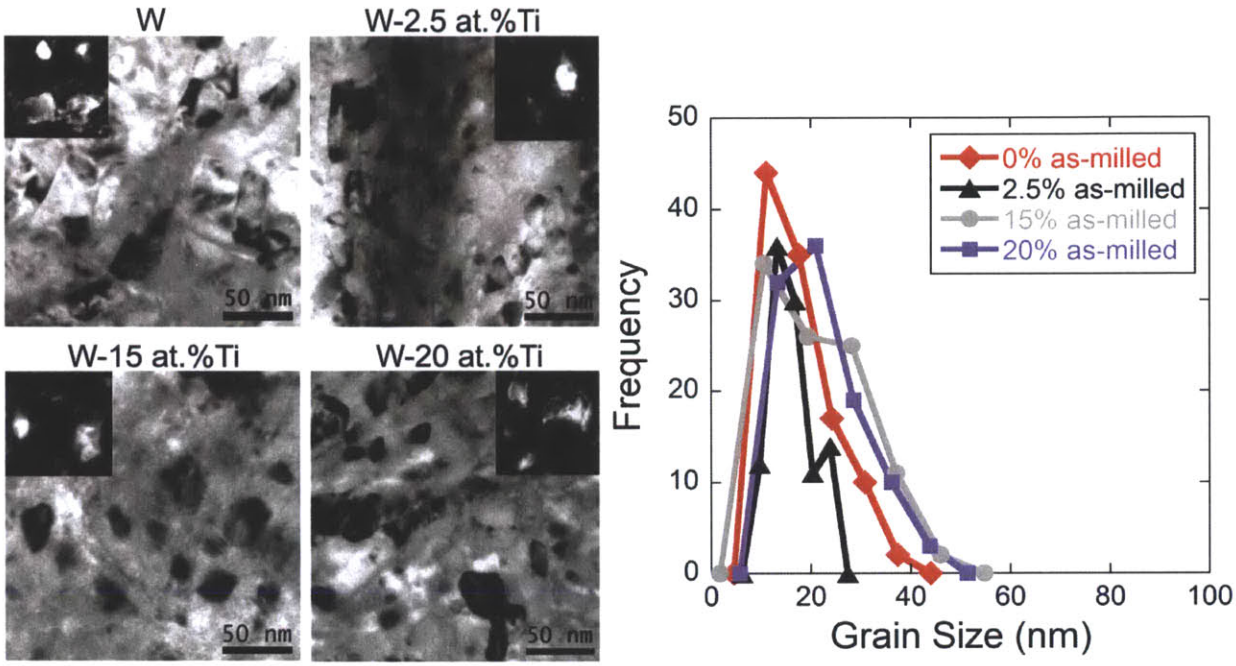

Figure 3.31: Bright-field TEM images with dark-field insets along with the grain size distributions from as-milled W specimens with 0-20 at.% Ti addition. The grain sizes are observed to be below 100 nm after milling.

3.4. Conclusions

Selection of a suitable alloying element for enhancing high-temperature stability of nanocrystalline tungsten with a focus on powder consolidation requirements is discussed based on simulation of alloy structures and specific material considerations. As an extension of the nanostructure stability map, which represents a general classification of nanostructure behaviors, a parameter ω_{gb} - ω_c, or in our study $2\Delta H^{seg} - \Delta H^{mix}$, is used as a quantitative representation of the solute's potential stabilizing efficacy, through the magnitude of reduction in the grain boundary formation energy.

Our choice of titanium as the alloying element is supported by both simulation results and the alloy screening experiment from the pool of candidate of various material parameters. The processing method of nanocrystalline tungsten by high-energy ball milling is established and

yields an initial average grain size of around 20 nm in both unalloyed and alloyed tungsten. Structural characterization by diffraction and microscopy methods reveals a uniform nanoscale grain structure with marginal change with solute concentration in the as-milled state.

Chapter 4: Thermal stability of nanocrystalline W-Ti alloys

Enhancing thermal stability is a considerable engineering leap toward practical nanostructured materials, especially for powder-route nanocrystalline metals which are susceptible to structural changes at the high temperature required for full-density consolidation. The results in Chapters 2 and 3 suggest that by adding a suitable alloying element, the energy penalty of grain boundaries can be reduced and a nanoscale grain structure can be retained. This concept is explored further with a focus on the extent of stability in terms of both temperature and time. By changing the alloying composition, control of structural stability for the temperature and the time duration needed for a specific processing or usage requirement may be possible. Diffraction and microscopy techniques can be used to investigate the extent and the nature of stabilizing effects of the added solutes.

4.1. Diffusion in W and Ti metals

Lee at al. reported two regimes of self-diffusion in polycrystalline tungsten [68]. In the lower temperature range of 887-1050°C, grain boundary diffusion is dominant with the grain boundary self-diffusivity of $D_{W,GB} = 1.41x10^{-5}*\exp(-294[kJ/mol]/RT)$ m^2/s, where R is the ideal gas constant. As the temperature increases, a change in diffusion mechanism is observed from grain boundary to lattice diffusion, which begins to dominate at 1600-1900°C, with the volume self-diffusivity of $D_{W,vol} = 4x10^{-6}*\exp(-525.9[kJ/mol]/RT)$ m^2/s.

The low-temperature hexagonal close-packed phase of titanium metal transforms to the BCC structure at 880°C and therefore titanium becomes dissolved in solid solution with BCC tungsten at elevated temperatures. The self-diffusivity of Ti at 1000°C is $D_{Ti,BCC} = 1.6x10^{-13}$ m^2/s, and at 1100°C is $D_{Ti,BCC} = 4.1x10^{-13}$ m^2/s [69]. Therefore, titanium is a fast diffusing element compared to tungsten. The diffusion distances, calculated from the square root of the product of diffusivity and diffusion time, are listed in Table 4.2 by both grain boundary and volume pathways at 1000°C and 1100°C.

Table 4.2: Diffusion lengths of W and Ti in the grain boundary and grain interior paths.

Temperature (°C)	$L_{W,GB}$ t=1 day (μm)	$L_{W,GB}$ t=1 week (μm)	$L_{W,vol}$ t=1 day (nm)	$L_{W,vol}$ t=1week (nm)	$L_{Ti,vol}$ t=1 day (μm)	$L_{Ti,vol}$ t=1 week (μm)
1000	1	2.7	0.01	0.03	118	311
1100	2.8	7.5	0.06	0.15	188	498

In our temperature range of interest, grain boundary diffusion is the dominant diffusion path in tungsten. The diffusion distances after 1 day at 1000°C and 1100°C are on the order of micrometers and are both significantly larger than the average grain size of around 20 nm in the as-milled tungsten samples.

4.2. Short annealing

In order to determine the effects of alloying on grain structure evolution, the ball milled tungsten samples are annealed at 900-1100°C for 4.5 hours to probe for any change in structure at these temperatures. Analysis of the post-annealing structures by X-ray diffraction and TEM imaging shows evidence of grain size retention in the W-15 at.% Ti alloy annealed at 1000°C, while the unalloyed tungsten grain structure is significantly coarsened at a lower annealing temperature of 950°C. Figure 4.32 shows a comparison between the grain sizes obtained from XRD patterns and TEM images, with the TEM grain sizes plotted in blue. The extracted lattice parameters in Figure 4.33 are observed to vary with the solute content, with a lower lattice parameter as the solute composition increases. At a certain solute concentration, the lattice parameter displays a positive linear relationship with the annealing temperature, which could result from a higher degree of relaxation at the higher annealing temperature.

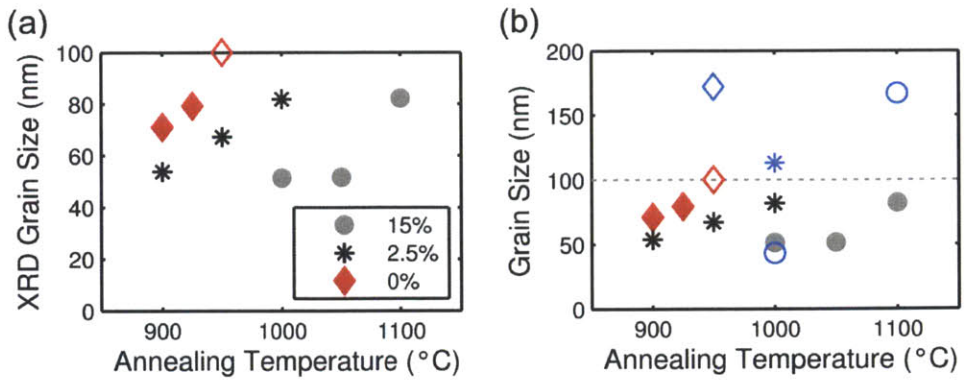

Figure 4.32: (a) XRD grain size of tungsten alloys after annealing. The grain size that falls above the reliable limit of XRD grain size analysis is plotted with an open marker at 100 nm. (b) Comparison between XRD and TEM grain sizes with those obtained from TEM images in blue.

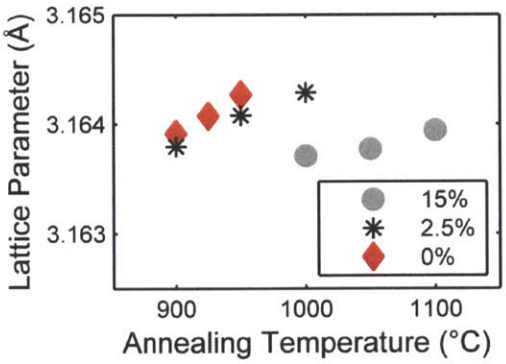

Figure 4.33: Lattice parameter of tungsten after annealing.

The grain size histograms in Figure 4.34 are obtained from TEM images and they confirm the difference in thermal stability in these alloys with respect to solute composition and annealing temperature. The TEM images show the grain size on the order of several hundreds of nanometers in the unalloyed tungsten annealed at 950°C and a uniform fine-grained structure in the W-15 at.% Ti sample. After annealing, the average grain size of the W-15 at.% Ti sample increases only marginally and the distribution becomes slightly broader. The larger grains are a small fraction of the entire grain population, and therefore result in only a minor change in average grain size from those runaway grains. A second phase emerges in the W-2.5 at.% Ti sample annealed at 1000°C and the W-15 at.% Ti sample annealed at 1100°C.

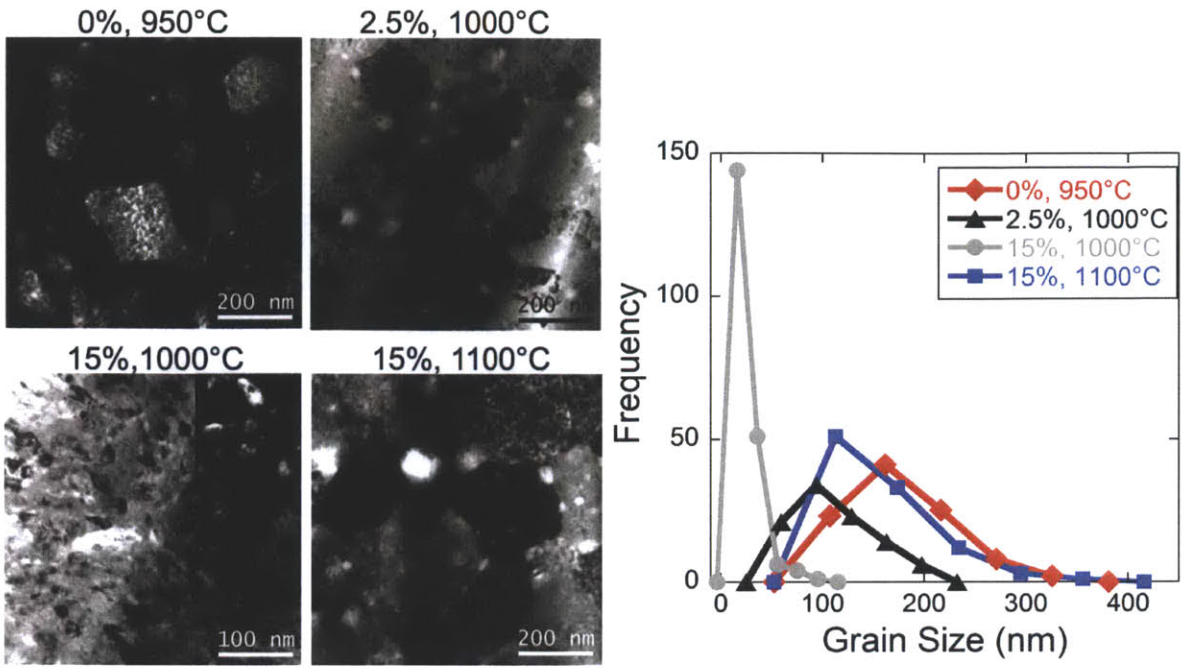

Figure 4.34: TEM images and grain size distributions of the tungsten samples after a 4.5-hour isothermal anneal at 950-1100°C.

These initial results show the grain size dependence on the annealing temperature and the solute content. Specifically, increasing the solute content appears to extend the temperature range in which the fine grain structure can be maintained. With a possibility of retaining the grain structures at 1000°C with 15 at.% solute content, these tungsten alloys are tested further by annealing for a longer duration of time to probe for any stability limit.

4.3. Extended annealing

Ball milled tungsten with 0, 5, 10, and 20 at.% titanium content were annealed at 1100°C for one day and at 1000°C and 1100°C for one week in an argon atmosphere then quenched to room temperature. The pre- and post- annealing structures were analyzed using X-ray diffraction for phase identification, grain size, microstrain, and lattice parameter. The procedures for specimen preparation and TEM imaging are similar to those outlined in Chapter 3. For relatively large grained structures, FIB imaging was performed using an FEI Helios NanoLab focused ion beam.

The lattice parameters of tungsten in the annealed samples are plotted in Figure 4.35 along with those obtained from the pre-annealing structures. The decrease in tungsten lattice

parameter with titanium composition after annealing could result from redistribution of titanium atoms from the titanium-tungsten solid solution in various possible scenarios, such as segregation of titanium into grain boundaries of tungsten, titanium-rich precipitates, or new phase formation. Relaxation of the deformed lattice also contributes to the change in lattice parameter of tungsten, although chemical effects may be more significant, as seen in the minor change in lattice parameters of unalloyed tungsten compared to those of tungsten alloys. In the as-milled samples, the lattice parameter slightly increases with the addition of titanium, and the variation results from the larger metallic radius of titanium compared to tungsten. However, the increase is very minor and is lower than the weighted average of the two metallic radii.

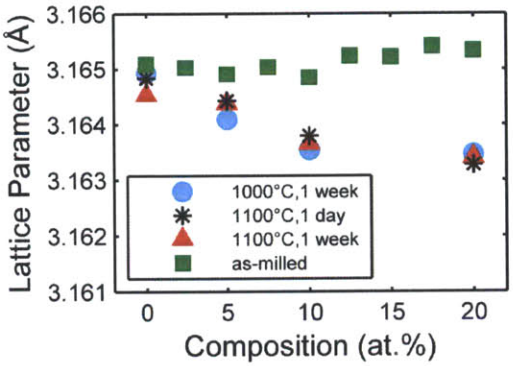

Figure 4.35: Lattice parameters of tungsten in the pre- and post- annealing structures.

Figure 4.36(a) shows the post-annealing XRD grain sizes and improvement in grain stability with increasing solute concentration. We note that grain sizes after annealing at 1000°C for one week and at 1100°C for one day are comparable and this is consistent with the similar diffusion distances listed in Table 4.2 under both conditions. The average grain sizes obtained from TEM images in Figure 4.36(b) confirm the solute-enhanced thermal stability, but reveals severe grain coarsening at dilute concentrations.

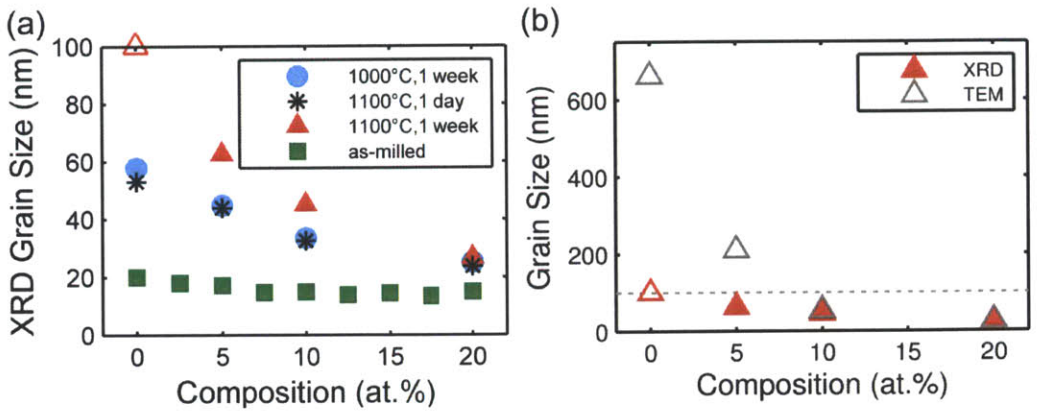

Figure 4.36: (a) As-milled and post-annealing XRD grain sizes under different annealing conditions. (b) Comparison between XRD and TEM grain sizes obtained from tungsten samples after a one-week anneal at 1100°C.

After a one-week anneal at 1100°C, the FIB cross section image of unalloyed tungsten in Figure 4.37 confirms grain coarsening in the unalloyed nanocrystalline tungsten powder to several hundreds of nanometers in average grain size. The grains become faceted and straight grain boundaries are clearly visible. The W alloy powders with 5, 10 and 20 at.% Ti content are prepared by the lift-out technique and studied under a TEM. The W-5 at.% Ti sample shows second phase particles throughout the structure. The tungsten grains grow noticeably larger although the grain boundaries are not straightened out like those in the unalloyed tungsten. The W-10 at.% Ti sample exhibits grain growth and some second phase formation but not as severe as in the 5 at.% sample. On the contrary, the W-20 at.% Ti sample displays grain size retention below 100 nm with no evident second phase. The grain sizes obtained from TEM and XRD analysis are listed in Table 4.3.

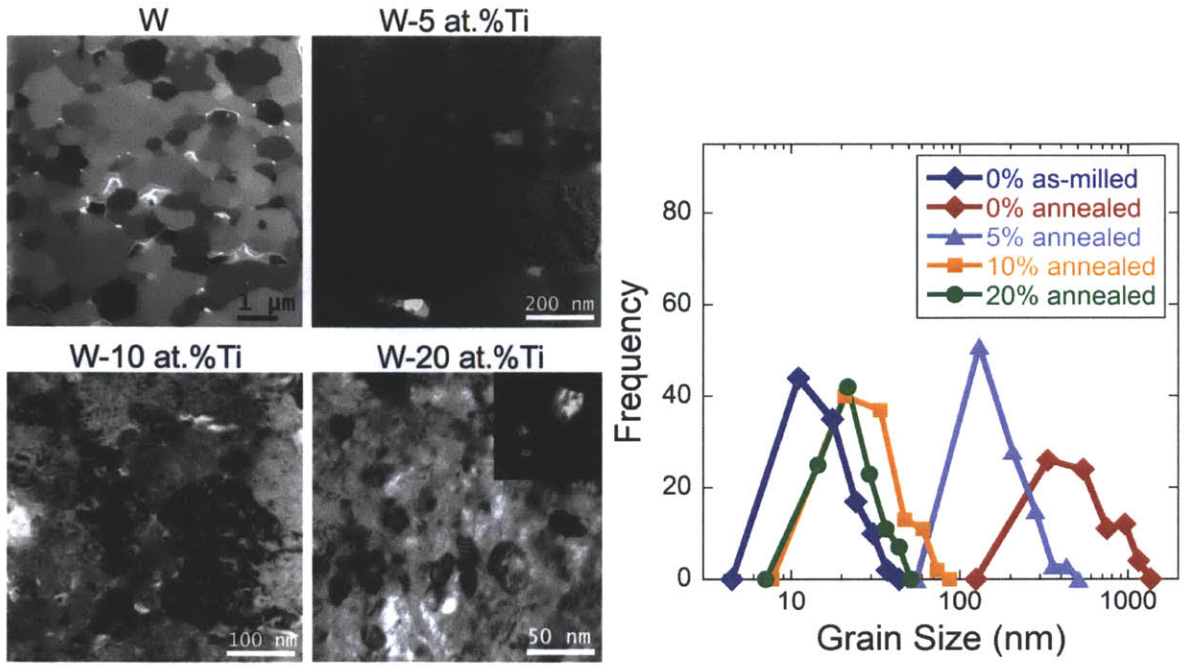

Figure 4.37: FIB image of unalloyed W and TEM bright-field images with a dark-field TEM inset of W-Ti alloys after a one-week anneal at 1100°C. Grain size distribution histograms of the post-annealing structures are also provided.

Table 4.3: Grain sizes obtained from TEM observation and estimated from XRD patterns.

Ti Composition (at.%)	Condition	TEM arithmetic average size (nm)	TEM volume averaged size (nm)	XRD Rietveld size (nm)	XRD Langford size (nm)
20	As-milled	22	32	20	30
20	Annealed	24	33	35	43
10	Annealed	35	70	59	79
5	Annealed	153	280	83	> 100
0	As-milled	17	26	27	43
0	Annealed	604	883	> 100	> 100

The extent or breakdown of nanostructure stability with respect to composition and temperature may result from a change in structural or chemical arrangements that could be

overlooked in bulk thermodynamics. Without any consideration of grain boundaries, a bulk tungsten-titanium mixture is expected to exist in BCC solid solution with a possibility of hexagonal close packed (HCP) titanium emerging at temperatures below 490°C. In nanocrystalline materials, the large volume of interfaces may induce behaviors or structures that are unexpected in coarse grained materials. For instance, as a fast diffusing specie, titanium atoms can redistribute via tungsten grain boundaries or aggregate into a second phase, such as those in the 5 at.% Ti case. The solute redistribution can thus trigger a change in grain boundary segregation state and therefore tungsten grain structure. Here the appearance of the second phase seems to be associated with the breakdown of grain structure stability in the samples with relatively dilute concentrations. At the higher Ti composition of 20 at.%, the grain structure remains uniformly on the nanoscale with no observable second phase.

4.4. Conclusions

Grain stability of nanocrystalline tungsten is investigated by several isothermal annealing experiments. The post-annealing structures are characterized by X-ray diffraction and electron microscopy and the following conclusions may be drawn:

- The post-annealing grain sizes are similar in the samples subjected to annealing conditions with equivalent diffusion distance, but significantly different annealing time and temperature (i.e. 1000°C for one week and 1100°C for one day).
- Grain stability can be intervened by a competition from a second phase and therefore stability against both grain growth and second phase formation must be considered.
- Titanium is potentially a good candidate for grain stabilization of tungsten, and the grain stabilizing effects is dependent on titanium concentration. A 20 at.% addition of titanium is observed to help inhibit grain coarsening in nanocrystalline tungsten at the expected sintering temperature of 1100°C for the duration of one week.
- Grain structure stability is influenced by diffusion length, solute concentration and a change in equilibrium state. The alloying condition should be adjusted according to the thermal requirement, i.e. the time and temperature, as well as any possible phase transformation at the required temperature.

Chapter 5: Segregation behaviors in W-Ti nanocrystalline alloys

5.1. Characterization of grain boundary segregation

5.1.1. Characterization methods

Among the direct and indirect characterization methods of chemical segregation, microscopy techniques are a particularly useful tool for assessing the extent of solute segregation at grain boundaries in both qualitative and quantitative manners. For chemical segregation in the vicinity of a grain boundary, Taheri et al. suggested three characterization methods as follows [70]:

1. Estimation of segregation level from grain boundary mobility
2. TEM based methods such as Z (atomic number) contrast imaging by scanning transmission electron microscopy (STEM) and/or electron energy loss spectroscopy (EELS)
3. Atom probe tomography (APT) method -- local electrode atom probe (LEAP) tomography also offers site-specific analysis by using a movable electrode to field-evaporate atoms locally.

TEM based methods such as STEM and EELS provide through-thickness information of the specimen, or more specifically, atomic column imaging. Instead of a parallel electron beam, STEM technique is based on using a convergent beam of electrons, or electron probe, to obtain point-by-point electron scattering data by scanning over the surface of the specimen. The scanning electron probe can simultaneously generate several types of signals, both images and spectrometry depending on the physics of interactions, including annular dark-field imaging (ADF), high-angle annular dark-field imaging (HAADF), energy dispersive X-ray spectroscopy (EDS), and EELS. STEM images are produced by the scattered electrons collected by the annular detector below the specimen. The amount of scattering depends on the Rutherford scattering cross-section which varies with atomic number by Z^2. As a result, the intensity at each point of a STEM image indicates the average atomic number over the vertical atomic column illuminated by the electron probe [71]. One advantage of STEM imaging is the robustness of the data; there is no contrast reversal with local specimen thickness or change of focus. Therefore,

qualitative observation in STEM is considered reliable; the position of an atomic column can be accurately identified by bright contrast. Hence, STEM images can provide direct observation of atomic arrangement and consistently identify the difference in chemical species. In particular, ADF and HAADF imaging works well with high atomic number elements but can be insensitive to certain light elements.

STEM analysis of the chemical arrangement at or near grain boundaries is most of the time qualitative (by contrast comparison) or by direct observation at the atomic resolution. Quantitative STEM-based characterization is possible with spectrometry based on signals generated by electron scattering, which are generally EDS and EELS techniques. EDS analysis is common and particularly suited for heavier elements. For light elements, EELS can provide complementary data, specifically for elements from carbon to zinc, with a requirement of very thin specimens. For the analysis of heavy metals such as tungsten based alloys, EDS is the STEM-based spectroscopy method of choice.

5.1.2. Resolution limit

Kimoto et al. made an interesting statement regarding the practicality of imaging techniques as follows [72]:

> "Although atomically resolved measurements have long been possible, an important goal in *microstructure characterization* is to achieve *element-selective* imaging at atomic resolution. A combination of scanning transmission electron microscopy (STEM) and electron energy-loss spectroscopy (EELS) is a promising technique for *atomic-column* analysis. However, two-dimensional analysis has not yet been performed owing to several difficulties, such as delocalization in inelastic scattering or instrumentation instabilities."

Requirements for obtaining the atomic-column resolution in crystalline materials using STEM-based techniques include a small intense probe and localization of electron probe propagation. Instead of propagating along a certain atomic column, in thick specimens the electron probe can experience dechannelling by having the intensity transferred to adjacent atomic columns and this in turn worsens the resolution [72].

In thick specimens, beam spreading from the single-scattering model determines the spatial resolution by [73]:

$$b = 6.25 \cdot 10^5 \cdot \frac{Z}{E_0} \cdot \left(\frac{\rho}{A}\right)^{1/2} \cdot t^{3/2} \qquad (5.1)$$

where b is the beam spread in cm, Z is the atomic number, E_0 is the beam energy in eV, ρ is the density in g/cm^3, A is the atomic weight, and t is the foil thickness in cm. For tungsten based materials, the high atomic number and density may lead to significant beam spreading and an inherent resolution limit in STEM observation. Therefore, a comparison to other characterization techniques or use of complementary data may be particularly useful in determining the reliability of STEM-based characterizations of heavy metal structures.

5.2. STEM-based grain boundary studies

Characterization of grain boundary structures near or at atomic resolution reported by far has been carried out mostly on individual well-defined grain boundaries with high symmetry (coincident site lattice, or CSL grain boundaries) or ideal grain boundaries in bicrystals, made possible by site-specific sample preparation (such as focused ion beam methods) on pre-determined high-symmetry grain boundaries or those that are artificially made [70, 74-76]. Thorough characterization of grain boundary networks or a relatively large volume of material with small grain sizes in the nanocrystalline or near-amorphous regime is still lacking. And with small grain sizes and a large volume fraction of grain boundaries, characterization of all grain boundaries may not be carried out in the "edge-on" direction, making the quantitative analysis in STEM more difficult due to averaging of signals over the whole atomic column under the electron probe. Beside the TEM based methods, three-dimensional tomography techniques may become a critical tool when grain boundaries are entangled into a network and atomic column imaging may be irrelevant or extremely difficult.

STEM-based grain boundary characterization techniques can be classified into two general approaches, namely by direct observation and quantitative spectrometry, as discussed in the following sections.

5.2.1. Direct observation

Atomic resolution images of solute segregation at interfaces have been reported via direct observation of atomic column structures and chemically induced contrast. Z-contrast imaging of individual grain boundaries in Figure 5.38 reveals special atomic arrangement in the grain boundaries compared to the bulk [75-77]. Particularly in CSL boundaries, atoms usually assemble into repeating "structural units" in the vicinity of grain boundaries. Identification of solute segregation is often qualitative, mostly by identifying a peak in contrast and sometimes comparing to image simulations.

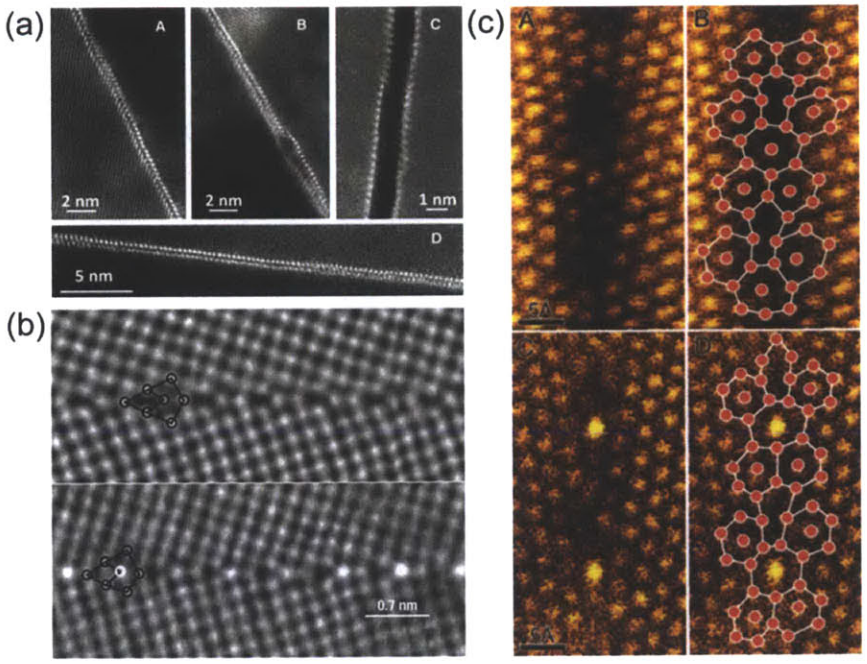

Figure 5.38: (a) STEM HAADF images of a Ni polycrystal showing different contrast from a bilayer interfacial phase of adsorbed Bi along the grain boundaries [77]. (b) Z-contrast images of symmetric 36.8° <001> tilt boundaries in pure and Bi-doped Cu. Repeating structural units and segregation of Bi atoms are observed along the grain boundaries [75]. (c) Z-contrast images of Σ31 [0001] tilt grain boundaries in undoped and Y-doped alumina. Grain boundary segregation of Y is evident from the contrast difference. The atomic column arrangement of structural units is highlighted by the overlays [76].

A STEM-based study of grain boundary segregation in polycrystalline metals was reported by Taheri et al. by direct observation and qualitative identification of solute segregation [70]. The STEM image in Figure 5.39(a) shows a variation in atomic contrast at different types of special grain boundaries, which results from selective grain boundary segregation of the solutes. The variation in brightness intensity over a line drawn across different types of grain

boundaries in the STEM image represents the degree of solute segregation, however only in a qualitative manner.

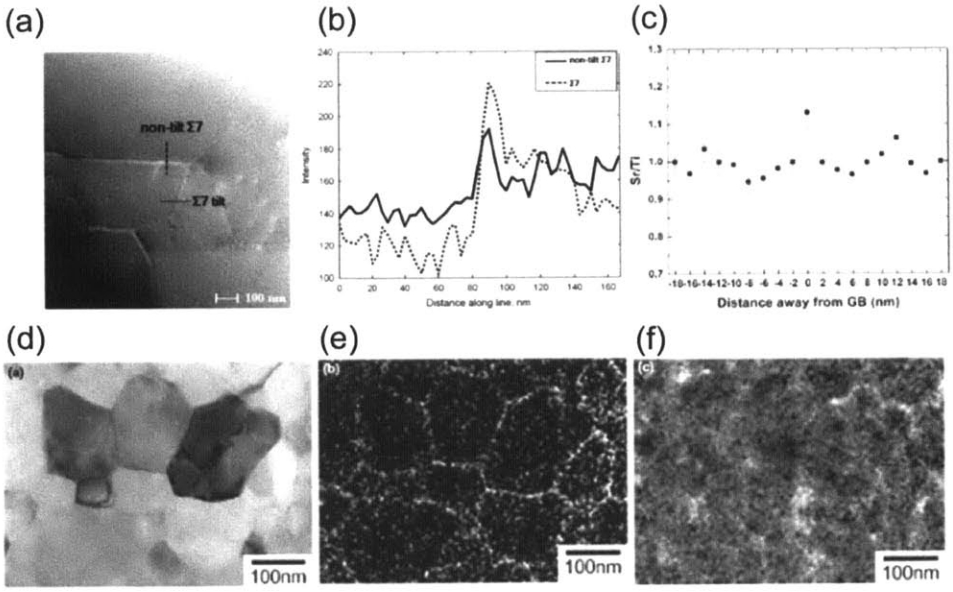

Figure 5.39: Semi-quantitative and quantitative measurements of grain boundary segregation. (a) A STEM image showing higher brightness at the non-tilt Σ7 grain boundary compared to the mobile Σ7 tilt leading edge of a growing grain. (b) Brightness intensity across the Σ7 tilt and non-tilt Σ7 grain boundaries [70]. (c) The Sr/Ti ratio obtained from STEM-EDS chemical composition analyses near the grain boundary vicinity showing Sr enrichment at the grain boundary [78]. (d) STEM image and EDS chemical maps for (e) Y and (f) Al in sintered nanocrystalline tetragonal zirconia [79].

5.2.2. Quantitative methods

Several attempts at the quantitative analysis of grain boundary segregation in STEM using EDS spectrometry have been reported, with many relying on the Cliff-Lorimer equation to obtain the composition profile from EDS intensities.

Cliff-Lorimer method

The weight ratio between two atomic species in a thin specimen can be approximated using the Cliff-Lorimer equation:

$$\frac{C_A}{C_B} = k_{AB}\frac{I_A}{I_B} \qquad (5.2)$$

where C denotes the weight fraction of A and B atomic species, I is the EDS peak intensity above background, and k_{AB} is the Cliff-Lorimer factor for elements A and B, which is determined experimentally using multiple thin-film standards with known composition [80, 81].

Shih et al. performed discrete STEM-EDS measurements using several spot scans across grain boundary regions of $SrTiO_3$ and used the Cliff-Lorimer equation to quantify the ratio between Sr and Ti enrichment at the grain boundaries, as shown in Figure 5.39(b). There are some known errors associated with such method. Specifically, X-ray absorption by the specimen can alter the X-ray intensities even in thin specimens, and the variation of specimen thickness can also affect the amount X-ray generated from each region of the specimen.

Zeta-factor method

Watanabe et al. proposed the zeta-factor method to address the issues of X-ray absorption and specimen thickness variation in the Cliff-Lorimer method [81, 82]. In their approach, the mass-thickness can be related to X-ray intensity by $= \zeta_A \frac{I_A}{C_A D_e}$, where ρ is the specimen density, t is the specimen thickness, ζ_A is the proportional factor, I_A is the measured X-ray intensity above background, C_A is the composition, and D_e is the electron dose. For a binary system, the mass-thickness varies with the intensity from each element as $\rho t = \frac{\zeta_A I_A + \zeta_B I_B}{D_e}$, and therefore the weight fraction can be derived as $C_A = \frac{\zeta_A I_A}{\zeta_A I_A + \zeta_B I_B}$. The ζ factor can be experimentally determined using standards for each required element using the relationship, $\zeta = \frac{A}{C N_0 Q \omega a i}$, where A is the atomic weight, N_0 is Avogadro's number, Q is ionization cross-section, ω is the fluorescence yield, a is the relative transition probability, and i is the beam current. As a result, the ζ factor is independent of the specimen thickness and therefore local thickness variation, which the Cliff-Lorimer method may suffer from [83].

The composition ratio between two elements derived from the zeta-factor method resembles the Cliff-Lorimer equation, as in $\frac{C_A}{C_B} = \frac{\zeta_A I_A}{\zeta_B I_B} = k_{AB} \frac{I_A}{I_B}$. However, here the ζ factor can be independently measured for each element, and therefore the calibration can be done using a single-element standard. It should be noted that the Cliff-Lorimer method remains accurate given that the appropriate k factor is used. Even though the zeta-factor method may offer some improvements over the Cliff-Lorimer method, it is yet to be made available in standard

commercial EDS software. On the other hand, the Cliff-Lorimer method is more accessible and remains reliable with proper calibration.

5.2.3. Other characterization methods

A combination of TEM-based methods such as TEM, STEM, EDS, and EELS with other characterization tools and modeling has been shown to provide intensive complementary data [84]. In particular, atom probe tomography (APT) has aided the visualization of microstructural features in three dimensions as an extension to two-dimensional TEM-based methods. Although the chemical data with respect to the spatial position in three dimensions is the advantage of APT, direct detection of grain boundaries is generally difficult or unavailable in the instrument, and may not be straightforward in all material structures. Evidence of grain boundaries can be indirect, such as an orientation shift shown in stereographic projection in field ion microscopy, or a sharp increase in evaporation rate, or it could be derived from statistical analysis [70, 85, 86]. These evidences may be less pronounced in ultrafine-grained structures where an excessive amount of grain boundaries exist throughout the volume of the specimen. Furthermore, the advance of the evaporation front through the specimen may obscure the intensity of such signals, or the grain boundary related events may be so frequent that the data appears too scattered.

5.3. Segregation behaviors in W-Ti alloys

The bright- and dark- field TEM images of the annealed W-Ti alloys in Chapter 4 provide grain structure information and degree of thermal stability of these alloys. However, further analysis of the chemical distribution may offer an insight into the segregation behavior and possibly the mechanism behind the enhanced stability. In the following section, the chemical distributions will be investigated using the STEM-EDS method and the Cliff-Lorimer equation will be used to quantify the extent of segregation. Comparison to a three-dimensional characterization technique will be made in order to assess the validity of the STEM-EDS method.

5.3.1. STEM-EDS analysis

A JEOL 2010F TEM with STEM and EDS capability was used for atomic contrast imaging and elemental analysis of the annealed samples. Elemental maps and compositional line

scans can be obtained from these grain structures to study the distribution of titanium in tungsten after annealing. The two alloys that exhibit enhanced grain stability at 1100°C, i.e. W-10 at.% Ti and W-20 at.% Ti, were characterized.

A bright-field STEM image, showing titanium-rich areas in brighter contrast and tungsten-rich areas in darker contrast, and EDS elemental maps of the annealed W-10 at.% Ti alloy display irregular shaped titanium-rich regions in the tungsten polycrystalline structure as shown in Figure 5.40. The titanium composition profile from EDS shows the titanium composition ranging between 75 and 96 at.% in the relatively large titanium-rich precipitates that appear to enclose the tungsten grains. There is also segregation of titanium at the boundaries of tungsten grains at a lower concentration range of around 5-20 at.%.

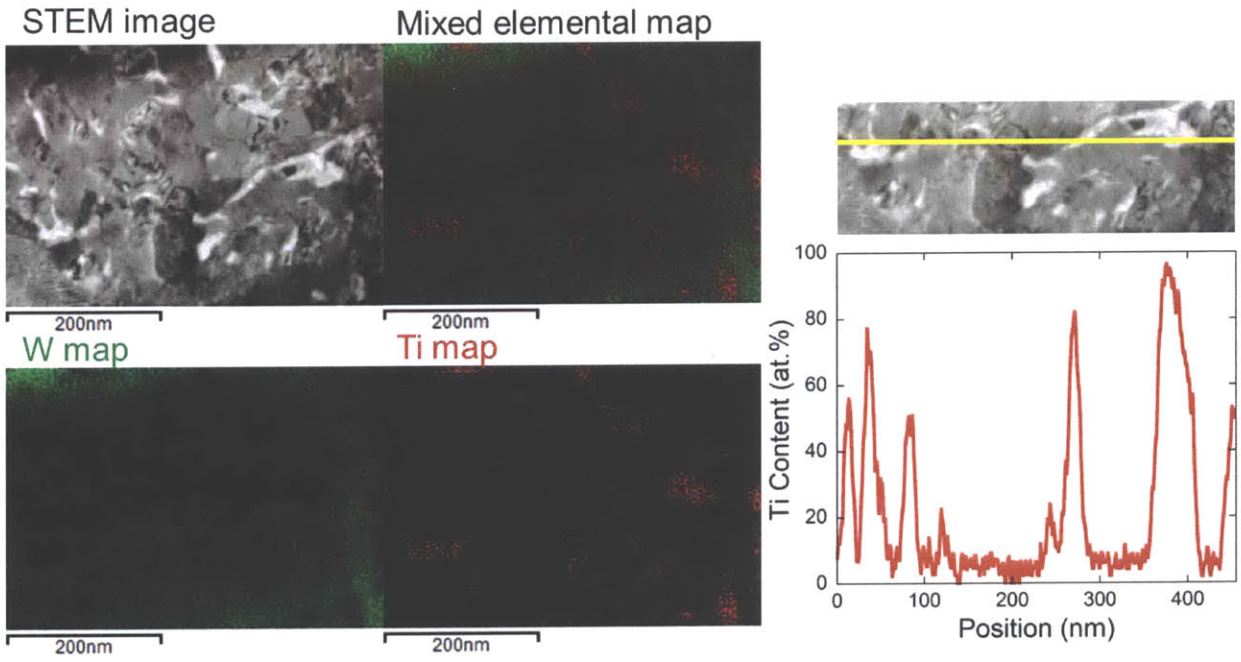

Figure 5.40: STEM image, elemental maps, and Ti compositional line profile obtained from the W-10 at.% Ti alloy after a one-week anneal at 1100°C.

Figure 5.41 show an inhomogeneous distribution of Ti in the annealed W-20 at.% Ti alloy around the visible tungsten grains identified by the darker contrast in the bright-field STEM image. The EDS compositional profile shows the titanium composition varying between 5 and 53 at.%, which is close to the 0-48 at.% solubility limit of Ti in W at 1100°C. The compositional line scan also suggests that titanium is depleted from the tungsten-rich grain centers and rises to approximately 50-60 at.% close to the tungsten-rich grain exterior. Although STEM images can

reveal the contrast between heavy and light elements, two adjacent tungsten grains with different crystal orientations may not be as clearly resolved as by the diffraction contrast in the TEM images.

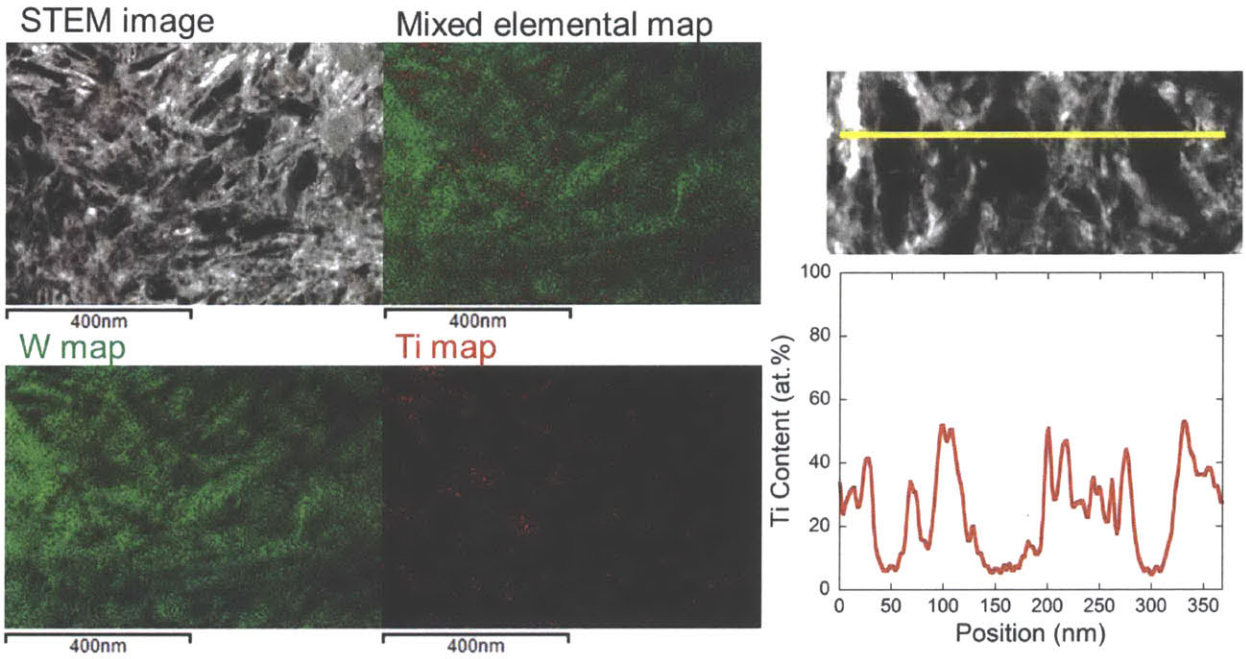

Figure 5.41: STEM image, elemental maps, and Ti compositional line profile from the W-20 at.% Ti alloy after a one-week anneal at 1100°C.

The heterogeneous distribution of Ti in these tungsten alloys is unexpected in conventional bulk W-Ti phase diagrams, which suggest complete miscibility of Ti in W at our annealing temperature of 1100°C and Ti concentrations of 10 and 20 at.%. This unusual separated state could result from incomplete mixing in the as-milled state and therefore we proceed to analyze the as-milled structure of the W-20 at.% Ti alloy. The results in Figure 5.42, however, show fairly uniform distributions of W and Ti atoms with some fluctuation in Ti content around the 20 at.% nominal concentration.

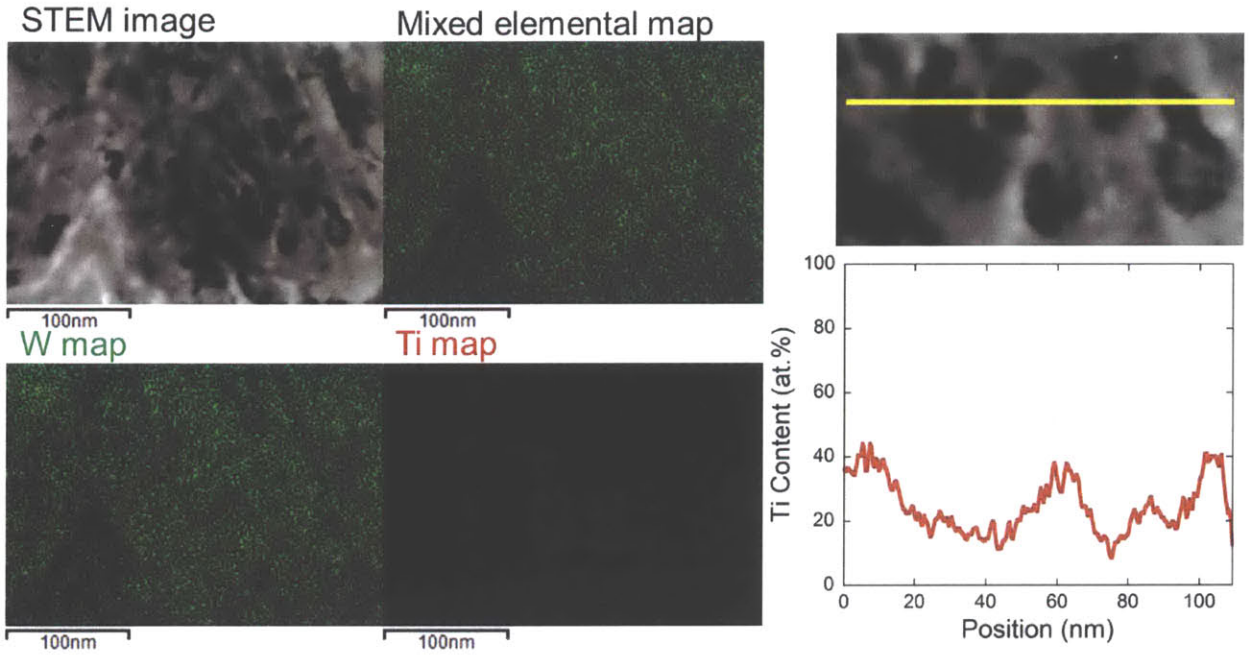

Figure 5.42: STEM image, elemental maps, and Ti compositional line profile obtained from the as-milled W-20 at.% Ti alloy.

5.3.2. Atom probe tomography

The annealed W-20 at.% Ti sample is further analyzed using the atom probe tomography technique to investigate the volume distribution of Ti atoms. The APT specimen was prepared by the FIB lift-out method and the atom probe evaporation procedure was performed using a Cameca local electrode atom probe (LEAP-4000X HR) in the laser pulse mode with the initial pulse frequency of 50 kHz at the pressure of 4.9×10^{-11} torr at 55 K. Before going into further detail, the APT results are first presented in a top-down view of the overall volume distributions, as shown in Figure 5.43(a), in order to compare with the through-thickness STEM measurements.

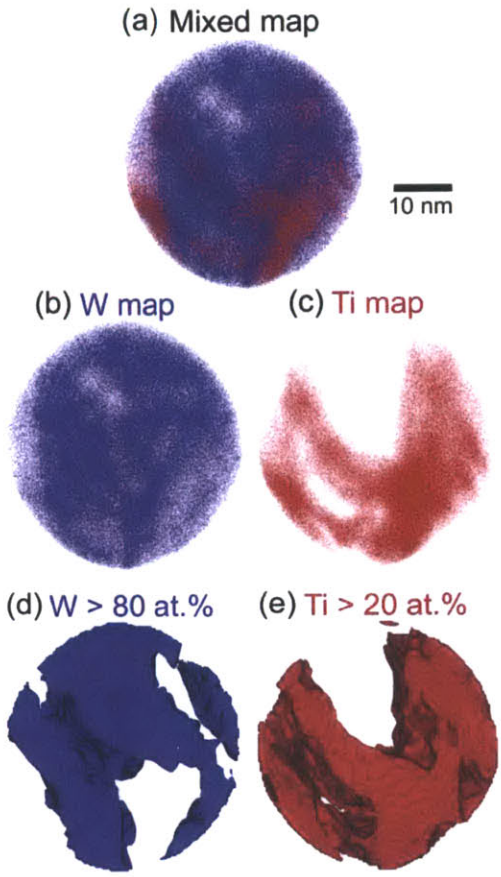

Figure 5.43: Through-thickness representation of (a) mixed W and Ti elemental map and separate (b) W and (c) Ti distributions from atom probe tomography analysis of the W-20 at.% Ti alloy after a one-week anneal at 1100°C. Tungsten atoms are uniformly distributed whereas the titanium atoms display a spatial preference with the size of the Ti-depleted region comparable to the tungsten grain size. The compositional isosurfaces of (d) W and (e) Ti distributions show regions with local composition higher than the nominal values.

While the distribution of W atoms appears uniform in Figure 5.43(b), both of Ti-rich and Ti-depleted regions are present in the Ti distribution map in Figure 5.43(c). The overall distributions of both types of atoms presented in the mixed elemental map in Figure 5.43(a) resemble those observed earlier using the STEM-EDS method.

A more quantitative interpretation of the APT results is first presented by the compositional isosurfaces in Figure 5.43(d) and (e). The region enclosed by the red surface in Figure 5.43(e) are enriched above the nominal 20 at.% Ti concentration, and the complementary blue surface bounds the regions in Figure 5.43(d) with the W content higher than 80 at.%. Even though the absolute value of tungsten concentration inside the blue isosurface is above the

nominal 80 at.% value, it is a result of Ti depletion rather than W enrichment, as shown earlier by the fairly uniform distribution of tungsten in Figure 5.43(b). The tungsten and titanium isosurfaces are combined and provided in Figure 5.44(a) and (d) as a reference.

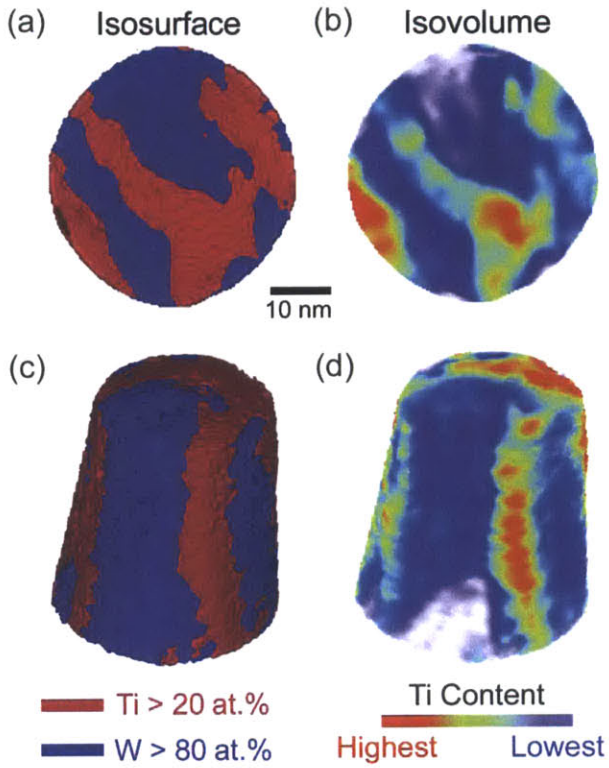

Figure 5.44: Quantitative volume distribution of Ti in the annealed W-20 at.% Ti alloy. (a) Composition isosurfaces of W and Ti show location-specific depletion of Ti below the nominal concentration of 20 at.% in blue and enrichment of Ti above 20 at.% in red. (b) The volume distribution of Ti can be presented by the isovolume with the highest local Ti content in red and the lowest local Ti content in blue. The three-dimensional views of the isosurfaces (d) and volume distribution (e) are provided for the whole specimen volume.

The volume distribution of atoms can also be presented by a combination of multiple isosurfaces into an isovolume shown in Figure 5.44(b) and (e). The colors indicate the relative Ti content at each point in the volume and identify regions with Ti depletion and enrichment, which match the blue and red isosurfaces in Figure 5.44(a) and (d).

A compositional line profile can also be generated from the APT data and the Ti profiles in Figure 5.45(a) and (b) display local peaks in Ti concentration around 20 at.% and 60 at.% with the periodicity comparable to the grain size of tungsten. The quantitative APT results presented in the form of isosurfaces, the isovolume, and the compositional line profiles all illustrate an inhomogeneous distribution of Ti atoms in our post-annealing alloy structure consistent with the

data from STEM-based measurements, with similar segregation profiles measured by both techniques

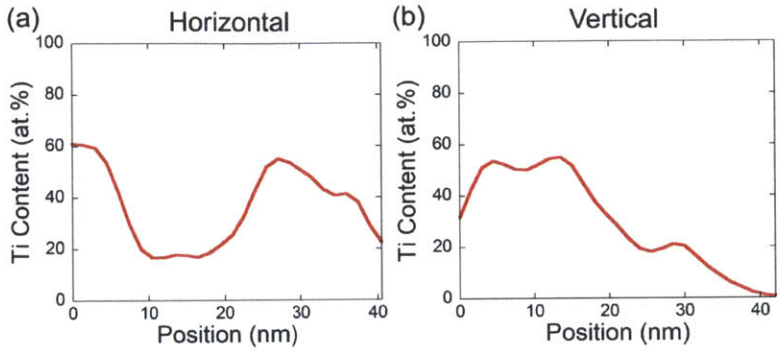

Figure 5.45: Compositional line profiles across the horizontal and vertical axes of the annealed W-20 at.% Ti APT specimen.

The inhomogeneous distribution of titanium atoms observed in the annealed W-20 at.% Ti alloy is unexpected based on a comparison to an equilibrium bulk phase diagram between tungsten and titanium, which anticipates a homogeneous solid solution with a maximum solubility beyond 40 at.% Ti at 1100°C. Nevertheless, our nanocrystalline material is produced by severe plastic deformation, which results in a highly defected, out-of-equilibrium structure in the as-milled state. During the anneal, Ti atoms can redistribute into a low-energy configuration via short-circuit diffusion through interfaces and defects at a faster diffusion rate compared to tungsten atoms. The mismatch between diffusivity and also atomic sizes can result in a combination of W-rich crystalline structures with Ti-rich intergranular regions.

Thus, the discrepancy between our observed structures and a uniform solid solution expected by bulk thermodynamics may result from the influence from grain boundaries, which exist in a large volume fraction in nanostructured materials. The simulated structures of W-Ti alloys in Chapter 3 show a preference for segregation of titanium atoms at grain boundaries over grain interior mixing, which is expected from the larger magnitude of enthalpy of grain boundary segregation, ΔH^{seg}, compared enthalpy of mixing, ΔH^{mix}. In the large grained form, such segregation behavior has a length scale that is much finer than the grain size and a volume fraction that is much smaller than the granular regions. As a result, the overall material structure is dominated by the crystalline constituent and can display the behavior of a crystalline solid solution. However, a grain boundary segregation state may manifest differently if the alloy is allowed to fully equilibrate in a nanocrystalline grain environment and exists in the form of these

complex nanoscale segregation structures. To further explore the effects of grain boundaries, we can use the Monte Carlo alloy simulation to determine the equilibrium structure of W-Ti alloys when grain boundaries are explicitly included as equilibrium features and when the material parameters of W and Ti are applied.

5.3.3. Comparison to simulated structures

The structures of W-Ti alloys at 1100°C are simulated using the Monte Carlo method with the same procedure discussed in Chapter 2 and the input material parameters of W and Ti. Here, the values of bulk like-bonds, $E_c^{WW} = E_c^{TiTi} = 486$ kJ/mol, and grain boundary energy penalties, $\frac{\Omega^W \gamma_0^W}{zt} = 2.64$ kJ/mol and $\frac{\Omega^{Ti} \gamma_0^{Ti}}{zt} = 2.02$ kJ/mol are applied. Before considering the influence of grain boundaries, it may be intuitive to consider the equilibrated bulk structures in order to compare our results with bulk phase diagrams.

When grain boundaries are not allowed, our Monte Carlo simulation produces the expected single-phase solid solution at 1100°C, as shown in Figure 5.46, without any distinct feature such as phase separation or ordering. Further investigation can be made by imitating the experimental compositional line scans. The numbers of W and Ti atoms on the horizontal edges (two rows at the bottom and one row at the top of the image, which are interconnected by the periodic boundary conditions) of the simulated structures are extracted and the through-thickness compositional line profile can be calculated, as shown in Figure 5.46. The Ti profiles show some fluctuation around the nominal 10 and 20 at.% concentrations, however there is no significant local peak. Thus, the expected homogeneous solid solution bulk structures can be appropriately captured by our simulation.

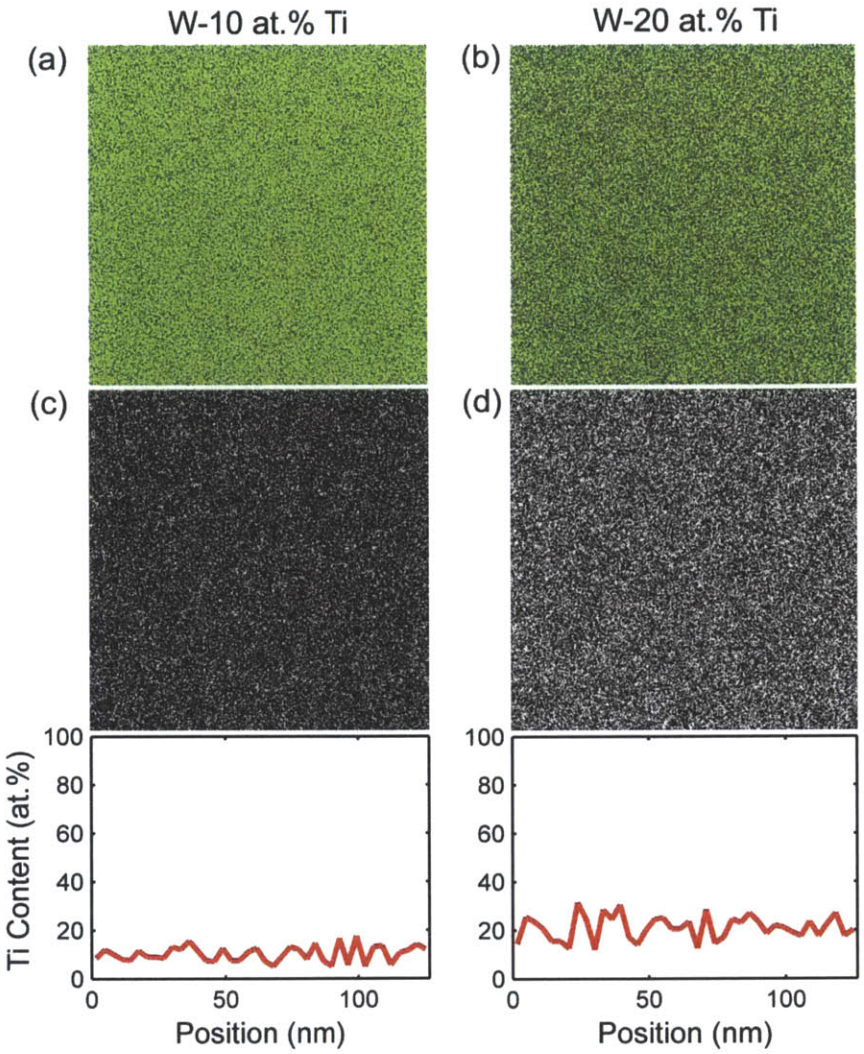

Figure 5.46: Equilibrated bulk structures of (a) W-10 at.% Ti and (b) W-20 at.% Ti alloys at 1100°C calculated using the Monte Carlo alloy simulation. The structures are homogeneous single crystalline solid solutions. The through-thickness compositional line scans across the bottom rows of atoms of the simulated structure also confirm a uniform distribution of titanium atoms around the nominal (c) 10 at.% and (d) 20 at.% Ti composition. Simulations are performed on a 400 x 400 x 6 BCC lattice with $\Delta H^{\text{mix}} = 20$ kJ/mol.

When the single crystalline requirement is no longer imposed, the fully equilibrated structures shown in Figure 5.47 are polycrystalline with complex solute segregation structures. Multiple nanoscale grains can coexist in our equilibrium structures and they are connected by regions of solute segregation in the grain boundary vicinity.

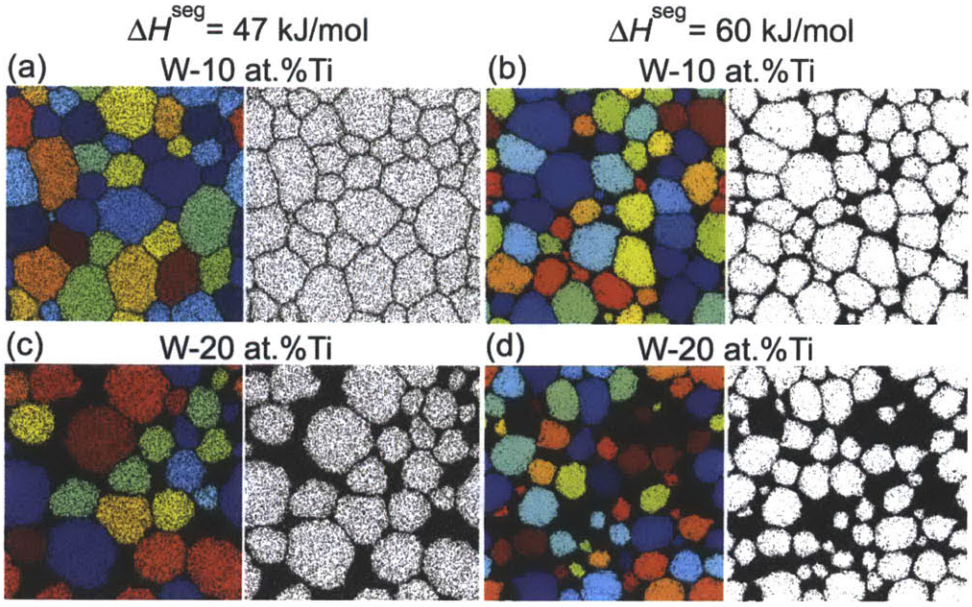

Figure 5.47: Simulated equilibrium structures of W-Ti alloys at 1100°C.The W-10 at.% Ti alloy structures with (a) ΔH^{seg} = 47 kJ/mol and (b) ΔH^{seg} = 60 kJ/mol are solid solutions with titanium grain boundary segregation states. Both of the equilibrated W-20 at.% Ti alloy structures with (c) ΔH^{seg} = 47 kJ/mol and (d) ΔH^{seg} = 60 kJ/mol display inhomogeneous distributions of titanium with titanium atoms being preferentially depleted from the tungsten-rich grains. Simulations are performed on a 1000 x 1000 x 6 BCC lattice and ΔH^{mix} = 20 kJ/mol.

With the values of ΔH^{mix} = 20 kJ/mol and ΔH^{seg} = 47 kJ/mol obtained from Ref. [64], both of the W-10 at.% Ti and W-20 at.% Ti structures in Figure 5.47(a) and (c) are solid solutions with solute segregation in the grain boundary vicinity. Solute segregation is clearly visible in the 20 at.% Ti structures where the titanium atoms are depleted from the crystalline tungsten-rich regions, which is in line with our experimental results. By using the best fit value of ΔH^{seg} = 60 kJ/mol, which is within the calculation errors of ΔH^{seg} from Ref. [64], the experimental W-10 at.% Ti structure can also be captured by our simulation while the segregation state in the W-20 at.% Ti structure remains roughly the same. These simulated structures resemble the experimentally observed chemical distributions in the W-10 at.% Ti and W-20 at.% Ti samples from both STEM-EDS and APT characterizations; They are polycrystalline with complex solute segregation structures.

In particular, the W- 20 at.% Ti alloy forms a dilute solid solution in the grain interior with solute enrichment in the grain boundary vicinity. Chemical segregation is clearly visible as the titanium atoms are depleted from the crystalline regions presented in solid colors and form a

surrounding segregation zone, which is consistent with our STEM-EDS and APT results. This structural-dependent chemical isolation results from the preference for grain boundary segregation over grain interior mixing of titanium, or in other words, a higher solubility of Ti in the grain boundary vicinity than the grain interior. Further comparison can be made by imitating the experimental compositional line scans.

The through-thickness compositional line profiles are shown in Figure 5.48. The peaks in the Ti composition profiles overlap with the position of grain boundaries. There appear to be two types of solute enriched regions. For the W-20 at.% Ti alloy, the relatively large Ti-rich areas appear to have Ti segregation zones with a higher solute content around 60 at.% and also thin layer of segregation at grain boundaries with the Ti content around 20 at.%. These local peak magnitudes are comparable to the APT line profiles in Figure 5.45. Formation of Ti segregation zones is balanced by regions with Ti depletion, which appear to be crystalline, or in other words, in the tungsten-rich grain interior.

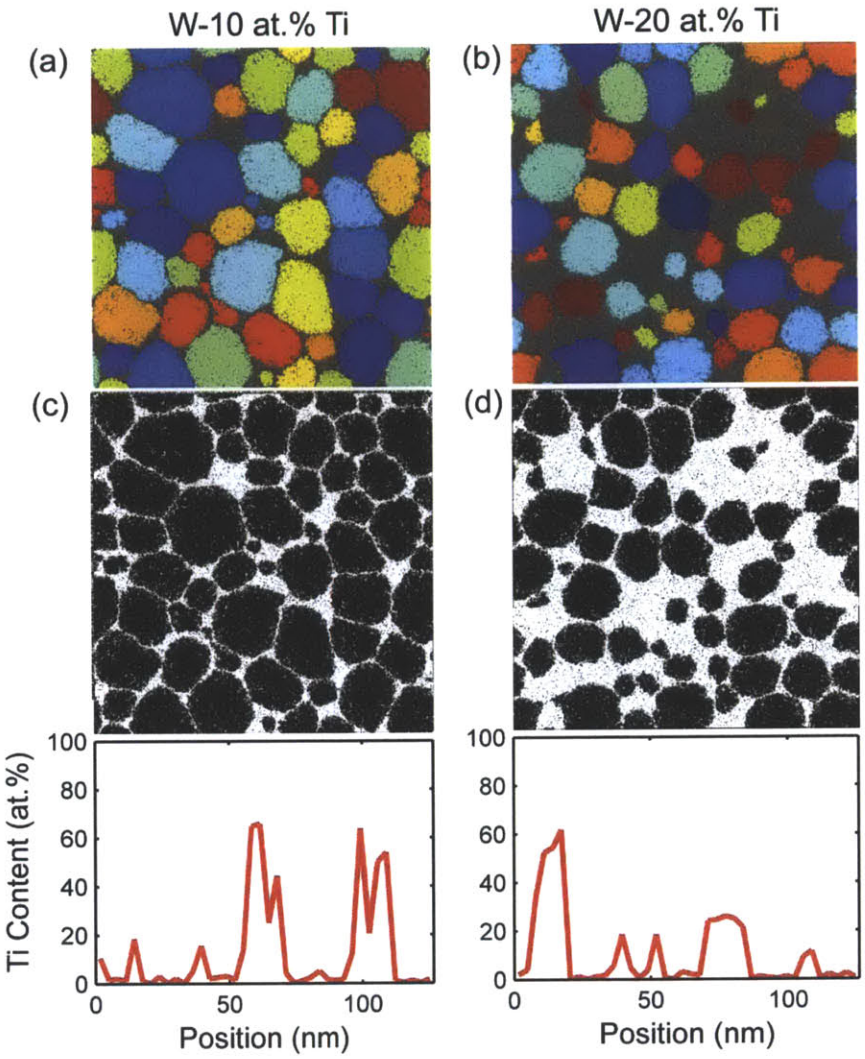

Figure 5.48: Equilibrium grain-atomic structures of W-Ti alloys at 1100°C calculated using the Monte Carlo alloy simulation. The crystalline regions are in solid colors and the Ti atoms are displayed in gray. The fully equilibrated alloy structure displays a complex segregation structure of Ti atoms around W-rich crystalline regions in both (a) W- 10 at.% Ti and (b) W-20 at.% Ti alloys. The chemical distribution, showing titanium atoms in white and tungsten atoms in black, of the alloy structure displays an evident chemical inhomogeneity in the fully equilibrated polycrystalline structures. The through-thickness compositional line scans across the bottom rows of atoms of the simulated structure confirm depletion of titanium atoms from the tungsten-rich crystalline regions and formation of a segregation zone with the Ti content above the nominal Ti composition of 10 at.% in (c) and 20 at.% in (d). Simulations are performed on a 400 x 400 x 6 BCC lattice with $\Delta H^{\mathrm{mix}} = 20$ kJ/mol and $\Delta H^{\mathrm{seg}} = 60$ kJ/mol.

The unusual solute distribution in our annealed W-Ti samples can therefore be captured by our model by incorporating the influence of grain boundaries. The energy relief via alloying enables solute-segregated interface states to persist even after an extended annealing time. The

comparison between the STEM-EDS, APT, and Monte Carlo results are summarized in Figure 5.49. The heterogeneous distribution of Ti is captured by all methods as shown in Figure 5.49(a)-(c) and is supported by the line profiles in Figure 5.49(d)-(f). Ti atoms can form a segregation zone around W-rich grains with the maximum Ti content well above the nominal Ti concentration and is observed to be around 60 at.%. The fluctuation of Ti concentration profile shows an apparent periodicity of Ti depletion similar to the tungsten grain size obtained by TEM.

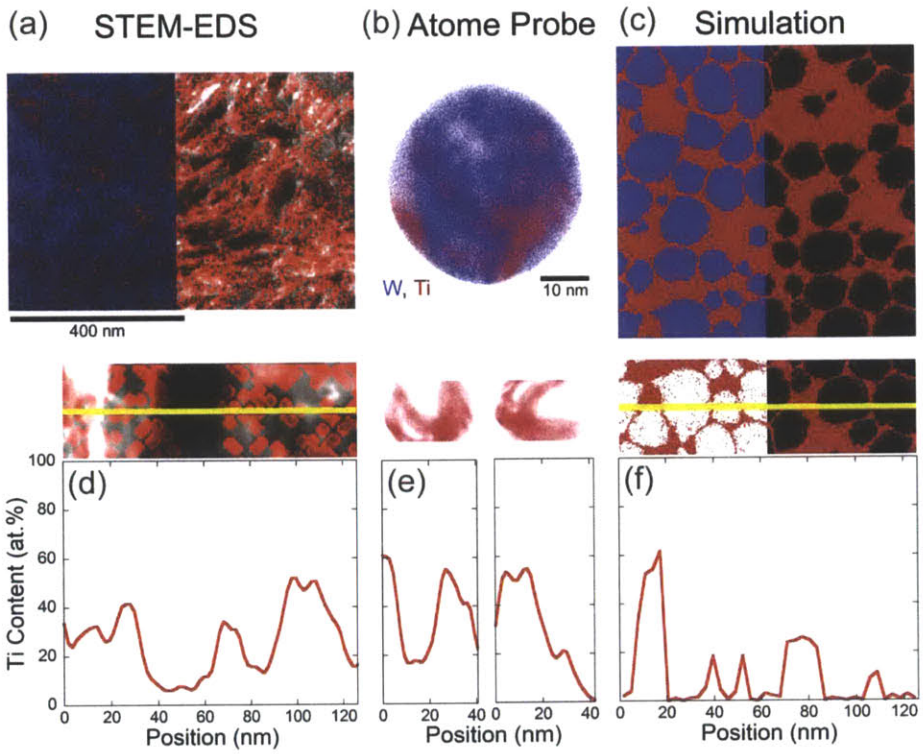

Figure 5.49: Comparison of the W-20 at.% Ti alloy structures after an equilibration at 1100°C from STEM-EDS analysis, atom probe tomography, and Monte Carlo alloy simulation. (a) An EDS elemental map with W atoms in blue and Ti atoms in red is shown on the left, and a grayscale STEM image with an overlaying EDS map of Ti in red is shown on the right. (b) Through-thickness distribution from APT technique with W atoms in blue and Ti atoms in red. (c) A chemical map with Ti atoms in red. The W atoms are shown in red on the left-hand side to compare with the full W-Ti EDS map and the APT results, but shown in black on the right-hand side in order to compare to the STEM contrast. A heterogeneous distribution of Ti is confirmed by all three independent methods. The Ti composition line scans from (d) the STEM-EDS method, (e) atom probe tomography, and (f) Monte Carlo alloy simulation all reveal a similar segregation profile, with the fluctuation up to about 60 at.% and a periodicity comparable to the average tungsten grain size of around 20 nm. Ti atoms are presented in red.

5.4. Conclusions

- The through-thickness information obtained from STEM-based methods provides similar results to the bulk information obtained from atom probe tomography, and therefore the STEM-based results could be considered sufficiently reliable.
- In the W-Ti alloys with enhanced thermal stability, an inhomogeneous distribution of titanium atoms is observed in both STEM-EDS and APT results, but it is unexpected by bulk thermodynamics.
- By using the Monte Carlo simulation, such segregation states are shown to be induced by the inclusion of grain boundaries as an equilibrium feature. In this way, the experimentally observed grain-atomic structure can be reproduced by our simulation.
- Ti atoms preferentially segregate to the intergranular region and form solute segregation structures that enclose W-rich grains. This alloy configuration allows grain boundaries to exist in a lower energy state with Ti enrichment. This in turn allows tungsten atoms to remain in a nanoscale crystalline structure without an energy penalty or driving force for grain coarsening.

Chapter 6: Concluding remarks

By employing both atomistic simulation and experimental testing, the thermodynamics of nanocrystalline alloys is explored. Alloying as the approach for thermodynamics based nanostructure stabilization is demonstrated to be a powerful method for enhancing stability of nanostructured metals and for establishing control of their properties via structural design. The important conclusions drawn from this thesis are summarized below.

In Chapter 2, we show by a thermodynamics based simulation that a nanostructured alloy can be the most energetically favorable thermodynamic state given a suitable alloying condition. The grain boundary energetic requirement for grain stability is clarified and we distinguish the two thermodynamic terms, $\frac{dG}{dA}$ and γ, that are both generally recognized as the grain boundary energy. Beside a zero grain boundary area potential, $\frac{dG}{dA}$, a negative grain boundary formation energy, γ, is also a requirement for achieving grain stability via grain boundary segregation of solute, and its magnitude is identified as a quantitative measure of grain stability. The control of grain size and grain-atomic structure via alloying specie and concentration is demonstrated in detail.

In Chapter 3, the framework for alloying element selection is presented and we identify titanium as a suitable alloying element for powder-route nanocrystalline tungsten. The synthesis method of nanocrystalline tungsten alloys by severe plastic deformation via high-energy ball milling is developed, and the as-processed structure is characterized to be about 20 nm in average grain size. The X-ray diffraction and electron microscopy techniques required for structural characterizations are introduced.

In Chapter 4, thermal stability of nanocrystalline tungsten and nanocrystalline W-Ti alloys is tested by short and extended isothermal annealing in the temperature range of 900-1100°C. Grain stability can be modified via diffusion length (comprising temperature, time, and material characteristics), solute concentration and possible phase change. For the purpose of power-route manufacturing development, the nanoscale grain structure of tungsten can be retained at the expected sintering temperature of 1100°C for one week with a 20 at.% addition of titanium.

In Chapter 5, the chemical distributions of tungsten and titanium in the post-annealing structures are investigated using microscopy, diffraction, and tomography techniques. An inhomogeneous distribution of titanium atoms in the more uniform tungsten host is experimentally observed but unforeseen according to the high solubility of titanium in tungsten from conventional bulk phase diagrams. By using the Monte Carlo simulation to equilibrate the W-Ti structure with an explicit consideration of grain boundaries and alloying effects, the nanoscale heterogeneous distribution of solute is clearly anticipated. The complex interface and chemical configuration induced by grain boundaries and alloying is expected to be the basis of the enhanced grain stability.

The findings in this thesis may provide detailed understandings of thermodynamics in nanostructured metals and its application in establishing the thermodynamics-based stabilization approach for synthesis of stable nanocrystalline alloys. In particular, the production of nanocrystalline tungsten-titanium alloys with enhanced thermal stability may serve a case study for further developments of many other stable nanocrystalline alloys.

Chapter 7: Directions for future work

Through the understandings of thermodynamics in these nanocrystalline alloy systems, many interesting research questions have emerged and the future research efforts may be directed to explore the following topics:

- Alloys with a negative enthalpy of mixing that may exhibit ordering, compound formation, and solute-induced amorphization may be explored using the Monte Carlo simulation method. Furthermore, alloys with negative grain boundary adsorption could be studied for grain boundary anti-segregation behaviors.
- FCC and other types of metals can also be studied using our simulation framework with an adjustment of the base lattice. A specialized grain boundary phase can also be included in the simulation to account for grain boundary thickness and its atomic disordering.
- Beyond binary systems, simulation of multi-component systems is possible with an adjustment in the bond energy scheme.
- The sintering mechanism in nanocrystalline tungsten should be further explored in order to complete the development of powder-route nanocrystalline tungsten compact. The solute that acts as a grain stabilizer may be beneficial or deteriorative to the sintering process.
- The mechanical properties of nanocrystalline tungsten alloys should be explored especially for their deformation behavior. Confirmation of rate sensitivity in nanocrystalline alloy will be important for the applications of these materials.
- Characterization techniques of grain boundary solute segregation should be further developed with a focus on nanoscale grain boundary networks. Investigation of any change in grain boundary characteristics as a result of alloying in nanostructured metals will also be an interesting topic.

Appendix A: Monte Carlo simulation details

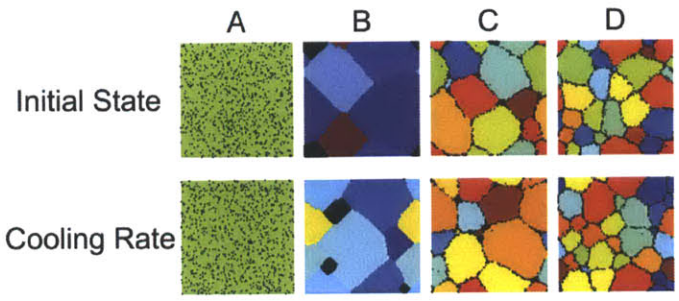

Figure A.1: Equilibrium state convergence with different initial states and cooling rates. The structures with a bicrystal initial state evolve to similar configurations to those with a randomized initial state in Chapter 2. The cooling rate of $\frac{-(T_{\text{step}}-T_{\text{final}})}{100}$ produces similar equilibrium structures to those with a slower cooling rate in Chapter 2. Simulations are performed on a 100 x 100 x 6 BCC lattice with the material parameters of alloys A, B, C, and D from Figure 2.4, $X = 5$ at.%, and $T = 500°C$.

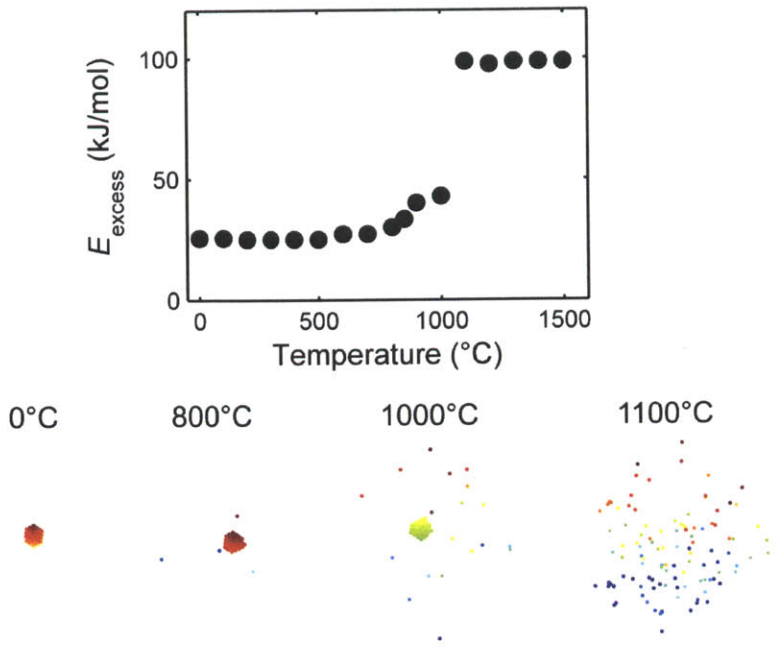

Figure A.2: Effects of temperature and entropically stabilized states. The solute distribution evolves from a precipitated state to a completely miscible solid solution with increasing temperature. The normalized energy excess from chemical mixing, reflected by $E_{\text{excess}} = \frac{E_{\text{system}} - zNE_c^{AA}/2}{N_B}$, increases with the system temperature. An entropically stabilized solid solution is preferred over a precipitated state with lower internal energy at elevated temperatures as a result of the uphill switching events with the temperature dependent probability $P = e^{\frac{-(E_2-E_1)}{kT}}$. Simulations are performed on a 30 x 30 x 60 BCC single crystalline lattice with ΔH^{mix} = 100 kJ/mol and 0.2 at.% solute content.

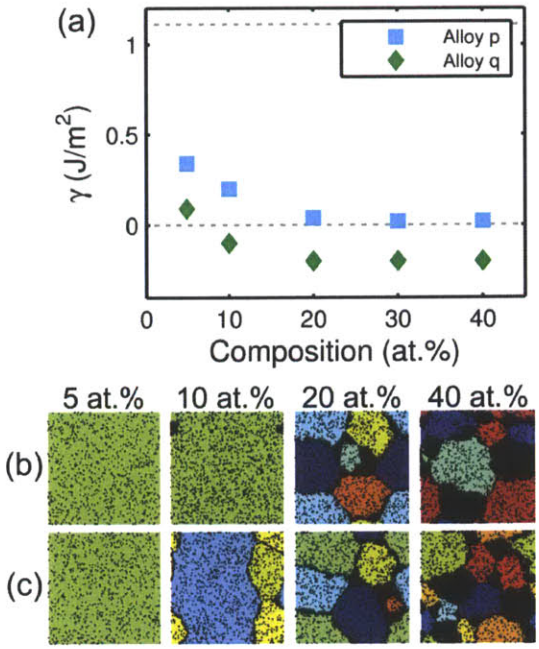

Figure A.3: Change in structure and grain boundary formation energy with solute content in alloys p and q from the duplex region "C". A certain minimum solute content is required for grain stability and for reduction in grain boundary formation energy below zero.

References

1. Detor, A.J. and C.A. Schuh, *Tailoring and patterning the grain size of nanocrystalline alloys.* Acta Materialia, 2007. **55**(1): p. 371-379.
2. Trelewicz, J.R. and C.A. Schuh, *The Hall-Petch breakdown in nanocrystalline metals: A crossover to glass-like deformation*, 2007, Tarrytown, NY: Elsevier Science Inc., 1996-. p. 5948-5958.
3. Trelewicz, J.R. and C.A. Schuh, *The Hall–Petch breakdown at high strain rates: Optimizing nanocrystalline grain size for impact applications*, 2008. p. 171916.
4. Lu, K., L. Lu, and S. Suresh, *Strengthening Materials by Engineering Coherent Internal Boundaries at the Nanoscale.* Science, 2009. **324**(5925): p. 349-352.
5. Lu, L., M.L. Sui, and K. Lu, *Superplastic Extensibility of Nanocrystalline Copper at Room Temperature.* Science, 2000. **287**(5457): p. 1463-1466.
6. Rupert, T.J. and C.A. Schuh, *Sliding wear of nanocrystalline Ni–W: Structural evolution and the apparent breakdown of Archard scaling.* Acta Materialia, 2010. **58**(12): p. 4137-4148.
7. Poudel, B., et al., *High-Thermoelectric Performance of Nanostructured Bismuth Antimony Telluride Bulk Alloys.* Science, 2008. **320**(5876): p. 634-638.
8. Lu, L., et al., *Ultrahigh Strength and High Electrical Conductivity in Copper.* Science, 2004. **304**(5669): p. 422-426.
9. McHenry, M.E., M.A. Willard, and D.E. Laughlin, *Amorphous and nanocrystalline materials for applications as soft magnets.* Progress in Materials Science, 1999. **44**(4): p. 291-433.
10. Wei, Q., et al., *Mechanical behavior and dynamic failure of high-strength ultrafine grained tungsten under uniaxial compression.* Acta Materialia, 2006. **54**(1): p. 77-87.
11. Wei, Q., et al., *Effect of nanocrystalline and ultrafine grain sizes on the strain rate sensitivity and activation volume: fcc versus bcc metals.* Materials Science and Engineering: A, 2004. **381**(1–2): p. 71-79.
12. Jia, D., K.T. Ramesh, and E. Ma, *Effects of nanocrystalline and ultrafine grain sizes on constitutive behavior and shear bands in iron.* Acta Materialia, 2003. **51**(12): p. 3495-3509.
13. Jia, D., K.T. Ramesh, and E. Ma, *Failure mode and dynamic behavior of nanophase iron under compression*, 1999, Johns Hopkins Univ., Baltimore, MD (US).
14. Wei, Q., et al., *Evolution and microstructure of shear bands in nanostructured Fe.* Applied Physics Letters, 2002. **81**(7): p. 1240-1242.
15. Wei, Q., et al., *Nano-structured vanadium: processing and mechanical properties under quasi-static and dynamic compression*, 2004, Elsevier. p. 359-364.
16. Wei, Q., et al., *Nanoengineering opens a new era for tungsten as well.* JOM Journal of the Minerals, Metals and Materials Society, 2006. **58**(9): p. 40-44.
17. Wei, Q., et al., *Microstructure and mechanical properties of super-strong nanocrystalline tungsten processed by high-pressure torsion.* Acta Materialia, 2006. **54**(15): p. 4079-4089.
18. Lide, D.R., *CRC handbook of chemistry and physics*1993: CRC press.
19. Lassner, E. and W.-D. Schubert, *Tungsten : properties, chemistry, technology of the element, alloys, and chemical compounds*1999, New York: Kluwer Academic/Plenum Publishers. xix, 422 p.

20. Howatson, A.M., P.G. Lund, and J.D. Todd, *Engineering tables and data*. 2nd ed1991, London ; New York: Chapman and Hall. vi, 181 p.
21. Davis, J.R. and ASM International. Handbook Committee., *Properties and selection--nonferrous alloys and special-purpose materials*. 10th ed1990, [Materials Park, OH]: ASM International. xv, 1328 p.
22. Birringer, R., *Nanocrystalline materials*, 1989, Elsevier. p. 33-43.
23. Ames, M., et al., *Unraveling the nature of room temperature grain growth in nanocrystalline materials.* Acta Materialia, 2008. **56**(16): p. 4255-4266.
24. Kothari, N.C., *Grain Growth during Sintering of Tungsten*, 1967. p. 2395-2396.
25. Semchyshen, M., et al., *Refractory metals and alloys*1961, New York,: Interscience Publishers. xii, 623 p.
26. Hayden, H.W. and J.H. Brophy, *The Activated Sintering of Tungsten with Group VIII Elements.* Journal of The Electrochemical Society, 1963. **110**(7): p. 805-810.
27. German, R. and Z. Munir, *Enhanced low-temperature sintering of tungsten.* Metallurgical and Materials Transactions A, 1976. **7**(11): p. 1873-1877.
28. Weissmüller, J., *Alloy effects in nanostructures.* Nanostructured Materials, 1993. **3**(1–6): p. 261-272.
29. Kirchheim, R., *Grain coarsening inhibited by solute segregation.* Acta Materialia, 2002. **50**(2): p. 413-419.
30. Kirchheim, R., *Reducing grain boundary, dislocation line and vacancy formation energies by solute segregation. I. Theoretical background.* Acta Materialia, 2007. **55**(15): p. 5129-5138.
31. Kirchheim, R., *Reducing grain boundary, dislocation line and vacancy formation energies by solute segregation: II. Experimental evidence and consequences.* Acta Materialia, 2007. **55**(15): p. 5139-5148.
32. Millett, P.C., R.P. Selvam, and A. Saxena, *Stabilizing nanocrystalline materials with dopants.* Acta Materialia, 2007. **55**(7): p. 2329-2336.
33. Trelewicz, J.R. and C.A. Schuh, *Grain boundary segregation and thermodynamically stable binary nanocrystalline alloys*, 2009, APS. p. 94112.
34. Weertman, J.R., *Retaining the Nano in Nanocrystalline Alloys.* Science, 2012. **337**(6097): p. 921-922.
35. Weissmüller, J., *Some basic notions on nanostructured solids.* Materials Science and Engineering: A, 1994. **179**: p. 102-107.
36. Detor, A.J. and C.A. Schuh, *Grain boundary segregation, chemical ordering and stability of nanocrystalline alloys: Atomistic computer simulations in the Ni–W system.* Acta Materialia, 2007. **55**(12): p. 4221-4232.
37. Millett, P.C., et al., *Atomistic simulation of grain boundary energetics–Effects of dopants.* Acta Materialia, 2005. **53**(13): p. 3671-3678.
38. Trelewicz, J.R. and C.A. Schuh, *Grain boundary segregation and thermodynamically stable binary nanocrystalline alloys.* Physical Review B, 2009. **79**(9): p. 094112.
39. Kirchheim, R., *Comment on "Unexplored topics and potentials of grain boundary engineering" by LS Shvindlerman and G. Gottstein.* Scripta Materialia, 2006. **55**(10): p. 963-964.
40. Gottstein, G. and L. Shvindlerman, *Reply to comments on "Unexplored Topics and Potentials of Grain Boundary Engineering",[Scripta Materialia, 54 (2006) 1041–1045].* Scripta Materialia, 2006. **55**(10): p. 965-966.

41. Purohit, Y., et al., *First-principles-based mesoscale modeling of the solute-induced stabilization of <1 0 0> tilt grain boundaries in an Al–Pb alloy.* Acta Materialia, 2011. **59**(18): p. 7022-7028.
42. Sahni, P.S., et al., *Kinetics of ordering in two dimensions. II. Quenched systems.* Physical Review B, 1983. **28**(5): p. 2705-2716.
43. Grest, G.S., M.P. Anderson, and D.J. Srolovitz, *Domain-growth kinetics for the Q-state Potts model in two and three dimensions.* Physical Review B, 1988. **38**(7): p. 4752-4760.
44. Mazor, A., et al., *Columnar growth in thin films.* Physical Review Letters, 1988. **60**(5): p. 424-427.
45. LeSar, R., R. Najafabadi, and D.J. Srolovitz, *Finite-temperature defect properties from free-energy minimization.* Physical Review Letters, 1989. **63**(6): p. 624-627.
46. Bruschi, P., P. Cagnoni, and A. Nannini, *Temperature-dependent Monte Carlo simulations of thin metal film growth and percolation.* Physical Review B, 1997. **55**(12): p. 7955-7963.
47. Ono, N., K. Kimura, and T. Watanabe, *Monte Carlo simulation of grain growth with the full spectra of grain orientation and grain boundary energy.* Acta Materialia, 1999. **47**(3): p. 1007-1017.
48. Raabe, D., *Scaling Monte Carlo kinetics of the Potts model using rate theory.* Acta Materialia, 2000. **48**(7): p. 1617-1628.
49. Creuze, J., et al., *Wetting and Structural Transition Induced by Segregation at Grain Boundaries: A Monte Carlo Study.* Physical Review Letters, 2001. **86**(25): p. 5735-5738.
50. Holm, E. and C. Battaile, *The computer simulation of microstructural evolution.* JOM, 2001. **53**(9): p. 20-23.
51. Tu, K.N., A.M. Gusak, and I. Sobchenko, *Linear rate of grain growth in thin films during deposition.* Physical Review B, 2003. **67**(24): p. 245408.
52. Lobkovsky, A.E., et al., *Grain shape, grain boundary mobility and the Herring relation.* Acta Materialia, 2004. **52**(2): p. 285-292.
53. Purohit, Y., et al., *Atomistic modeling of the segregation of lead impurities to a grain boundary in an aluminum bicrystalline solid.* Materials Science and Engineering: A, 2008. **493**(1–2): p. 97-100.
54. Gruber, J., et al., *Misorientation texture development during grain growth. Part I: Simulation and experiment.* Acta Materialia, 2009. **57**(20): p. 6102-6112.
55. Leblanc, M.D., et al., *Transition temperature and magnetic properties of the granular Ising model in two dimensions studied by Monte Carlo simulations: Impact of intragrain spin structure.* Physical Review B, 2010. **82**(17): p. 174435.
56. Ko, K.-J., A.D. Rollett, and N.-M. Hwang, *Abnormal grain growth of Goss grains in Fe–3% Si steel driven by sub-boundary-enhanced solid-state wetting: Analysis by Monte Carlo simulation.* Acta Materialia, 2010. **58**(13): p. 4414-4423.
57. Purohit, Y., et al., *Computational study of the impurity induced reduction of grain boundary energies in nano- and bi-crystalline Al–Pb alloys.* Materials Science and Engineering: A, 2010. **527**(7–8): p. 1769-1775.
58. Sadigh, B., et al., *Scalable parallel Monte Carlo algorithm for atomistic simulations of precipitation in alloys.* Physical Review B, 2012. **85**(18): p. 184203.
59. Metropolis, N., et al., *Equation of State Calculations by Fast Computing Machines.* The Journal of Chemical Physics, 1953. **21**(6): p. 1087-1092.

60. Anderson, M.P., et al., *Computer simulation of grain growth—I. Kinetics.* Acta Metallurgica, 1984. **32**(5): p. 783-791.
61. Voter, A., *INTRODUCTION TO THE KINETIC MONTE CARLO METHOD*, in *Radiation Effects in Solids*, K. Sickafus, E. Kotomin, and B. Uberuaga, Editors. 2007, Springer Netherlands. p. 1-23.
62. Murdoch, H.A. and C.A. Schuh, *Stability of binary nanocrystalline alloys against grain growth and phase separation.* Acta Materialia, 2013. **61**(6): p. 2121-2132.
63. Najafabadi, R., et al., *The Effects of Segregation on Grain Boundary Cohesive Energies in Ni 3--xAl 1+ x.* Scripta Metallurgica et Materialia(USA), 1991. **25**(11): p. 2497-2502.
64. Chookajorn, T., H.A. Murdoch, and C.A. Schuh, *Design of Stable Nanocrystalline Alloys.* Science, 2012. **337**(6097): p. 951-954.
65. Jonsson, S., *Reevaluation of the Ti-W system and prediction of the Ti-W-N phase diagram.* Zeitschrift für Metallkunde, 1996. **87**: p. 784.
66. Suryanarayana, C., *Mechanical alloying and milling.* Progress in Materials Science, 2001. **46**(1–2): p. 1-184.
67. Zhang, Z., F. Zhou, and E.J. Lavernia, *On the analysis of grain size in bulk nanocrystalline materials via x-ray diffraction.* Metallurgical and Materials Transactions A, 2003. **34**(6): p. 1349-1355.
68. Lee, J.S., C. Minkwitz, and C. Herzig, *Grain Boundary Self-Diffusion in Polycrystalline Tungsten at Low Temperatures.* physica status solidi (b), 1997. **202**(2): p. 931-940.
69. Köhler, U. and C. Herzig, *On the Anomalous Self-Diffusion in B.C.C. Titanium.* physica status solidi (b), 1987. **144**(1): p. 243-251.
70. Taheri, M.L., et al., *Site-specific atomic scale analysis of solute segregation to a coincidence site lattice grain boundary.* Ultramicroscopy, 2010. **110**(4): p. 278-284.
71. Browning, N.D., et al., *The Application of Scanning Transmission Electron Microscopy (STEM) to the Study of Nanoscale Systems*

Modeling Nanoscale Imaging in Electron Microscopy, T. Vogt, W. Dahmen, and P. Binev, Editors. 2012, Springer US. p. 11-40.
72. Kimoto, K., et al., *Element-selective imaging of atomic columns in a crystal using STEM and EELS.* Nature, 2007. **450**(7170): p. 702-704.
73. Reed, S.J.B., *The single-scattering model and spatial resolution in X-ray analysis of thin foils.* Ultramicroscopy, 1982. **7**(4): p. 405-409.
74. Lartigue-Korinek, S., et al., *HAADF study of the relationship between intergranular defect structure and yttrium segregation in an alumina grain boundary.* Acta Materialia, 2011. **59**(9): p. 3519-3527.
75. Duscher, G., et al., *Bismuth-induced embrittlement of copper grain boundaries.* Nat Mater, 2004. **3**(9): p. 621-626.
76. Buban, J.P., et al., *Grain Boundary Strengthening in Alumina by Rare Earth Impurities.* Science, 2006. **311**(5758): p. 212-215.
77. Luo, J., et al., *The Role of a Bilayer Interfacial Phase on Liquid Metal Embrittlement.* Science, 2011. **333**(6050): p. 1730-1733.
78. Shih, S.-J., S. Lozano-Perez, and D.J.H. Cockayne, *Investigation of grain boundaries for abnormal grain growth in polycrystalline SrTiO3.* Journal of Materials Research, 2010. **25**(02): p. 260-265.

79. Yoshida, H., K. Matsui, and Y. Ikuhara, *Low-Temperature Superplasticity in Nanocrystalline Tetragonal Zirconia Polycrystal (TZP).* Journal of the American Ceramic Society, 2012. **95**(5): p. 1701-1708.
80. Cliff, G. and G.W. Lorimer, *The quantitative analysis of thin specimens.* Journal of Microscopy, 1975. **103**(2): p. 203-207.
81. Watanabe, M. and D.B. Williams, *The quantitative analysis of thin specimens: a review of progress from the Cliff-Lorimer to the new ζ-factor methods.* Journal of Microscopy, 2006. **221**(2): p. 89-109.
82. Watanabe, M., Z. Horita, and M. Nemoto, *Absorption correction and thickness determination using the ζ factor in quantitative X-ray microanalysis.* Ultramicroscopy, 1996. **65**(3–4): p. 187-198.
83. Williams, D.B. and C.B. Carter, *Transmission Electron Microscopy: A Textbook for Materials Science*2009: Springer.
84. Robertson, I.M., et al., *Towards an integrated materials characterization toolbox.* Journal of Materials Research, 2011. **26**(11): p. 1341-1383.
85. Detor, A.J., M.K. Miller, and C.A. Schuh, *Solute distribution in nanocrystalline Ni–W alloys examined through atom probe tomography*, 2006, Taylor & Francis. p. 4459-4475.
86. Detor, A.J., M.K. Miller, and C.A. Schuh, *Measuring grain-boundary segregation in nanocrystalline alloys: direct validation of statistical techniques using atom probe tomography*, 2007, Taylor & Francis. p. 581-587.